Time-domain Analysis of Multiconductor Transmission Lines Excited by Transient Electromagnetic Disturbances Based on the Analog Behavior Modeling

A dissertation submitted to

Xi'an Jiaotong University and Politecnico di Torino

in partial fulfillment of the requirements

for the degree of

Doctor of Philosophy

By

Ziweihua Du

Supervisor: Yan-zhao Xie

Co-superivisor: Flavio Canavero

Electrical Engineering

July 2020

I hereby declare that, the contents and organisation of this dissertation constitute my own original work and does not compromise in any way the rights of third parties, including those relating to the security of personal data.

. . . .

Ziweihua Du

Xi'an, April 29, 2020

摘　要

现代社会越来越重视对各类瞬态电磁干扰（Transient Electromagnetic Disturbances, TEDs）的研究，如雷电电磁脉冲、高空电磁脉冲、开关操作产生的电磁干扰、静电放电等。多导体传输线（Multiconductor Transmission Lines, MTLs）在瞬态电磁场的辐照下，可以感应出幅值较高的电压和电流，可能对传输系统中的 MTLs 和与其相连的终端设备造成严重的影响甚至损坏。因此，当需要同时考虑系统中的频变参数和器件的非线性特性时，建立可计算入射场激励下 MTLs 瞬态响应的时域模型对研究其响应规律和保护技术具有重要意义。本论文的研究目标是基于广义特征法（Method of Characteristics, MoC）和 PSpice 软件的模拟行为建模（Analog Behavior Modeling, ABM）特性提出一个准确而高效的时域宏模型建模方法，在 SPICE 求解器中计算研究 TEDs 激励下端接线性或非线性负载的埋地或架空 MTLs，传输线网络以及以变压器为代表的线圈类设备上的瞬态响应。

本文首先利用 PSpice 仿真软件内 ABM 库中的瞬态和频域器件，建立了 MTLs 的时域宏模型，并重点分析了影响模型准确性和无源性的几个重要参数和约束条件。其次，对传输线宏模型进行拓展，使其可对入射场激励下有损地面上的 MTLs 和传输线网络进行建模。然后，针对入射场对埋地电缆的耦合问题，提出了一种可以评估埋地同轴电缆瞬态响应的宏模型。最后，建立了一种可用于分析变压器绕组内过电压的宽频电路模型，可在 SPICE 内与系统中其他元件的模型联合进行高效的瞬态分析。本论文得到的主要研究成果如下：

利用 ABM 库中的瞬态和频域器件，在进行瞬态分析时对系统内的频率相关变量和非线性特性建模。提出并分析了可保证 ABM 频域器件计算准确性和效率的一些参数选取准则和约束条件。基于以上研究，针对 MTLs 提出了一种精确而高效的宏模型建模方法。该宏模型直接利用 LAPLACE 或 FREQ 器件对传输线的特性阻抗（或导纳）和传播算子进行建模。此外，提出并证明了可保证宏模型无源性的充分条件。数值算例的计算结果表明，该建模方法不仅能保证计算结果的准确性，而且极大地简化和加快了建模和仿真过程，特别是在研究端接非线性负载的长 MTLs 时，该方法的优势更加明显。

将所提出的宏模型拓展使其包括外场激励和有耗大地的影响，研究建立了入射场作用下损耗大地上多导体传输线和传输线网络的宏模型。详细阐述和讨论了传输线方程中单位长度参数的表达形式，特别是大地阻抗和导纳参数。利用宏模型的模块化和独立性，将两个子模型的端口子模型连接在一起，对传输线网络进行建模。此外，在某些特定情况下，提出了基于戴维宁变换的网络简化模型。具体是将网络的离散分支等效为一个单端口的戴维宁电路。利用数值算例进行验证，证明了宏模型的正确性和有效性。然后利用所提出的宏模型对线路参数、大地损耗和架空地线对瞬态响应结果的影响进行了数值规律研究。

研究提出了一种计算外场激励下埋地电缆瞬态响应的时域宏模型。通过与现有的

闭式表达式类比，提出了单位长度大地自阻抗、互阻抗和导纳积分表达式的近似表达式，大大提高了参数提取效率。该方法避免了时域有限差分法（Finite Difference Time Domain, FDTD）中常用的时间和空间离散化和低效复杂的瞬态参数提取过程。利用数值算例进行验证，该宏模型在保证准确性的前提下仿真效率明显提高。另外，与架空传输线网络一样，埋地网络的宏模型也很容易实现。

最后，研究提出了一种电压波侵入变压器后计算绕组内暂态过电压的等效电路模型。具体建立了变压器绕组的端口模型和传递函数电路模型，其可与系统内传输线或其它元件的电路模型联合，方便且高效地在 SPICE 求解器内进行瞬态分析。

SUMMARY

Modern society pays more attention on transient electromagnetic disturbances (TEDs), such as lightning electromagnetic pulse (LEMP), high altitude electromagnetic pulse (HEMP), electromagnetic interference due to switching operations, electro-static discharge (ESD), and so on. The transient electromagnetic field could couple to multiconductor transmission lines (MTLs), and induced over-voltages and over-currents may cause serious effects or even damage to MTLs and the connected terminal equipment in transmission systems. Hence, the time-domain theoretical modeling of MTLs to incident field coupling is of great significance for researchers and engineers to study response laws and protection technologies, when frequency-dependent variables and nonlinear components in systems must be taken into consideration simultaneously. The aim of this research is to propose an accurate and efficient time-domain macro-modeling algorithm using generalized Method of Characteristics (MoC) and Analog Behavior Modeling (ABM) feature in PSpice, in order to study transient responses of buried or overhead MTLs and TL networks terminated with linear or nonlinear devices and large-coil type equipment (represented by transformers) excited by TEDs in SPICE solvers.

First, in this dissertation, using the instantaneous and frequency-domain devices in ABM library, a time-domain macromodel for MTLs is established. Especially, several important parameters and constraints which are related to the accuracy and passivity of the model are analyzed. Second, the macromodel of MTLs is modified to model field coupling to MTLs and TL networks above lossy ground. Then, for the problems of field coupling to buried cables, a macromodel that can estimate transient responses of coaxial cables is presented. Finally, a wide-frequency circuit model for the analysis of over-voltages in the transformer winding is established, to perform transient analysis with models of other system components in SPICE efficiently. The main achievements of this dissertation are listed below:

The instantaneous and frequency-domain ABM devices are utilized to model frequency dependent components and nonlinear characteristics during transient analysis. Some criteria and constraints for accurate modeling and efficient calculation of frequency-domain parts of ABM are also proposed and analyzed. An accurate and efficient time-domain macromodeling algorithm is proposed to calculate transient responses of MTLs, in which the characteristic impedances (or admittances) and propagation operators of TLs are modeled using LAPLACE or FREQ devices directly. Furthermore, a sufficient condition is proposed and proved to guarantee the passivity of the proposed macromodel. According to the numerical validation, the proposed algorithm can not only yield accurate macromodels, but largely simplifies and speeds up the

modeling and simulation processes, especially for long MTLs terminated with linear or non-linear loads.

The proposed macromodel for MTLs is extended to include the field excitation and lossy ground, to model the MTLs and TL networks above lossy ground to field coupling. The expressions of p.u.l parameters, especially for ground impedance and admittance, are discussed. The modularity and independence of the macromodel are utilized to model the TL network, by connecting two-port sub-models together. In addition, for certain scenarios, a simplified model of the network is proposed based on the Thevenin transformation, in which discrete branches is equivalent to a one-port Thevenin circuit. According to the numerical validation, the proposed macromodel is proved to be accurate and efficient. The macromodel is utilized to carry out numerical studies about effects of line parameters, lossy ground and ground wires on induced responses.

A time-domain macromodeling method is proposed to calculate transient responses of buried cables to incident field coupling. Furthermore, approximation expressions for integral formulations of self and mutual ground impedance and admittance are proposed by an analogy with the closed-form expressions. Hence, the proposed algorithm avoids the time and spatial discretization and inefficient transient parameter evaluation generally used in Finite Difference Time Domain (FDTD) method. According to the numerical validation, the simulation efficiency is improved significantly on the premise of accuracy. Also, like overhead TL networks, the macromodel for filed coupling to buried line networks can also be easily realized.

Finally, an equivalent circuit model is proposed to calculate transient over-voltages in the winding when a voltage pulse invades into the transformer. So the input-port model of the winding and the transfer function's circuit model can be established, which can be combined with equivalent circuits of MTLs or devices in the system to perform transient analysis conveniently and efficiently.

SOMMARIO

La società moderna presta crescente attenzione ai disturbi elettromagnetici transitori (TED), come gli impulsi elettromagnetici da fulmine (LEMP), gli impulsi elettromagnetici dovuti ad esplosioni nucleari d'alta quota (HEMP), le interferenze elettromagnetiche dovute a operazioni di commutazione negli impianti elettrici, le scariche elettrostatiche (ESD) e così via. Il campo elettromagnetico transitorio può accoppiarsi alle linee di trasmissione multiconduttore (MTL) e le sovratensioni e sovracorrenti indotte possono causare effetti gravi o persino danni alle MTL e alle apparecchiature terminali nei sistemi di trasmissione. Quindi, la modellizzazione teorica nel dominio del tempo delle MTLs è di grande importanza per lo studio dell'accoppiamento del campo incidente e per le relative tecnologie di protezione, quando le variabili dipendenti dalla frequenza e i componenti non lineari nei sistemi devono essere presi in considerazione contemporaneamente. Lo scopo di questa ricerca è di proporre un accurato ed efficiente algoritmo di macromodellamento nel dominio del tempo, basato sul metodo generalizzato delle caratteristiche (MoC) e sulla modellizzazione comportamentale analogica (ABM), al fine di studiare mediante solutori SPICE le risposte transitorie di reti di distribuzione aeree o interrate, terminate con dispositivi lineari o non lineari e apparecchiature con bobine di grandi dimensioni (rappresentate da trasformatori), in presenza di TED.

Innanzitutto, in questa tesi, utilizzando i dispositivi adinamici e dinamici della libreria ABM di PSpice, viene stabilito un macromodello nel dominio del tempo per MTL. In particolare, vengono analizzati numerosi parametri e vincoli importanti correlati all'accuratezza e alla passività del modello. In secondo luogo, il macromodello di MTL viene modificato per modellare l'accoppiamento del campo elettromagnetico con le reti MTL al di sopra del terreno con perdite. Quindi, per i problemi di accoppiamento del campo a cavi interrati, viene presentato un macromodello in grado di stimare le risposte transitorie di cavi coassiali. Infine, viene stabilito un modello di circuito a larga banda per l'analisi delle sovratensioni nell'avvolgimento di un trasformatore, per eseguire in modo efficiente la co-simulazione in SPICE con i modelli di altri componenti del sistema. I principali risultati di questa tesi sono elencati di seguito:

I dispositivi adinamici e dinamici della libreria ABM di PSpice sono utilizzati per modellare componenti dipendenti dalla frequenza e caratteristiche non lineari durante l'analisi transitoria. Vengono inoltre proposti e analizzati alcuni criteri e vincoli per una modellizzazione accurata e un calcolo efficiente delle parti ABM dipendenti dalla frequenza. Viene proposto un algoritmo accurato ed efficiente per la macromodellizzazione nel dominio del tempo e per calcolare le risposte transitorie di MTL, in cui le impedenze caratteristiche (o le ammettenze) e gli operatori

di propagazione delle linee sono modellati direttamente utilizzando le istruzioni LAPLACE o FREQ. Inoltre, viene proposta e dimostrata una condizione sufficiente a garantire la passività del macromodello proposto. Secondo la convalida numerica, l'algoritmo proposto non solo può produrre macromodelli accurati, ma semplifica e accelera ampiamente i processi di modellazione e simulazione, in particolare per MTL molto lunghe e terminate con carichi lineari o non lineari.

Il macromodello proposto per le MTL viene esteso per includere l'eccitazione del campo esterno e del terreno con perdite, per modellare la risposta di reti MTL al di sopra del terreno al campo esterno. Vengono discusse le espressioni dei parametri per unità di lunghezza, specialmente per l'impedenza e l'ammettenza del suolo. La modularità e l'indipendenza del macromodello sono utilizzate per modellare la rete di linee, collegando insieme sottomodelli a due porte. Inoltre, per alcuni scenari, abbiamo proposto un modello semplificato della rete basato sulla trasformazione di Thevenin, in cui rami discreti della rete equivalgono a un circuito di Thevenin a una porta. Secondo la validazione numerica, il macromodello proposto si è dimostrato accurato ed efficiente. Il macromodello viene utilizzato per eseguire studi numerici degli effetti dei parametri di linea, del suolo con perdite e dei conduttori di terra sulle risposte indotte.

Viene proposto un metodo di macromodellizzazione nel dominio del tempo per calcolare le risposte transitorie dei cavi interrati all'accoppiamento con il campo incidente. Inoltre, le espressioni di approssimazione per le formulazioni integrali di auto e mutua impedenza (e ammettenza) del suolo sono proposte da un'analogia con le espressioni esistenti in forma chiusa. Pertanto, l'algoritmo proposto evita la discretizzazione spaziale e temporale e la valutazione inefficiente dei parametri transitori generalmente utilizzati dal metodo delle Differenze Finite nel Dominio del Tempo (FDTD). La validazione numerica dimostra che l'efficienza della simulazione è migliorata in modo significativo in base alla precisione. Inoltre, come per le reti TL aeree, è anche possibile realizzare facilmente il macromodello per l'accoppiamento del campo alle reti di linee interrate.

Infine, viene proposto un modello circuitale equivalente per calcolare sovratensioni transitorie nell'avvolgimento quando un impulso di tensione colpisce un trasformatore. In questo modo è possibile stabilire il modello d'ingresso dell'avvolgimento e il modello circuitale della funzione di trasferimento, che può essere combinato con circuiti equivalenti di MTL o dispositivi nel sistema per eseguire analisi transitorie in modo conveniente ed efficiente.

CONTENTS

List of Figures

List of Tables

1   Introduction

1.1 Research background and significance

Modern society pays more attention on transient electromagnetic disturbances (TEDs), such as lightning electromagnetic pulse (LEMP), geomagnetic disturbance (GMD) caused by sunspots, high altitude electromagnetic pulse (HEMP), electromagnetic interference due to switching operations in gas-insulated substation (GIS) and ESD electromagnetic pulse (ESD-EMP), as well as some artificial electromagnetic radiation sources, such as ultra-wide band (UWB) pulse and narrow-band high power microwave (HPM), spring up continuously, which may be utilized by terrorists or criminals and brought into systems as the intentional electromagnetic interference (IEMI)[1–8].

All of above TEDs could couple to transmission line (TL) systems[9–11], such as high-voltage overhead TLs, natural gases/oil pipelines, cables, bundles, PCB tracks, interconnects, etc., and then induce transient over-voltages and over-currents on them. The induced voltage and current responses due to incident field coupling may degrade the performance, or even result in serious permanent damage effects to lines and connected equipment. Especially recently, modern electronic systems develop toward miniaturization, high integration and low power consumption, as well as the power system and other wide-area distributed systems develop toward intelligence and large-scale interconnection continuously, a large number of sensitive electronic components and equipment are introduced into systems. Hence, the modern electrical/electronic systems are more vulnerable to above-mentioned TEDs, leading to impact and destruction to them, or even threat to the social security[12–17].

In fact, typical electrical/electronic transmission systems, such as power transmission systems and communication systems that are inevitably exposed to transient electromagnetic fields, may suffer severe impact or damage due to induced interference, or even normal operation of systems is threatened[18–22]. Taking the power system as an example, there are many wide-distributed overhead lines in the system. The over-voltages and over-currents due to incident fields on TLs may cause flashover of insulators and short-circuit faults. Consequently, the TLs may trip and the power supply is interrupted[23–25]. Meanwhile, through the interconnection between TLs and electrical/electronic equipment, the energy of incident transient field can further couple into them. Such as the power transformer, a kind of typical coil-type primary equipment, the induced voltage pulse on TLs may invade into transformer windings. Because of the high amplitude and fast wavefront of the voltage pulse, it will result in extremely uneven turn-to-turn voltage distribution, and a serious threat to the insulation of windings[26–28]. Besides, the secondary devices of the power system, such as supervisory control and data acquisition (SCADA) systems and sensors, etc., may be interfered and damaged, rendering

measurement error, mal-operation or refused operation of protection relay, and other serious consequences[22, 29]. These consequences seriously affect the power system's safety and reliability, or even cause enormous economic loss and casualties. Furthermore, as transmission technoloies develop and population densities increase, underground transmission systems have been widely leveraged, especially in metropolitan areas and common corridors[30, 31]. Therefore, the incident transient fields can also couple to buried lines, and may affect the operation of underground transmission systems[32–37]. In conclusion, for the design, construction and protective strengthening of systems in circumstances of transient electromagnetic fields, it is of great significance for the research on coupling effects of incident fields to power, or electronic systems and other wide-area distributed tranmission systems.

Based on above analysis, the essence of this study is the coupling effect and response laws of transient fields on MTLs and terminal equipment in transmission systems. Compared with the experimental research, the theoretical modeling can not only reduce the cost of research, but better reveal the essential mechanism and influence rules of the incident field coupling, which is convenient for quantitative prediction of TL responses[38–42].

The wide-area distributed transmission systems are characterized by large scale, long lines and complex interconnect structure, etc., which cause more complicated response laws, more serious and unpredictable influence of incident fields on systems. Besides, the nonlinear components in systems can only be described in time domain as nonlinear ordinary differential equations (ODEs), such as metal oxide varistors (MOVs) installed in power transmission systems and transient voltage suppressors (TVS) widely used for surge protection. However, the frequency-dependent parameters of the surrounding media and distributed lines are both best described and solved in the frequency domain. Hence, there are two major difficulties for analyzing field coupling to wide-area distributed transmission systems in a single simulation environment. The first one is linking distributed TLs with nonlinear elements, which results in a mixed frequency-domain and time-domain problem. It is essential to model MTLs in time domain so that they can be directly solved in a nonlinear simulation software. The second one is due to time-consuming simulation when analyzing large-scale MTLs. Because of above difficulties, an efficient and accurate time-domain method for straightforward evaluation of TEDs effects on MTLs and terminal equipment is desirable.

In conclusion, the research target of this dissertation is to propose a time-domain algorithm to study transient responses of wide-area long-distance MTLs, TL networks terminated with equipment (mainly including nonlinear protective devices and large-coil type equipment represented by transformers) exposed to the incident transient fields. And specifically, the proposed algorithm can perform transient analysis both for buried and overhead lines, so as to consider frequency-dependent variables and nonlinear elements at the same time. The efficiency is not limited by the line length and loss, which is of great practical significance and application

value for the research of real overhead and buried transmission systems to the transient field coupling.

1.2 State of the art

1.2.1 Existing time-domain methods for field-to-line coupling issues

In most cases, the classical TL theory has been proved to be a valid approximation for the computation of coupling and propagation along TLs, especially for uniform TLs, in which the excitation source and TLs are both modeled by distributed parameters. Different from the antenna theory or full-wave methodologies, the propagation along the line is assumed to be quasi transverse electromagnetic (TEM), that is, only the TL mode component is considered, but higher-order modes, such as the antenna mode, are ignored[19, 40, 43]. Since for general analysis of TEDs effects on TLs, more attention is often paid to the current or voltage responses at terminals. As antenna mode behaves as the common mode, it cancels each other out at terminals, which can be reasonably omitted in the response analysis at terminals of TLs, and only the TL mode component left to be considered to meet the need of theoretical analysis[44, 45]. Compared with the antenna theory, the TL theory greatly simplifies the calculation process and improves the calculation efficiency on the premise of accuracy, therefore, it has been widely applied in the research of response analysis of TLs. Under quasi-TEM distributed assumptions, the voltages and currents are related by Telegrapher's equations, which are essentially a kind of partial differential equations (PDEs) firstly proposed by Oliver Heaviside. In order to contain external incident fields, three equivalent approaches have been proposed, including Taylor, Agrawal and Rachidi model[46–48].

There have been a significant amount of research for the simulation of transient field responses of distributed MTLs with nonlinear components, involving two main time-domain strategies. One strategy is based on numerical or analytical calculation techniques[33, 34, 49–62], and the other is based on developing efficient macromodels for TLs[63–71].

Some researchers have adopted finite difference time domain (FDTD) method to establish calculation models for MTLs[33, 34, 53–58]. It practically discretizes the Telegrapher's equations in terms of time and space steps by a first-order point-centered integration scheme. The FDTD has advantages of simplicity, intuitionistic and generality, which has been widely used in the processing of MTLs issues in time domain. However, in practical applications, FDTD method sometimes encounters numerical dispersion problem and the limitation of stability condition. Because general frequency-domain expressions of per-unit-length (p.u.l) parameters don't have analytical inverse Fourier transforms, another challenge when implementing FDTD is to determine p.u.l parameters in time domain. Generally, numerical inverse Fourier transform (IFT) algorithms or numerical curve fitting methods combined with analytical IFT can be adopted

to obtain time-domain approximations of transient parameters, which lead to the cumbersome evaluation of transient parameters. The potential loss of accuracy may also be generated in the process of numerical IFT and curve fitting in terms of errors. Besides, the distributed MTLs systems are generally large, covering a length of hundreds or even thousands of meters. Consequently, the simulation requires long computing time and large memory resources, especially for fast transient fields coupling to long MTLs.

Besides above, under the assumption of weak coupling, a time-domain efficient method is proposed by Paul to solve TL equations for three-conductor lossless lines in the symbolic form[72]. Many scholars proposed algorithms[73–76] based on waveform relaxation and transverse partitioning (WR-TP) numerical techniques, so that the large-scale circuit is split into smaller subcircuits that can be solved iteratively in sequence or in parallel. Hence, the simulation cost is largely reduced and a high calculation efficiency is obtained.

XIE, Canavero, Guo, etc. proposed the frequency-domain distributed analytical representation and iterative technique (DARIT) to problems of crosstalk and field coupling[77–79]. This technique is also extended by them to the time domain for field coupling to MTLs [80, 81]. This method (DARIT in time domain) is with good accuracy and can deal with nonlinear problems effectively. However, in order to model nonlinear loads, piecewise linear is required to fit V-I characteristics, and the whole working interval is equivalent to multiple linear working intervals. Therefore, during the calculation process, it is necessary to preset a value of the load firstly, then judge whether the current and voltage response is the correct value at the corresponding interval through multiple calculations and tests. The analytical derivation process of this method is complicated and very hard to have more than 4 iterations. Furthermore, the fitting precision of the working interval of the nonlinear load directly affects the accuracy of the final responses.

As mentioned before, we usually care about terminal responses. Therefore, based on the TL theory, the classical frequency-domain BLT (Baum, Liu, Tesche) equation is derived[43], which can analytically present expressions of current and voltage responses at terminals with the influence of incident fields. In order to analyze nonlinear systems, based on the classical frequency-domain BLT equation, Baum C.E. gave a time-domain BLT equation in 1999[59]. In 2007, Tesche presented the time-domain BLT equation of a single-conductor TL and adopted it to calculate responses on nonlinear terminal loads[60, 61]. The time-domain BLT equation requires an enormous amount of computation, and it is inconvenient to complete: on the one hand, time-domain BLT equation involves a lot of convolution; on the other hand, when the terminal load is nonlinear, a nonlinear matrix equation needs to be solved firstly to determine the time-domain reflection coefficient. Therefore, after Tesche's papers, there are no more literatures on the time-domain BLT equation.

In addition to above techniques, macrmodeling of MTLs has been a topic of intense re-

search[82–87]. The macromodel essentially represent a line as a two-port model for its input and output ports. An important part of the process in generating a macromodel is to convert Telegrapher's equations into ODEs that most CAD computer programs, such as SPICE, can solve. It's worth noting that the solutions of lossy TL equations involve transcendental functions which have an infinite number of roots. Any transfer function will therefore have an unlimited number of poles that characterize time-domain responses. So determining the inverse Laplace transforms of transfer functions in order to return to the time domain is a tough task.

In theory, chain parameter matrix, admittance matrix, impedance matrix or scattering parameter matrix can be used to describe terminal characteristics of MTLs[43]. The resulting macromodels are suitable to study physical characteristics of TLs and physical laws of field-to-line coupling theoretically. In reality, the lumped-parameter circuit can be equivalent to TLs, so that both of them have same terminal characteristics, and obtained macromodels are suitable to carry out efficient transient simulation in the circuit solver directly. The macromodel is the lumped equivalence of the distribution characteristics of TLs, and it has obvious advantages in the analysis of MTLs and huge TL networks with complex loads when integrated in SPCIE-like circuit solvers:

1. When the terminal is a lumped load, but the characteristic is complex (such as the non-linear load), it requires the establishment of TL's equivalent circuit model to perform efficient transient analysis, which is just what the advantage of the macromodel. Furthermore, there are a large number of nonlinear devices in libraries of SPICE, which can be adopted directly to model nonlinear loads;

2. The macromodel converts field-to-line coupling issues into circuit problems. It is convenient to combine with models of devices to calculate responses on terminal equipment irradiated by incident TEDs simultaneously.

3. The macromodel is featured with modularity and independence. So when the research object is a TL network with a huge number of TLs in it, the macromodel can decompose the complex network into several parts and greatly simplify the modeling and calculation processes;

4. The SPICE solver, such as PSpice, is provided with an analog behavioral modelling (ABM) library. It has the ability to model the behavior of a component using an electrical circuit with controlled current or voltage source from an external viewpoint. Hence, the behavior modeling can be adopted to create black-box models to solve mathematical problems in macromodels or to realize nonlinear loads;

5. When the terminal load or the field excitation of TLs has uncertain parameters, the Monte Carlo method is a common choice to study statistical characteristics of response results. Once the macromodel is obtained, as it is determined by TL's characteristics,

it can be reused to perform efficient repeated calculations for random changes;

According to all above analysis, macromodels of MTLs have simple structures which can easily be realized by equivalent circuits and solved. So in this dissertation, the macromodel methodology is adopted as an appropriate and valid tool to study transient responses of MTLs with terminal linear or nonlinear equipment excited by incident fields.

1.2.2 Existing Macromodeling algorithms for TLs

Several macromodel algorithms have been developed to incorporate distributed TLs with nonlinear devices.

Algorithms based on the generalized MoC are most commonly adopted, and the main idea is to represent the terminal behavior of TLs with a set of admittances (impedances) and delayed sources[63–65]. The propagation delay is extracted in MoC macromodels to preserve the efficiency, in which the attenuation function is approximated with a low-order rational function. For long low-loss lines, these MoC macromodels can ensure the TL causality and provide fast calulations. However, there are two major difficulties in the process of algorithm implementation. Firstly, the numerical curve fitting[88] is required to realize the rational approximation of the transfer function. It presents many difficulties as losses become larger, the length becomes longer, and the number of TLs increases. Secondly, the passivity of MoC-based algorithms is difficult to preserve during the process of modeling. Because the potential passivity loss[63, 89] may be generated in tabulated parameters obtained from empirical formulae or measurements, and fitting errors. Since TLs are passive elements, the passivity property must be satisfied. Because the stable but non-passive macromodel can lead to spurious oscillations when it is connected to nonlinear elements.

In order to construct efficient passive macromodels, algorithms based on rational approximations or sectioning methods (such as matrix rational approximations (MRA)[66, 67], integral congruent transformation[90]) that can guarantee the macromodel passivity, have also been developed. However, these algorithms approximate the TL without delay extraction. Consequently, in the presence of long lines with significant delay, these algorithms require high order approximation to accurately capture the delay portion, which leads to many segments in the model and inefficient transient simulation.

In [68], a delay extraction-based passive compact macromodeling algorithm (DEPACT) adopting modified Lie product has been proposed to efficiently model long TLs. It combines the advantages of both MoC and MRA, and performs delay extraction prior to the MRA. Compared to the MRA technique, delay effects are modeled by lossless TLs (i.e. pure delay elements) instead of lumped circuits characterized by rational approximations. For long lossy-coupled TLs, the resulting DEPACT macromodel has lower order, which is composed of a cascade of subnetworks as shown in Figure 1.1. Each subnetwork are referred as a DEPACT

cell, which can be further represented by a cascade of lossless TLs modeled by MoC and lossy sections modeled by MRA, as shown in Figure 1.2. Nonetheless, it is still a sectioning method, so the efficiency of this macromodel will highly depend on the length and losses of TLs, and the frequency band of interest. And generally, the complexity of the DEPACT model will inevitably increase due to MRA-based models.
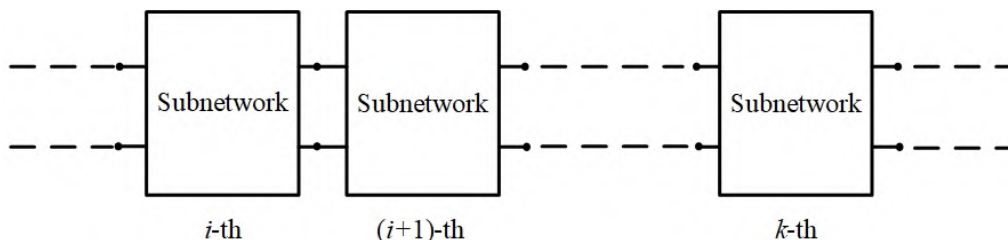
Figure 1.1 A DEPACT macromodel formed by a cascade of DEPACT cells
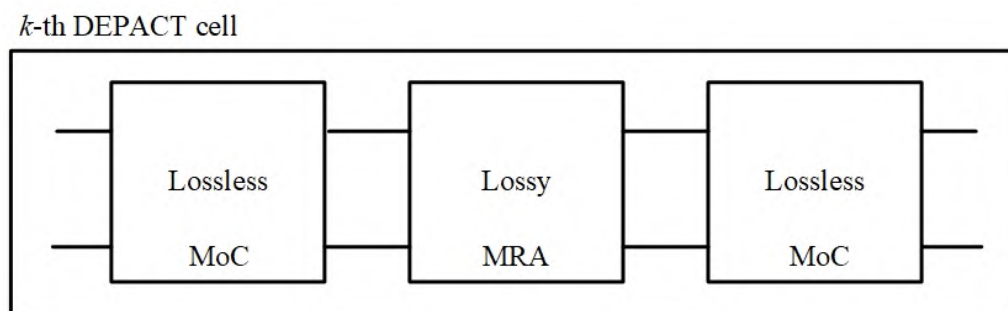
Figure 1.2 Structure of the k-th DEPACT cell

The key issue of this study is to model distributed MTLs exposed to incident fields. For field-to-line coupling issues, above three kinds of macromodeling algorithms have been extended, in which the external field is equivalent to distributed excitation sources along TLs. The macromodel of TLs with no excitation source can be derived from homogeneous Telegrapher's equations, while distributed excitation sources can be considered in non-homogeneous Telegrapher's equations.

In 1994, based on the MoC, Paul proposed a SPICE equivalent circuit model for lossless MTLs under the incident field's excitation[70]. This model is consist of delay lines, control sources and lumped elements. The calculation efficiency is almost independent of the TL length. However, the lossy frequency-dependent parameters are not included in this model. In 1996, Maio et al. established a SPICE equivalent circuit model by transient matched scattering responses and the time-domain fitting method[71]. The model is also based on the MoC, and the effects of excitation field on TLs are considered.

Erdin et al. then proposed a macromodel of lossy TLs under external field excitation in 2001[66, 91]. It is based on the MRA, and the passivity of the model is guaranteed. However, as mentioned above, for TLs with long electrical length and large delay component, MRA needs

high-order approximation to ensure accurate approximation to the exponential matrix, resulting in an increase in the number of model segments and low simulation efficiency.

In 2012, Xin Liu et al. applied the DEPACT macromodel to calculate over-voltages on three-phase power overhead lines loaded with metal oxide arresters excited by LEMP[69]. Concretely, the incident field is assumed to only couple with lossless TL segments, the distributed voltage sources due to horizontal component of the excitation field are equivalent to the lumped sources at terminals of the macromodel. Though the passivity of this macromodel has been proved, in order to accurately approximate the exponential matrix, the order of the Lie product formula (the number of segments) still largely depends on the line length and losses, and the frequency band of the excitation field.

Most existing macromodels are for high-speed interconnect circuits on chip or printed circuit boards and overhead MTLs, etc. With the widespread use of underground systems either for the purpose of power transmission or telecommunication, it is also of great significance to study accurate modeling of underground transmission systems and calculate transient responses when they are excited by transient fields. However, to the best of the authors' knowledge, no macromodel for the field coupling to buried cables that can be embedded in circuit solvers has been developed yet. In contrast with overhead TLs, the contribution of p.u.l ground admittance to the disturbances propagating along buried wires is non-negligible. So the first challenge when implementing the macromodel is to properly represent correction terms of the lossy ground on both p.u.l impedance and admittance terms in the telegrapher's equation. Another one is the approximation of frequency-dependent propagation characteristics, especially when ground admittance must be taken into account.

Hence, based on above analysis, the research in this dissertation mainly focuses on an effective macromodeling algorithm to construct passive time-domain macromodels for incident field coupling to buried/overhead MTLs and TL networks. Using this proposed macromodel, the transient responses of wide-area long-distance MTLs with terminal equipment exposed to incident transient fields can be studied accurately and efficiently, considering both nonlinear components and frequency-dependent characteristics.

1.2.3 Existing time-domain methods for studying over-voltage distribution of transformer windings

When the energy coupling from incident fields flows along TLs and enters into transformer windings as a voltage pulse, the complex electromagnetic coupling phenomenon will occur in the winding, and between the winding and ground. So extreme high over-voltages will be induced, resulting in the inner insulation breakdown of transformer windings[92–95].

For the problems of calculating transient over-voltages in the transformer winding, due to

the emergence of computers and the continuous optimization of program algorithms, numerical calculation and computer simulation technology become more acceptable and have been widely used by engineers and researchers, in addition to traditional measurement methods. The key of the calculation and simulation is to propose an appropriate calculation model for transformer windings and select appropriate parameters. The appropriate model should be choosen in accordance with actual circumstances, which can not only ensure accuracy, but also speed up the simulation efficiency.

According to the general structural parameters of transformer windings, the voltage pulse, whose frequency range is lower than MHz, is regarded as a low-frequency pulse, so the transformer can be equivalent to a lumped-parameter circuit model composed of capacitances and inductances. In other words, the complete or partial winding of the transformer can be equivalent to a certain equivalent circuit, which can be calculated by programming or using SPICE software or other electromagnetic transient analysis software. However, for the transient excitation sources with steep rise time (ns to μs) and wide frequency range (up to hundreds of MHz or even higher), the wavelength of the voltage pulse is comparable to or even less than the transformer winding size, the conventional lumped circuit model will be no longer applicable[96]. Hence, seeking for a new wide-frequency model of windings is necessary to remedy this problem. The model of MTLs, in which each turn in the winding is treated as a TL with the same length, has been widely used for wide-frequency modeling of large transformer windings[97–99].

In 1994, Zanji Wang et al. adopted the frequency domain method to solve MTL equations based on the improved Fourier transform, in which parameters such as capacitance and inductance are frequency-dependent[97]. To overcome the aliasing caused by FFT and IFFT, and consider nonlinear elements or phenomenon, there have been several time-domain numerical algorithms proposed to obtain the voltage distribution of windings. The TL equations can be solved by difference methods, such as FDTD method, Lax difference method and compact finite difference, in which TLs need to be discretized in terms of time and space [40, 87, 100, 101]. The voltage distribution of any part of the winding can be calculated as accurately as possible by using difference methods based on the model of MTLs. However, for large transformer windings, these difference methods may be not efficient enough due to a huge number of turns and corresponding grids.

Zanji Wang then proposed a hybrid method, in which the distributed-parameter model is combined with the lumped-parameter model[102]. Therefore, the first several discs of the winding are represented by the MTLs model in the unit of a turn, while the last several discs are modeled by the lumped parameter model in the unit of discs, and there is mutual coupling between these two models. Although the amount of computation is reduced, some parameters are not easy to determine, and the coupling between models still need to be represented more accurately.

In [103], the vector fitting and recursive convolution are adopted to obtain voltage responses on turns and voltage differences between turns. The vector fitting is used to fit voltage's transfer functions as rational approximations, then the output is calculated simply by convolving the input excitation with the system's unit impulse response in the time domain. To avoid the time-domain convolution, a circuit model of the transfer function is proposed[104]. Firstly, the scattering parameters are used to calculate the voltage's transfer function of each turn, and rational approximation of it can easily be obtained by vector fitting; then, reduced-order model is obtained by the order reduction method; finally, the transfer function's circuit model is realized by the network synthesis technique. Once the circuit model is obtained, it can be conveniently realized and solved in the circuit software, such as PSpice. However, the modeling process is complicated, and the potential accuracy loss cannot be avoided in the process of curve fitting and order reduction.

Hence, based on above analysis, an accurate and efficient modeling method of transformer windings is preferable in our research work, using which the obtained equivalent circuit model can be adopted to carry out transient analysis in SPICE-like circuit solvers. Furthermore, it can also be connected with models of TLs or other nonlinear elements to perform the co-simulation of multiple components in systems.

1.3 Major research content and organization of the dissertation
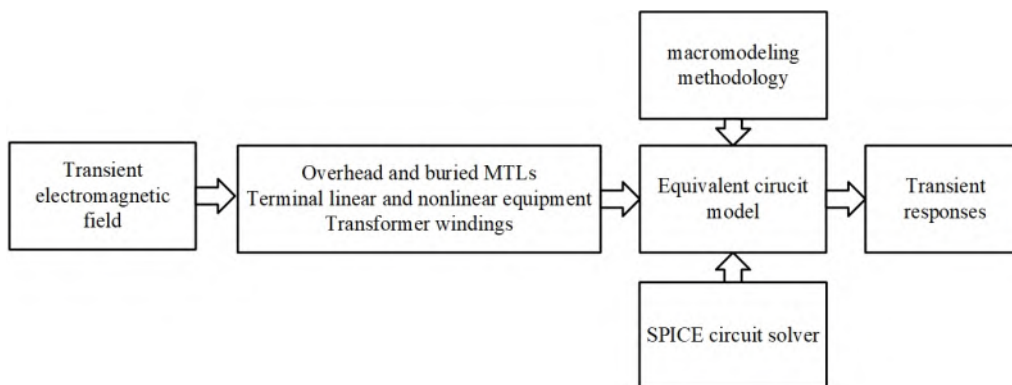
Figure 1.3 Main research content of the dissertation

As shown in the Figure 1.3, the major research content of this dissertation is to study transient responses of wide-area long-distance (overhead and buried) MTLs and TL networks connected with linear/nonlinear terminal devices and the transformer winding excited by transient electromagnetic fields in time domain. So an accurate and effective macromodeling algorithm is proposed based on the generalized MoC and ABM feature to consider frequency-dependent variables and nonlinear elements at the same time. Using this algorithm, overhead and buried lines terminated with transformer windings and orther devices excited by incident fields can be conveniently equivalent to circuit models while insuring the causality and passivity, and

responses of them can be obtained by carrying out efficient transient analysis in SPICE. The main research work includes: a time-domain macromodel for MTLs is established, in which the frequency-dependent variables and non-linear characteristics are modeled by devices of ABM; to include the effects of external fields and lossy ground, the macromodel is extended to model MTLs and TL networks above lossy ground exposed to external fields; for the problems of field coupling to buried cables, we present a macromodel that can estimate transient responses on multiple conducting layers of coaxial cables; finally, taking the power transformer, a typical coil-type equipment as the research object, a circuit model is established to analyze over-voltages in the transformer winding. The specific research work and the structure of the dissertation are arranged as follows:

In Chapter 2, an accurate and efficient time-domain MoC-based macromodel for MTLs is presented. In this algorithm, frequency-dependent characteristics (mainly refer to characteristic impedance and propagation operators) are modeled by frequency-domain devices of ABM, and the instantaneous models are also utilized to model nonlinear components in systems. Then, some key tips and constraints for the use of frequency-domain ABM devices are proposed and analyzed for robust and accurate modeling. Finally, a sufficient condition that guarantee the passivity of the proposed macromodel is provided and proved.

In Chapter 3, for the problems of overhead long-distance MTLs to incident field coupling, the application of the macromodel for MTLs is firstly extended to incorporate the effects of incident fields and lossy ground. Besides, the macromodel of field coupling to TL networks can easily be realized by connecting two-port sub-models together. Furthermore, a simplified model of the network based on the Thevenin transformation is proposed to treat discrete branches of the network as a one-port Thevenin circuit. Various examples will be presented to verify the proposed modeling algorithm.

In Chapter 4, a macromodel for buried cables to field coupling is established, which can estimate transient responses on multiple conducting layers of coaxial cables efficiently. The previous modeling methodology is modified to consider practical cable arrangements and the effects of both ground impedance and admittance. Besides, the approximation expressions for a general semi-infinite integral analytic formulation of the self and mutual ground impedances and admittances are also proposed, to avoid using time-consuming numerical integration techniques. Various examples will be presented to verify the proposed algorithm.

In Chapter 5, an equivalent circuit model is established to calculate transient responses in the transformer winding by SPICE efficiently. The macromodel of MTLs proposed in the previous chapter is firstly adopted to model the transformer winding by considering the boundary condition. Then, the input impedance formula of the winding and the transfer functions of voltages at terminals of turns are derived by solving Telegrapher's equation. Finally, the input-port model of the transformer winding and transfer function's circuit model are realized using

frequency-domain devices of ABM.

The last chapter presents a summary and a list of the future work.

2 An ABM-based time-domain macromodel for MTLs considering frequency-dependent characteristics and non-linear components

The classical TL theory and its macromodels have the merits of simple form and high computation efficiency, which are widely used in the research of transient responses of MTLs. For the macromodel of generalized MoC, the Telegrapher's equations are decoupled to extract the delay firstly, then the characteristic impedance (admittance) and delayless propagation operator are approximated in frequency domain to obtain the macromodel. There is no need to segment the TL, it shows superiority in efficiency compared with other macromodeling methods, though the approximation of propagation operator is still be a tough task and the passivity of the model cannot be guaranteed. The sectioning methods, including MRA and DEPACT macromodels, need the rational approximation to accurately capture transmission delay characteristics. Though the passivity is guaranteed for these models, the efficiency of them is restricted by the length and losses of TLs.

So in order to model wide-area long-distance MTLs and TL networks for efficient transient analysis, in this chapter, an effective MoC-based algorithm is presented to construct a passive time-domain macromodel for MTLs. In this algorithm, frequency-dependent characteristics of TLs are modeled by frequency-domain devices in ABM library. Besides, the instantaneous devices are also utilized to model nonlinear components in systems. Then, for robust and accurate modeling, some key tips and constraints for the use of frequency-domain devices are proposed and analyzed. A sufficient condition to guarantee the passivity of the macromodel is provided and proved. This chapter lays a theoretical foundation for the applied research of the following chapters.

This specific content is arranged as follows: in section 2.1, a brief review of the MoC approach is given. Section 2.2 provides modeling approaches for time-domain convolution and nonlinear elements using devices of ABM feature in SPICE. Then, aimed at frequency-domain parts, some key tips and constraints are proposed and analyzed in section 2.3: 1. how to process the non-causal impulse responses; 2. criteria for defining frequency response tables; 3. the constraints in simulation of Laplace transforms; 4. the trade-off between accuracy and efficiency. On above basis, in section 2.4, we propose time-domain macromodels with and without delay extraction, and provide a numerical example to verify the validity and efficiency of them. In section 2.5, we highlight the importance of passivity, and put forward a sufficient condition to preserve the passivity of the proposed macromodel. Section 2.6 summaries the research work of this chapter.

2.1 The macromodel for MTLs based on the generalized MoC approach

We present in this section the generalized MoC approach for generating the macromodel of MTLs.We firstly review here some details and critical aspects on MoC. Consider lossy distributed MTLs including n conductors and one reference conductor as shown in Figure 2.1, which are governed by Laplace-domain Telegrapher's equations[40] as

$$\frac{\partial}{\partial x}\mathbf{V}(x,s) + (\mathbf{R}(s) + s\mathbf{L}(s))\mathbf{I}(x,s) = \mathbf{0} \tag{2-1a}$$

$$\frac{\partial}{\partial x}\mathbf{I}(x,s) + (\mathbf{G}(s) + s\mathbf{C}(s))\mathbf{V}(x,s) = \mathbf{0} \tag{2-1b}$$

where s is the Laplace-domain variable, $\mathbf{V}(x,s)$ and $\mathbf{I}(x,s)$ are voltage and current vectors at location x on TLs. Frequency-dependent parameters $\mathbf{R}(s)$, $\mathbf{L}(s)$, $\mathbf{G}(s)$, and $\mathbf{C}(s)$ represent p.u.l resistance, inductance, conductance, and capacitance matrices, respectively. Equation (2-1) cannot be directly written as time-domain ordinary differential equations, which means that it is difficult to interface with nonlinear SPICE circuit solvers.
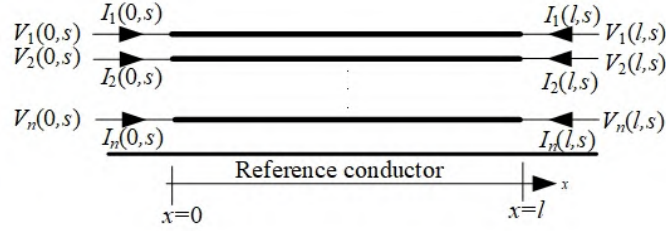
Figure 2.1 $(n+1)$-conductor TLs

In generalized MoC, the solution to (2-1) can be given as[63]

$$\mathbf{V}(0,s) - \mathbf{Z_C}(s)\mathbf{I}(0,s) = \mathbf{H}(s)[\mathbf{V}(l,s) - \mathbf{Z_C}(s)\mathbf{I}(l,s)] \tag{2-2a}$$

$$\mathbf{V}(l,s) + \mathbf{Z_C}(s)\mathbf{I}(l,s) = \mathbf{H}(s)[\mathbf{V}(0,s) + \mathbf{Z_C}(s)\mathbf{I}(0,s)] \tag{2-2b}$$

where $\begin{bmatrix} \mathbf{V}(0,s) \\ \mathbf{V}(l,s) \end{bmatrix}$ and $\begin{bmatrix} \mathbf{I}(0,s) \\ \mathbf{I}(l,s) \end{bmatrix}$ are voltages and currents at terminals of TLs, and l is the length. $\mathbf{H}(s)$ is the propagation operator, which is defined as

$$\mathbf{H}(s) = e^{-\mathbf{\Gamma}(s)l} \tag{2-3}$$

with

$$\mathbf{\Gamma}(s) = \sqrt{(\mathbf{R}(s) + s\mathbf{L}(s))(\mathbf{G}(s) + s\mathbf{C}(s))} \tag{2-4}$$

$$\mathbf{Z_C}(s) = \mathbf{\Gamma}^{-1}(s)(\mathbf{R}(s) + s\mathbf{L}(s)) \tag{2-5}$$

being the propagation function and the characteristic impedance matrix, respectively. The corresponding equivalent circuit of (2-2) representing the voltage wave solution is shown in Figure

2.2.

$$\mathbf{E}_0(s)=\mathbf{H}(s)[\mathbf{V}(l,s)-\mathbf{Z_c}(s)\mathbf{I}(l,s)] \qquad \mathbf{E}_l(s)=\mathbf{H}(s)[\mathbf{V}(0,s)+\mathbf{Z_c}(s)\mathbf{I}(0,s)]$$
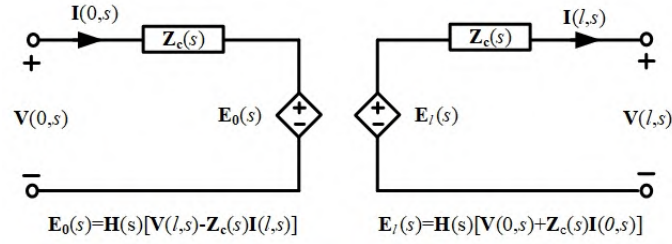
Figure 2.2　Basic equivalent circuit for the MoC model

For lossy TLs, both characteristic impedance and propagation operator are irrational functions of s. Hence, unless rational approximations for both $\mathbf{Z_C}(s)$ and $\mathbf{H}(s)$ are performed, the expressions in (2-2) cannot be directly converted into time-domain ordinary differential equations. However, it is not practical to complete the direct rational approximation of $\mathbf{H}(s)$ over a wide frequency band, since $\mathbf{H}(s)$ includes the delay term which requires a high-order rational approximation to accurately model long TLs with significant delay.

To solve this issue, the eigen-decomposition and delay extraction are adopted to approximate $\mathbf{H}(s)$ as a lower-order rational function[63, 64, 82, 83, 85, 105, 106] in the generalized MoC approach. Specifically, the delay term can be extracted from $\mathbf{H}(s)$ and delayless propagation operator is denoted as $\mathbf{Q}(s)$. Then $\mathbf{Q}(s)$ and $\mathbf{Z_C}(s)$ are approximated to lower-order rational funtions as

$$\mathbf{Z_C}(s) = \mathbf{Z}_\infty + \sum_{i=1}^{N} \frac{\mathbf{S}_i}{s+p_i}; \quad \mathbf{Q}(s) = \mathbf{Q}_\infty + \sum_{i=1}^{N} \frac{\mathbf{S}_i}{s+p_i} \qquad (2\text{-}6)$$

The approximations in (2-6) are generally generated by the well-known vector-fitting technique. Obviously, the frequency-domain rational function in (2-6) can be mapped back to the time domain. Now, converting (2-2) into time-domain expressions gives

$$\mathbf{V}(0,t) - \mathbf{z_C}(t) * \mathbf{I}(0,t) = \mathbf{h}(t) * [\mathbf{V}(l,t) - \mathbf{z_C}(t) * \mathbf{I}(l,t)] \qquad (2\text{-}7a)$$

$$\mathbf{V}(l,t) + \mathbf{z_C}(t) * \mathbf{I}(l,t) = \mathbf{h}(t) * [\mathbf{V}(0,t) + \mathbf{z_C}(t) * \mathbf{I}(0,t)] \qquad (2\text{-}7b)$$

with the inverse Laplace transformation

$$\mathbf{V}(s) \Leftrightarrow \mathbf{V}(t) \quad \mathbf{I}(s) \Leftrightarrow \mathbf{I}(t) \quad \mathbf{Z_C}(s) \Leftrightarrow \mathbf{z_C}(t) \quad \mathbf{H}(s) \Leftrightarrow \mathbf{h}(t) \qquad (2\text{-}8)$$

Obviously, this transformation could lead to tedious time-domain convolution computations. The recursive convolution is one way to this problem[107]. Another possibility is to use rational expressions in (2-6) to come up with equivalent circuit, which can be directly simulated in the circuit solver using integration engine[108].

Though delay extraction has markedly reduced the complexity of computation, the curve fitting for $\mathbf{Q}(s)$ will still be a challenge. Firstly, with increases of the number, length and

losses of TLs, $\mathbf{Q}(s)$ requires a higher order approximation to insure acceptable fitting errors. Furthermore, the delay extraction and rational approximation need to be evaluated many times when TLs are analyzed at different lengths. In addition, in the process of curve fitting, the potential loss of passivity may be generated due to errors.

2.2 Realization of the convolution calculation and nonlinear components using ABM in SPICE

The conversion of frequency-dependent parameters from laplace to time domain and convolution calculation in (2-7) are the main difficulties in the implementation process of modeling lossy MTLs. Here we resort to ABM feature of SPICE to realize the time-domain equations (2-7) in circuit solver directly.

2.2.1 Overview of ABM

SPICE is a circuit simulation program for general purposes, which can carry out several kinds of analyses[109]. For some devices or systems, the internal parameters are difficult or unnecessary to know, and the default values of off-the-shelf devices cannot meet the simulation requirements. In order to realize the modeling of complex devices and systems, there are three ways available in SPICE to extend the simulator: polynomial controlled sources, adding a new model by modifying the simulator code and using existing primitives to build a macromodel.

PSpice is a kind of circuit simulation software developed from SPICE, which is capable of an extension called analog behavioral modelling. The simulator can be used like a programming language to solve mathematical problems by transforming them to electrical circuits using controlled current or voltage sources. Behavior modeling is to develop a model for a system or system's components by describing their behavior from an external viewpoint. So behavior modeling can be used to create new devices' models and black-box models for complex systems. PSpice provides the ABM option as an alternative way to make flexible descriptions of components or systems using arbitrary transfer functions and/or lookup tables, and to realize the analysis of input and output characteristics of systems. In other words, a circuit segment can be modeled only by a mathematical relationship, and there is no need to design the segment component by component.

Common analog behavioral models are all stored in the abm.olb library. According to [110], the ABM parts are classified as either control system parts or PSpice-equivalent parts. Control system parts provide basic realization functionality and do not require additional definitions in most cases. We will skip the detailed discription of them because of their simple application, and only concentrate on modules of PSpice-equivalent parts related with the treatment of the macromodel of lossy MTLs.

PSpice-equivalent parts have a differential input and a double-ended output. The parts include E-type and G-type devices, which have two pins for each controlling input and output. Table 2.1 sums up the common PSpice-equivalent parts. A series of expansion functions are adopted in ABM structure to extend controlled voltage and current sources, so that they are no longer controlled by only one or a few node voltages and currents. Complex control laws can also be realized by mathematical expressions (VALUE), look-up tables (TABLE), frequency-domain transfer functions (LAPLACE), and frequency-domain response tables (FREQ).

For such devices, the general SPICE syntax is:

E/G<name>   <+node>   <-node>   <keyword>   <function>

where the nodes indicate the port defining the controlling voltage or current, and the keyword specifies the device type to be used, such as the VALUE, LAPLACE and so on. The function introduces a formula or a table of the transfer function. The usage and features of these devices are briefly described below, some examples are also provided here to illustrate their functions.

Table 2.1 PSpice-equivalent parts in ABM

Category	Parts	Description
	E/GVALUE	arithmetic expression
Mathematical expression	E/GSUM	adder
	E/GMULT	multiplier
Table look-up	E/GTABLE	transfer function table
laplace transform	E/GLAPLACE	Laplace transform function
frequency-domain response table	E/GFREQ	frequency table look-up

(a) Square-root circuit   (b) Input and output signals of the EVALUE device
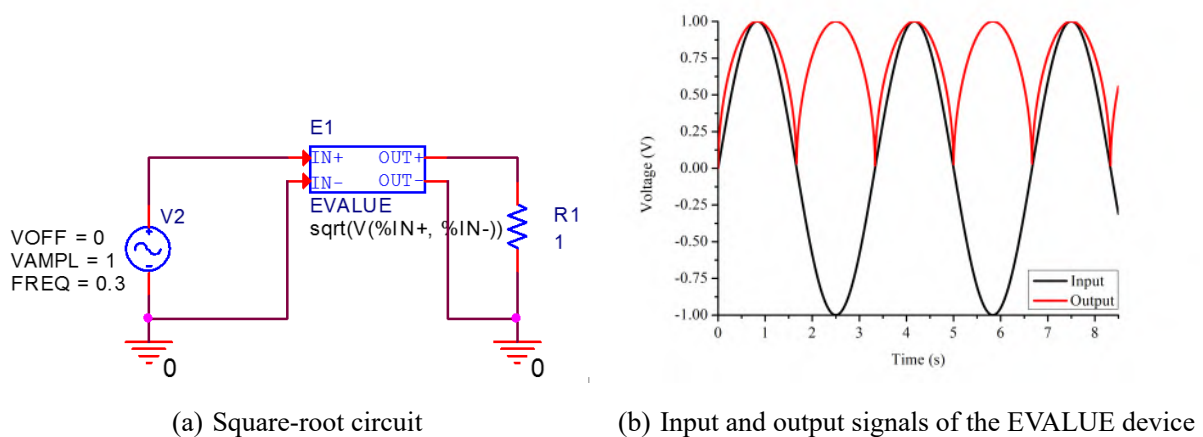
Figure 2.3 An example of the EVALUE part

1) E/GVALUE parts

The E/GVALUE parts enable an instantaneous function to be written in the form of a mathematical expression using the standard notation. Figure 2.3 shows an example of the EVALUE device, in which the output is the square root of the input voltage. An available simple solution is to use a feedback circuit to calculate square roots. But this method fails when the reference signal goes negative. The solution then is to use the functional form as:

E1 OUT+ OUT- VALUE = {SQRT(V(IN+, IN-)}

Except for voltages, E/GVALUE sources also have the ability to evaluate expressions containing currents, time, math functions, etc.

2) E/GTABLE parts

The E/GTABLE parts use a table to describe a transfer function, so they are well-suited to model measured data or characteristics without analytical expressions. An example of a table declaration would be the following:

E1 OUT+ OUT- TABLE {V(IN+, IN-)} = (-1, -10) (1, 10)

Above device describes an ideal comparator. The E/GVALUE and E/GTABLE parts all belong to instantaneous models, which enforce a direct time-domain response to the input at each moment. So these techniques can be used to model both linear and nonlinear characteristics. How to model nonlinear characteristics with ABM feature in SPICE environment will be elaborated in the subsequent section.

3) E/GLAPLACE parts

E/GLAPLACE parts can describe a transfer function in Laplace domain. So only variable s can appear in the Laplace transformation. For example, the netlist declaration can be written as:

E1 OUT+ OUT- LAPLACE {V(IN+, IN-)} = {1/(1 + 0.001s)}

According to the analysis, the transfer function $1/(1 + 0.001s)$ describes a lossy integrator with a time constant 0.001 s. Instead, the integral calculation can also be implemented by an RC-pair circuit with a time constant 0.001 s. Figure 2.4 shows this example, and the results of these two realization are also compared.

4) E/GFREQ parts

If there is no analytical Laplace description of the transfer function, the E/GFREQ parts, in which the frequency response are described by a table, can be adopted as the substitution. The syntax in the magnitude/phase form is:

E/G<name> <+node> <-node> FREQ {expression} (f(Hz), mag(dB), phase(degree))

(a) RC-pair integral circuit   (b) Input and output signals
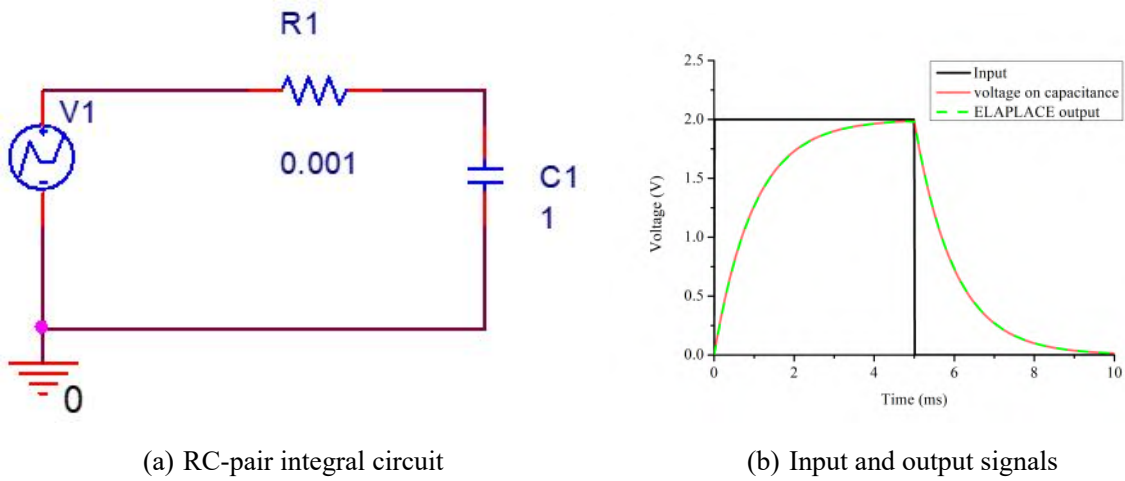
Figure 2.4 An example of the ELAPLACE part
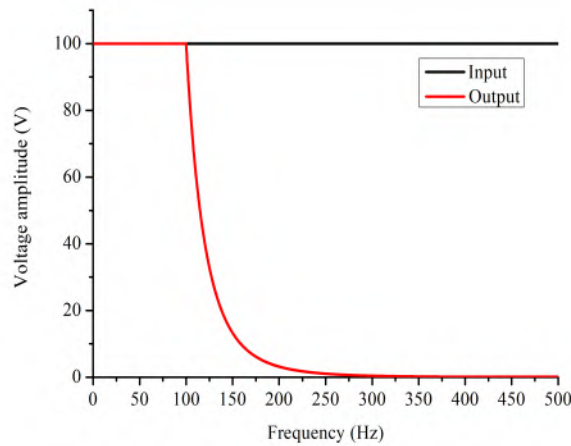
Figure 2.5 An example of the EFREQ part

There is an example defined by:

E1 OUT+ OUT- FREQ {V(IN+, IN-)} = (0,0,0) (100, 0,-180) (400 -60,-360)

The above EFREQ device describes a low-pass filter. Its response is 1 (0 dB) when frequencies are below 100 Hz and for frequencies above 400 Hz, the response becomes 0.001 (-60 dB). The frequency response for AC analysis is shown in figure 2.5.

The E/GLAPLACE and E/GFREQ parts all belong to frequency-domain models, so their output depends not only on the current input but the input history. Hence, different from E/G-VALUE and E/GTABLE parts, they are non-instantaneous models. The output of E/GLAPLACE and E/GFREQ devices varies with analysis types. During AC analysis, the frequency-domain responses are determined by the complex gain at each frequency; while for DC analysis, the gain is the response at the frequency zero; particularly, the output of the device is the convolution of the input and impulse response of the transfer function during transient analysis. The last property is appropriate to be used to realize convolution calculations in equation (2-7), and

the explicit modeling process will be introduced in the next section.

2.2.2　Realization of the time-domain convolution calculation in SPICE

As mentioned in section 2.1, in order to realize the macromodel for MTLs, the convolution calculation in equation (2-7) is a challenge. Except for the recursive convolution, there are several available methods to this problem, which will be presented in this section.

1) Equivalent circuit

The most common method is to develop equivalent circuits for rational expressions. For clarity, and without loss of generality, we firstly consider the characteristic impedance of three-conductor TLs, whose rational functions of elements in $\mathbf{Z_C}(s)$ matrix can be written as

$$Z_{c,ij} = R_{dc,ij} + \sum_{k=1}^{N} \frac{S_{ij,k}}{s - P_{ij,k}}(1 \leq i \leq 3, 1 \leq j \leq 3) \tag{2-9}$$

where $R_{dc,ij}$ denotes the direct current resistance. The $P_{ij,k}$ is the pole of $(Z_{c,ij} - R_{dc,ij})$, and the corresponding residue is $S_{ij,k}$. The diagonal elements in $\mathbf{Z_C}(s)$ matrix are self-impedances for each line, they can be equivalent to a series of subcircuits which are composed of a DC resistance in series with subnetworks including a resistance $R_{ii,k} = -(S_{ii,k}/P_{ii,k})$ paralleling with a capacitance $C_{ii,k} = 1/S_{ii,k}$. The off-diagonal elements of $\mathbf{Z_C}(s)$ matrix denote the coupling between lines, each of them can be realized by a current controlled voltage source, for which the controlling currents can be picked from branches modeled in the way as the diagonal elements. Figure 2.6 shows the equivalent circuit of term $\mathbf{z_C}(t) * \mathbf{I}(t)$ in (2-7) for three-conductor TLs, which can be directly solved in SPICE. So compared with the recursive convolution, the equivalent circuit is more convenient and efficient in the process of macro-model implementation on the premise that irrational functions of s have been approximated accurately.

2) LAPLACE parts in ABM

We have known from section 2.2.1 that the PSpice simulator is equipped with ABM function, with which general mathematical problems can be solved using circuit elements directly. Among existing ABM parts, frequency-domain E/GLAPLACE parts are capable of evaluating Laplace transform functions with variable s. And in particular, during transient analysis, the value of output is the convolution of past values of the input with the transfer function's impulse response. Hence, an available method is proposed here to calculate convolutions in SPICE.

The LAPLACE part requires a Laplace transform description in the form of exponential function or fractional function, in which the exponential term, numerator and denominator all
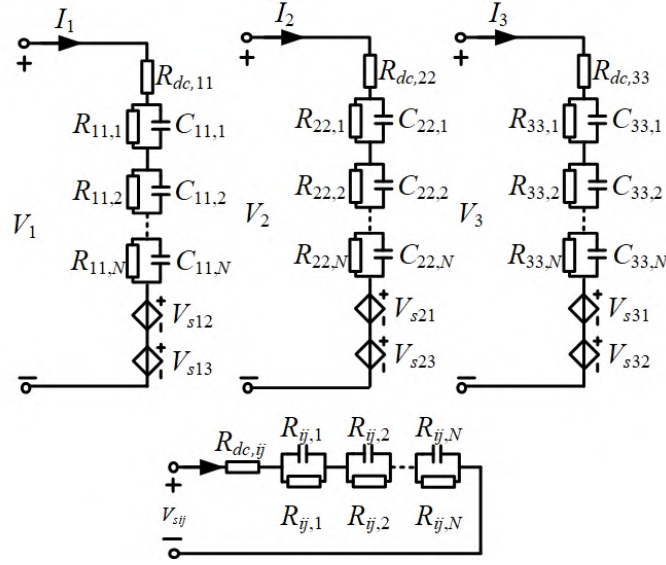
Figure 2.6 An equivalent circuit of the convolution calculation

$$E_{sij} = z_{cij}(t) * I_j(t)$$
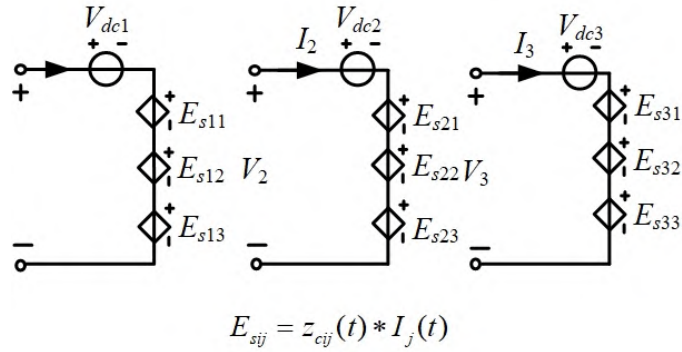
Figure 2.7 An ABM realization of the convolution calculation

follow the rules of the standard mathematical expression, along with arithmetic operators and parentheses. Therefore, though characteristic impedance $\mathbf{Z_C}(s)$ and propagation operator $\mathbf{H}(s)$ are irrational functions of s for cases of lossy TLs, the rational approximation is dispensable to model them using LAPLACE part. Once the analytical expressions of $\mathbf{Z_C}(s)$ and $\mathbf{H}(s)$ are composed of available built-in functions in SPICE solver, the term $\mathbf{z_C}(t) * \mathbf{I}(t)$ in (2-7) for three-conductor TLs can be realized simply by E/GLAPLACE, just as shown in Figure 2.7. These parts in Figure 2.7 produce several PSpice netlist declarations like this:

Eij OUT+ OUT- LAPLACE $\{I(V_{dcj})\} = \{f_{ij}(s)\}$

in which $f_{ij}(s)$ is the function with variable s, and $I(V_{dcj})$ is the current through a direct voltage source V_{dcj} with a value of 0. The adoption of 0-value DC voltage sources are convenient to sense currents in definitions of these controlled voltage sources.

3) FREQ parts in ABM

In addition to LAPLACE parts, the E/GFREQ parts are also frequency-domain models, but they are featured by a table of frequency responses instead of Laplace transform functions. Just as mentioned in the former section, the FREQ parts follow the same calculation rules with LAPLACE parts, while the analytical Laplace transfer functions are not a necessity anymore. So this unique property will be utilized to model devices which can only be characterized by discrete frequency response tables obtained by measurement or empirical formulae, etc.

Table 2.2 Parameters of FREQ parts in ABM

Properties	Description
EXPR	input value used for table lookup
TABLE	series of triplets describing a complex value
R_I	table type
DEDLAY	group delay increment
MAGUNITS	units for magnitude
PHASEUNITS	units for phase

Significantly, there are several property parameters of FREQ parts to be defined in the netlist declaration, which have been listed in Table 2.2. Among parameters in Table 2.2, the DELAY property is of great value in defining parts, which is particularly useful when SPICE generates a warning of non-causality. Hence, corresponding to LAPLACE parts, there will be several PSpice netlist declarations for models in Figure 2.7 using FREQ parts:

Eij OUT+ OUT- FREQ $\{I(V_{dcj})\}=$

$(f_1(\text{Hz})\ mag_1(\text{dB})\ phase_1(\text{degree}),$

$+ \cdots$

$f_k(\text{Hz})\ mag_k(\text{dB})\ phase_k(\text{degree}),$

$+ \cdots$

$f_N(\text{Hz})\ mag_N(\text{dB})\ phase_N(\text{degree}))$

in which $I(V_{dcj})$ is the voltage source with a value 0 for sensing current. The specified table is read in and converted to a time-domain response by means of a standard inverse Fourier transform method.

2.2.3 Modeling of the nonlinear device in SPICE

There are many nonlinear components in TL systems, served as the surge protection device (SPD), whose main role is to discharge and limit voltage, such as MOV. It should contain at least one nonlinear component, and are used to suppress many kinds of over-voltages.

In order to consider the influence of nonlinear devices on transient responses of MTLs, taking the MOV as an example, this section will focus on equivalent circuit models of nonlinear characteristics which could be solved in SPICE. Actually, the netlist files of SPICE circuit models for some nonlinear devices have been offered by their manufacturing companies. It can be downloaded from the website, and incorporated into PSpice just by slight modifications. Nevertheless, code redundancy of these file may lead to low analysis efficiency, and not all nonlinear components are provided with SPICE model netlists conveniently. Hence, the features including response time and V-I characteristics of nonlinear devices are extracted as the main features to model devices. Other aspects are ignored or eliminated for optimization and simplification.
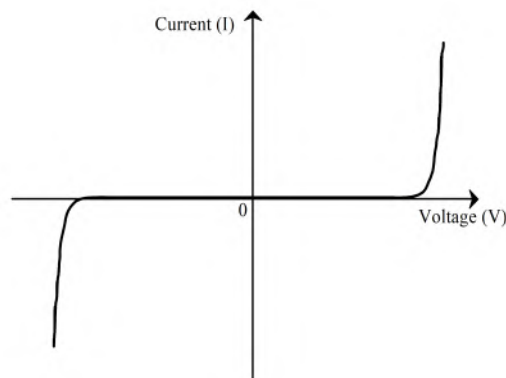
Figure 2.8 The V-I characteristic of varistors

The V-I characteristics of varistors are continuous and increasing, which is shown in Figure 2.8. The varistor is in a state of high resistor when it is in normal working condition, while when the surge invades, high current will flow through itself and leak into the earth. The modeling process will be presented in two parts, covering modeling the nonlinear V-I characteristic (nonlinear resistance), and modeling complete model considering dynamic property.

1) Nonlinear resistances modeling

As we know, any resistance can be thought of a current-controlled voltage source, correspondingly, a conductance can be equivalent to a voltage-controlled current source. And a resistance and a conductance can be mutually transformed. Hence, the E-type and G-type sources can be adopted to model nonlinear resistances (or conductance) by creating transfer functions for sources.

If the V-I characteristic of a nonlinear device can be expressed mathematically as nonlinear functions $V = f(I)$ or $I = f(V)$, the nonlinear V-I characteristic can be modeled by

E/GVALUE parts, as shown in Figure 2.9, with netlist declaration:

E1 OUT+ OUT- VALUE = $\{f(I(V1))\}$

G1 OUT+ OUT- VALUE = $\{f(V(OUT+, OUT-))\}$

The controlling nodes are identical to the output nodes. DC source V1 is used to obtain the current flowing through E1.

(a) EVALUE   (b) GVALUE
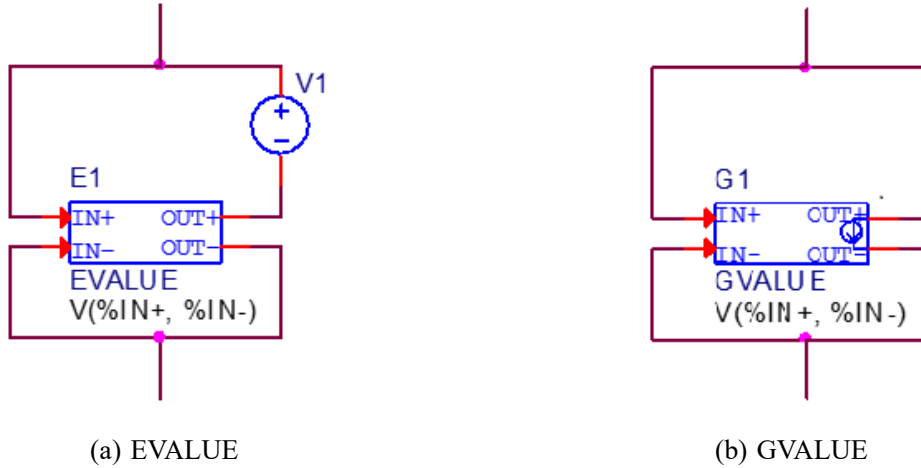
Figure 2.9 E/GVALUE realization of the nonlinear V-I characteristic

For nonlinear devices created in the above way, there are a few things we must be cautious about. First, the current flowing through the practical impedance equals to zero when voltage is zero. Second, we may obtain devices which can generate power though the real one may not operate at such voltages. Generally, it is a good choice to use TABLE parts in ABM as an available option to limit the output of devices. Because the output of the device equals to a constant whose value is the smallest (or largest) in the input table when values are out of the table's input range. This unique feature can be used to set an upper and lower limit to the output. Besides, these TABLE parts are well suited for V-I curves obtained by measured data, which can only be expressed using piecewise linear approximation.

The V-I characteristic of nonlinear devices has been realized. The complete model will be discussed in the next part.

2) The simulation model of MOV

In the last decades, a number of models for MOVs have been proposed[111–113], among which the model in [113] built with diodes in opposite direction is widely employed, as shown in Figure 2.10.

In Figure 2.10, L_s takes into consideration the internal inductance and the terminal inductance, of about 10 nH/m, C_p is a parallel capacitance with a value of hundreds to thousands of pF, here the typical value 1.5 nF is adopted. The dynamic effects are contained by means of L_s and C_p. R_p is a large resistance in hundreds MΩ used to approach the V-I character-

24
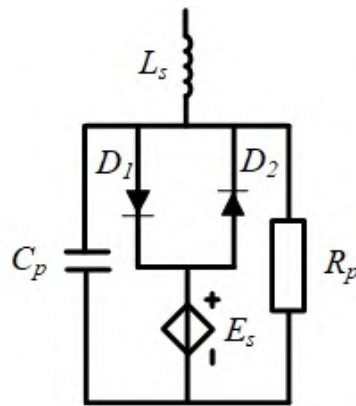
Figure 2.10　An equivalent model of the MOV

istic in low currents (non-conduction zone) and reflect the leakage current. Two diodes and the voltage-controlled voltage source E_s govern the nonlinear V-I characteristic. So the key point of model in Figure 2.10 is to specify the parameters of diodes (breakdown knee voltage voltage, saturation current and parasitic resistance) in SPICE, and the control coefficient of the controlled source, which are usually calculated by the electrical parameters obtained through test. Besides, in order to obtain a better fitting to the V-I curve, the numerical algorithm is adopted to search the optimal parameters of diodes and the controlled source. For reducing the number of model parameters to be set beforehand and simplifying the modeling process on the premise of model accuracy, the circuit branch of diodes and voltage source is replaced by behavior devices, as shown in Figure 2.11.
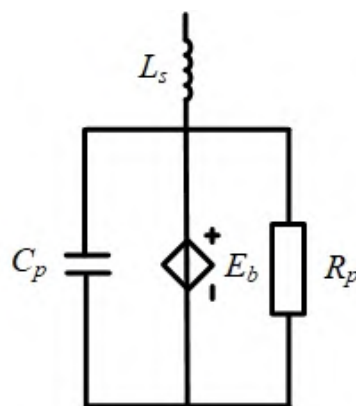
Figure 2.11　An equivalent behavior model of the MOV

The equivalent model in Figure 2.11 is universally applicable for protective devices possessing different characteristic with the same principle, which is convenient for redevelopment once the main features characterized by device parameters or experimental data have been obtained.

2.2.4 Numerical validation of the behavior model

In order to verify the proposed behavior models, different examples will be set in this section with respect to realization of convolution calculation and nonlinear devices in SPICE, and the results are compared with those of other methods. In addition, simulation times for different methods are also compared to illustrate the efficiency of advocated models. In the following part, two examples are investigated and simulated by PSpice on a PC equipped with an INTEL i7 3.6-GHz CPU.

1) Example 1: time-domain convolution

This example considers an overhead single-conductor line above the lossy ground, which refers to a line placed at a height of 0.8 m with ground conductivity σ_g being 0.1 S/m, and the conductor's radius is 0.001 m, as shown in Figure 2.12. We have known that the characteristic impedance Z_C of the line is determained by parameters including the height and radius of the conductor, and the ground conductivities. Apparently, it is frequency-dependent due to lossy ground.
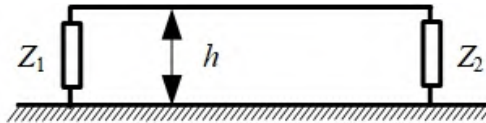
Figure 2.12 An overhead single-conductor line above the lossy ground

In order to model Z_C in SPICE, three modeling methods presented in section 2.2.2 are utilized in this example. Firstly, using .AC command, the amplitude and phase frequency characteristics of three models are obtained and shown in Figure 2.13. The fitting order of rational approximation for Z_C is selected as 8 here, that is, there are 8 subnetworks in the equivalent circuit. For FREQ part, the number of frequency samples $NFFT$ is 1024. The frequency responses of three different models agree well with the results of numerical calculation.

Then, in order to study transient responses of three models in time domain, Figure 2.14 compares the voltage responses of different models when this impedance is excited by a double-exponential current pulse as the load. From Figure 2.14, the transient responses of three models coincide with each other. Table 2.3 contains the comparison of simulation times, and the differences are narrow between these models. It should be noted that this comparison result is not of universality, because the efficiency of the equivalent circuit based on the rational approximation will reduce with the increase of the model complexity, that is, the order of rational expressions.

The above example demonstrates the validity and efficiency of behavior models. Besides, there are several factors to influence their accuracy and efficiency, including frequency reso-

(a) Amplitude-frequency curves of Z_c (b) Phase-frequency curves of Z_c
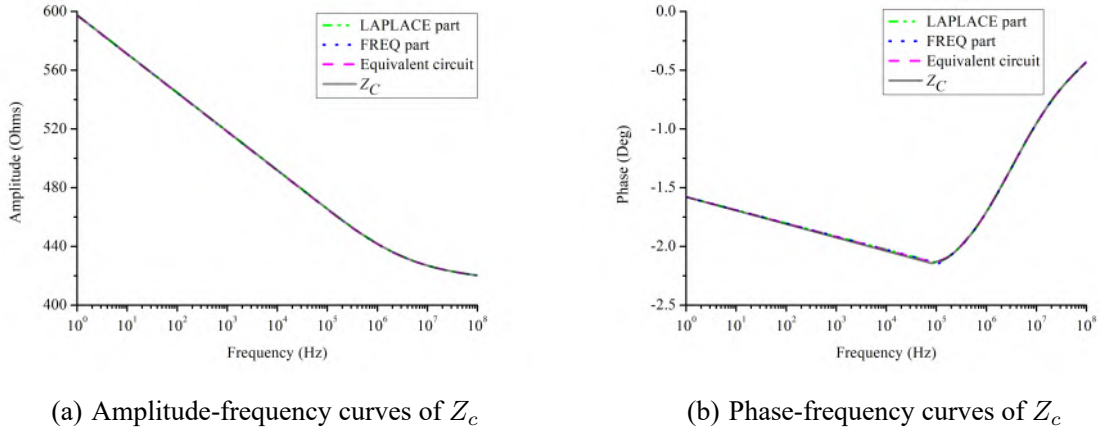
Figure 2.13 The frequency responses of three models for Z_c
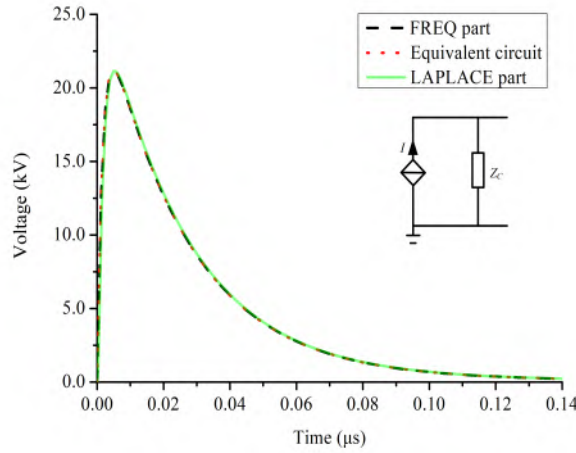
Figure 2.14 The transient responses of three different models for Z_C

Table 2.3 The comparison of simulation times for three models

Models	Equivalent circuit	LAPLACE part	FREQ part
Simulation Time (s)	4.61	4.53	4.73

lution and the maximum frequency of the look-up table in FREQ part, and transient analysis parameters, etc. Hence, how to choose these parameters to trade off the accuracy with the efficiency of ABM parts will be specifically discussed in the subsequent section.

2) Example 2: nonlinear device models

We select a MOV in model V120za20 (Littlefuse ZA series), whose netlist file of SPICE has been offered by its manufacturing company. According to the sub-circuit file, the circuit model is composed of several custom capacitances, resistances, diodes, controlled sources,

and so on. It can be incorporated into PSpice just by slight modifications, and is regarded as the reference model here. In this example, the equivalent model in Figure 2.10 and behavior model in Figure 2.11 are adopted, V-I characteristics and transient responses are studied and compared with the results of the reference model.

For V120za20, the parameters of circuit component L_s, C_P and R_P in Figure 2.10 and Figure 2.11 are set as 10 nH, 1.5 nF, and 100 MΩ, respectively. The voltage across the model is fit as a mathematical expression

$$V = A \cdot [26\text{mV} \cdot \ln(I/I_s) + I \cdot r_s] \tag{2-10}$$

where control coefficient A is 181.8182, I and V is the current and voltage, r_s represents the parasitic resistance of diode with the value of 140 μΩ here, I_s is 10^{-14} A representing the saturation current of diode in this case. So the controlled voltage source EVALUE can be defined in ABM, in which the equation (2-10) is used as transfer function directly. Figure 2.15 shows the V-I characteristic comparison between different models. It can be observed that curves are very close to each other in the active zone.
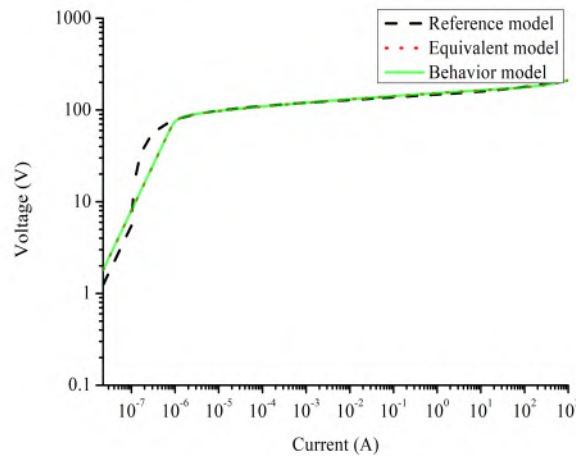
Figure 2.15 The V-I characteristic comparison between different models

Table 2.4 The comparison of simulation times for different models

Models	Reference model	Equivalent model	Behavior model
Simulation Time (s)	0.25	0.16	0.09

Figure 2.16 shows the comparison between transient voltage responses of different models when they are excited by a 1.2/50 μs current surge. Table 2.4 lists the simulation times of different models. We should note that the behavior model of the nonlinear MOV device allows
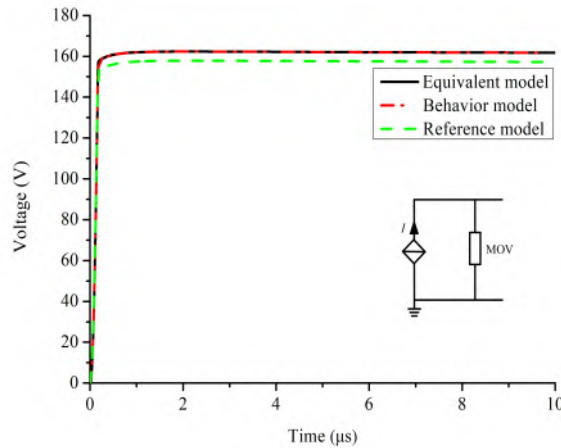
Figure 2.16 The transient voltage responses of different models for the MOV

us to obtain a good fitting to the V-I characteristic and transient response, and an improvement in the simulation efficiency compared with those of the present netlist and the original equivalent circuit model.

2.3 Some key tips and constraint analysis for the use of the frequency-domain parts in ABM library

Any ABM device adopted in the former section calls for robust and accurate modeling, which means that it must be precisely defined over a required wide frequency range, in order that its effect on the response of the input signal can be assessed. As mentioned above, during transient analysis, frequency-domain models follow the standard method of inverse Laplace or Fourier transforms. However, transforming back and forth between the time and frequency domain requires extreme caution under the standpoint of the model builder, especially performed by circuit solvers blindly.

In this section, several key tips and constraints that are involved in the implementation of frequency-domain LAPLACE and FREQ parts during transient analysis are discussed, since both VALUE and TABLE are instantaneous devices, with which the transient analysis is straightforward. In order to mainly focus on specific and readily comprehensible results, the theoretical analysis is interspersed with several simple examples.

2.3.1 The processing on non-causal impulse responses

For frequency-domain parts, PSpice applies a standard inverse fast Fourier transform (FFT) to the transfer function to gain an impulse response, and then it is convolved with the input signal during the transient analysis. Some impulse responses are inherently non-causal,

which means that both past and future input signals must be included in the convolution to accurately represent the inverse transformation of the Laplace-domain transfer function. Here is an example, we specified a transfer function $\{e^{-s\times1.6677e-07}+e^{s\times1.6677e-07}\}$ for LAPLACE device. The impulse response of $\{e^{-s\times1.6677e-07}+e^{s\times1.6677e-07}\}$ is an impulse pair separated by the double of transition time $1.6677e-07$ s, which is the time electromagnetic wave takes to propagate 50 m in free space. One of the impulse pair is situated in the past, the other is in the future, which correspond to a combination of backward and forward shift in time domain. In order to interpret this example more clearly, we apply an voltage pulse as the input of a GLAPLACE device, as shown in the Figure 2.17(a), in which the transfer function is defined as $\{e^{-s\times1.6677e-07}+e^{s\times1.6677e-07}\}$. The input waveform and the corresponding current response flowing through GLAPLACE are also shown in Figure 2.17(b).
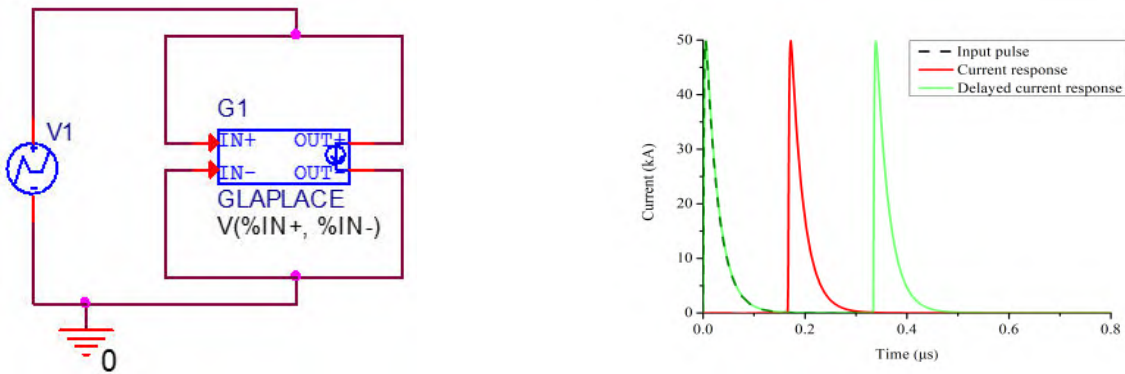
(a) The GLAPLACE device with a non-causal impulse response

(b) The input signal and current responses of GLAPLACE

Figure 2.17 An example of GLAPLACE with a non-causal impulse response

The problem now is that there are only present and past values of the input in the simulator, so from Figure 2.17, the input waveform is only delayed from $t=0$ to $t=1.6677e-07$ s (denoted by red solid line), implying that only half of the impulse pair is applied during convolution. Fortunately, PSpice is capable of detecting and issuing a warning message for users, in which what percentage of non-causal impulse response and how much delay needed to slide the non-causal part are shown. For the case of $\{e^{-s\times1.6677e-07}+e^{s\times1.6677e-07}\}$, there is 50 % non-causal impulse response, and a delay of $1.67344e-07$ s is required. The delayed current response is also shown in Figure 2.17(b) denoted by green solid line. It is obvious that the entire waveform of the current response is slided to the right of $t=0$, so the impulse response becomes causal.

In conclusion, during transient analysis, PSpice can only assess the convolution of causal impulse responses with input signals without any reprocessing. Though the suggested delay can be performed to keep impulse responses causal, it may also produce spurious results due to consequent uncontrollable factors, especially for frequency-domain parts in a large-scale

system model. Because of this reason, it is better to apply the causality test[89] for impulse responses of frequency-dependent parts firstly,Then, it is suggested to implement non-causal transfer functions or frequency responses by equivalent circuits instead of behavior models.

2.3.2 Criteria of selecting the maximum frequency and frequency resolution of FREQ response tables

It is worth to be noted that, though the scale of the response table is not limited in PSpice, the choice of appropriate frequency range (maximum frequency) and resolution has a great influence on the simulation results of FREQ devices. As previously mentioned, for frequency-domain devices, the output is the convolution of the input and the impulse response during transient analysis, whose paradigmatic expression is written as

$$y(t) = h(t) * x(t) = \int_{-\infty}^{+\infty} h(t - \tau)x(\tau)d\tau \tag{2-11}$$

in which $x(t)$ is the input, $h(t)$ is the time-domain impulse response and the output is denoted by $y(t)$. The discretization of the (2-11) yields

$$y(k\Delta) = \Delta \sum_{m=0}^{k} x(m\Delta) \cdot h[(k - m) \cdot \Delta], \ k = 0, 1, 2... \tag{2-12}$$

where Δ is the time step and k is the time index. The impulse response can be obtained from the discrete form of the inverse Fourier integral:

$$h(m\Delta) = \frac{1}{P \cdot \Delta} \sum_{p=0}^{P-1} H(f_p) \cdot e^{\frac{j2\pi pm}{P}}, \ m = 0, 1, 2, ..., P - 1 \tag{2-13}$$

In this expression, P represents the number of equally-spaced frequency samples of the transfer function, and $H(f_p)$ is provided to SPICE by means of the FREQ table. P is required to be a power of 2. The discrete frequencies f_p are defined by

$$f_p = \frac{p}{P \cdot \Delta}, \ p = 0, 1, 2, ..., P - 1 \tag{2-14}$$

and the Nyquist critical frequency $f_c = f_{P/2} = \frac{1}{2 \cdot \Delta}$, and the terms for $p > P/2$ represent the transfer function for negative frequencies. Since the negative frequency responses are the image of the positive ones, only $P/2$ frequency points are required to evaluate (2-13). According to a well-known result of sampling theory, the larger f_c is, the more accurate the transient analysis results are. However, for larger f_c, a smaller Δ is required, and the computation time increases. Hence, this section is devoted to the criteria of selecting reasonable maximum fre-

quency f_{MAX} and frequency resolution Δf of FREQ response tables considering simulation properties of PSpice.

One point we must illuminate firstly: in PSpice, the maximum time $TSTOP$ is the length of transient analysis. For frequency look-up tables, f_{MAX} is twice the highest frequency value f_c in the table, and the frequency resolution Δf is designated as the smallest increment of the frequency table. For convenience, the frequency samples are usually equally-spaced in the frequency domain starting from 0. The time resolution Δ is the reciprocal of the f_{MAX}.

For example, we consider a transform $e^{-s \times 1e-7}$ here, which represents an ideal delay of 0.1 μs. The frequency response table of a voltage source EFREQ can be defined by $e^{-s \times 1e-7}$ with $f_c = 4 \times 10^8$ Hz, and 4096 frequency samples. The input of EFREQ is a double exponential pulse realized using piecewise linearity source in PSpice for which the time resolution is 0.1 ns. We firstly set the transient analysis parameter $TSTOP$ as 1 μs. In order to validate the results, an ideal TL model in PSpice is also adopted in this example as a reference to realize the delay. The responses of both input and output are shown in Figure 2.18(a). It is obvious that the voltage response of EFREQ agrees not very well with the reference response. According to the above analysis, the maximum frequency f_{MAX} for the EFREQ device in this example is 8×10^8 Hz, which means that the time resolution Δ is 1.25 ns. It is approximately 10 times the time resolution of the input pulse, and this leads to inaccuracy of the output response. We change f_c of the table to 1×10^9 Hz, and all other parameters are fixed. In this circumstance, the time resolution Δ becomes 0.5 ns, which is comparable with that of the input pulse. The modified voltage response of EFREQ is also depicted in Figure 2.18(b).

Therefore, the frequency range of response tables is limited by the time resolution of input signals. Specifically, the time resolution of the impulse response, which is the inverse of the f_{MAX}, must be comparable or in the same order of magnitude with the time resolution of input signals.

Then we will study the influence of frequency resolution Δf or the number of frequency samples of response tables on the output results of FREQ. The f_c of response table for above example is again changed to 2×10^9 Hz, and all other parameters are fixed. Figure 2.19(a) shows the output response of EFREQ compared with the reference response. Though the f_{MAX} meets the requirement, the output of EFREQ is unexpected. We then reset the $TSTOP$ of transient analysis as 0.8, 0.6, 0.5 and 0.4 μs, respectively. The corresponding results are shown in Figure 2.19(b). We figure out that the frequency resolution Δf or the number of frequency samples of response tables have a great influence on transient responses of FREQ devices. And the number of frequency samples must meet the condition

$$\frac{NFFT}{2 \times f_{MAX}} = \frac{P}{4 \times f_{MAX}} > TSTOP \tag{2-15}$$
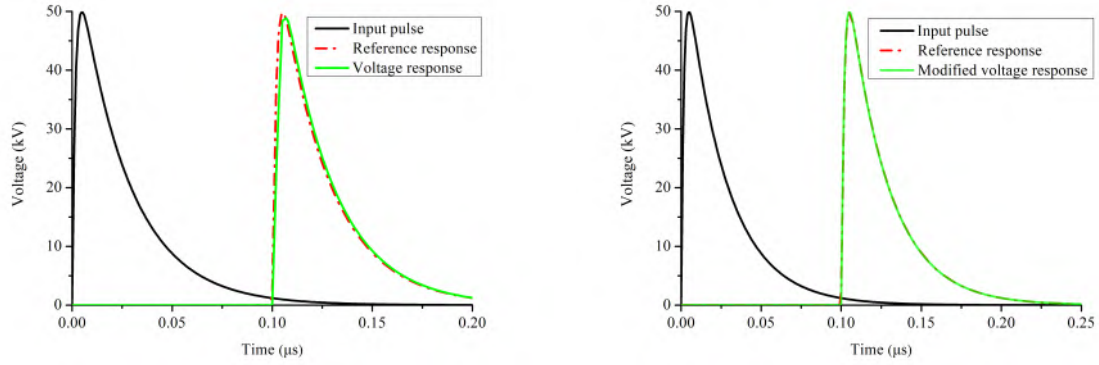
(a) The voltage response of EFREQ with the original table

(b) The voltage response of EFREQ with the modified table

Figure 2.18 The input pulse and voltage responses of EFREQ for different maximum frequency

where $NFFT = P/2$ is the number of frequency samples. In above example, when $f_c = 2 \times 10^9$ and $NFFT = 4096$, the $TSTOP$ must be less than $\frac{NFFT}{2 \times f_{MAX}} = \frac{4096}{2 \times 4 \times 10^9} \approx 0.512$ µs. We can find out from Figure 2.19(b) that voltage responses agree very well with the reference response when $TSTOP$ is equal to or less than 0.5 µs.
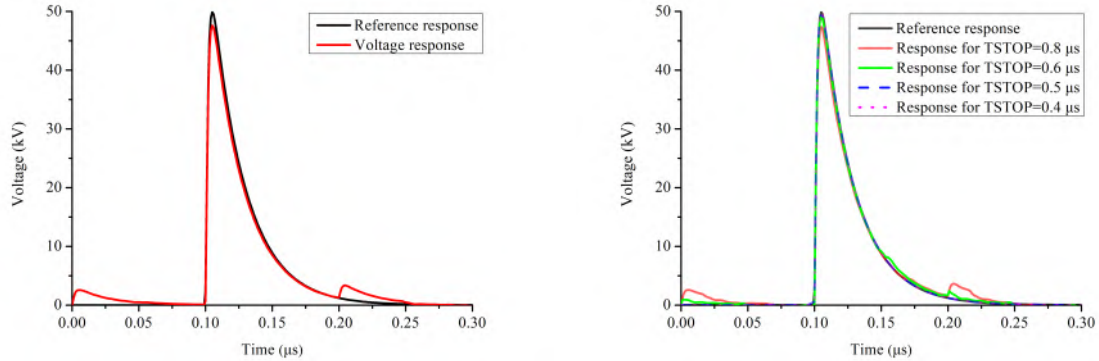
(a) The voltage response of EFREQ with $TSTOP = 1\mu s$

(b) The voltage response of EFREQ with different $TSTOP$

Figure 2.19 The transient voltage responses of EFREQ for different maximum time

Based on above analysis, the response accuracy of FREQ devices highly depends on parameters of look-up tables and transient analysis, including f_c, $NFFT$ and $TSTOP$. On the premise that $TSTOP$ is determined, then parameters of tables can be evaluated using following procedures with criteria:

1. The frequency range f_c of the response table must be evaluated first of all, ensuring the time resolution of the impulse response $\Delta = 1/2/f_c$ is comparable or in the same order of magnitude with the time resolution of input signals;

2. The number of frequency samples are better matched to the nearest power of 2, which

must meet the inequality condition: $\frac{NFFT}{4 \times f_c} > TSTOP$.

2.3.3 Simulation cautions for Laplace transformation

For Laplace devices, different from frequency tables, PSpice starts with initial bounds on the Δf and f_{MAX}, which are determined by transient parameters.

The Δf is originally set below $0.25/TSTOP$ and is then chosen as large as possible without inducing sampling errors. The initial upper bound of f_{MAX} is $1/(RELTOL \times TMAX)$, where $TMAX$ is the transient analysis step ceiling value. The $RELTOL$ is the relative accuracy of all calculated voltages and currents, the default is 0.001.Then PSpice trys to reduce the f_{MAX}. One way is to search for the frequency, at which the impulse response falls to maximum response times the $RELTOL$. While for transforms that don't have high limit, such as $e^{-s \times 1e-7}$, there is an another limit of $10/(RELTOL \times TSTOP)$.

Similar to frequency tables, in order to ensure the accuracy during transient analysis, the key point we must consider is that the time resolution of the impulse response $\Delta = 1/f_{MAX}$ is comparable or in the same order of magnitude with the time resolution of input signals. Hence, the $TSTOP$ and time resolution of input signals constraint with each other, and once the one of them is fixed, the other one must be adjusted based on the constraint condition.

2.3.4 The trade-off between accuracy and efficiency of frequency-domain parts

Except for ensuring the accuracy of frequency-domain parts, the efficiency or computation time is also a significant aspect. So the trade-off between accuracy and efficiency of frequency-domain parts will be discussed as follows.

We firstly focus on the computation efficiency of frequency-domain parts, a delay transform $e^{-s \times 1e-7}$ is also adopted here as an example. The $e^{-s \times 1e-7}$ is realized by a ELAPLACE part, and a EFREQ response table, respectively. Similarly, the response of an ideal TL model in PSpice is served as a reference. In order to make sure the fairness of the efficiency comparison, the input signal with Δ being 0.1 ns and $TSTOP$ being 1 μs are same for these three devices. Apparently, the $TSTOP$ meet the accuracy requirement of Lapalce devices ($RELTOL \times TSTOP/10 = 0.1$). Then, in accordance with criteria in 2.3.2, the f_c of response table is set to be 1×10^9 Hz, and sampling number $NFFT$ must be larger than 4000. It is well-known that the larger $NFFT$ is, the more accurate the response of EFREQ is, but we have to compromise on efficiency. So $NFFT$ is chosen to be 4096, which is the nearest power of 2 larger than 4000. The voltage responses of above delay devices are shown in Figure 2.20, in which they have a great agreement with each other. Then the simulation times are compared in Table 2.5. It is clear that the frequency-domain parts have a prominent advantage on

the efficiency, in particular, LAPLACE parts are slightly faster than FREQ parts. In addition, considering the modeling process of LAPLACE and FREQ, once the frequency response can be described by a transfer function, we can conclude that the LAPLACE is more convenient and preferable to calculate the convolution during transient analysis.
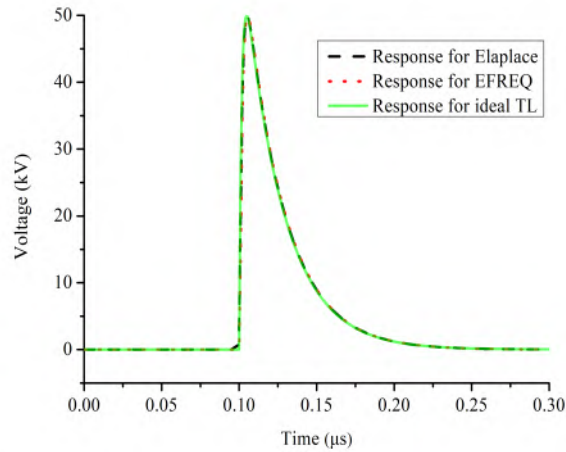
Figure 2.20 The voltage responses of three delay devices

Table 2.5 The comparison of simulation times for three delay devices

Devices	ELAPLACE	EFREQ	Ideal TL
Simulation Time (s)	1.37	1.42	2.64

According to above analysis, we list several recommendations for adopting frequency-domain models in transient analysis.

1. It will be preferable to choose E/GLAPLACE devices if a Laplace transform in the form of standard mathematical expression is available;

2. The E/GFREQ devices is utilized to model frequency responses that can only be characterized by discrete frequency response tables obtained from measurement or empirical formulae, etc. The response table must be prudently defined in terms of criteria proposed above, and $NFFT$ needs to be as small as possible under the given conditions;

3. The computation time and memory scale of PSpice is approximately inverse to $RELTOL$. Hence, except for the proper chosen of simulation models, we can also loose the $RELTOL$ to 0.01 instead of default 0.001;

2.4 Derivation of the time-domain macromodel for MTLs

In this section, the modeling of the MoC algorithm is presented. The formulation of the macromodel for MTLs is described in terms of p.u.l parameters.

2.4.1 Macromodel implementation

For cases of MTLs, the solution to TL equations can be expressed as (2-2), which are coupled together because $\mathbf{Z_C}(s)$ and $\mathbf{H}(s)$ are full matrices; that is, each set of voltages and currents affects all the other sets of voltages and currents. Decoupling with a similarity transformation is the essential idea in the solution method that we frequently use[114–116]. In implementation of the MoC, the equations in (2-2) are partially decoupled as

$$\mathbf{V}(x,s) = \mathbf{T}_V \overset{\wedge}{\mathbf{V}}(x,s); \quad \mathbf{I}(x,s) = \mathbf{T}_I \overset{\wedge}{\mathbf{I}}(x,s) \tag{2-16}$$

The $n \times n$ constant complex matrices $\mathbf{T}_V$ and $\mathbf{T}_I$ define a transformation between actual voltages and currents, $\mathbf{V}$ and $\mathbf{I}$, and mode voltages and currents, $\overset{\wedge}{\mathbf{V}}$ and $\overset{\wedge}{\mathbf{I}}$. They are selected such that they simultaneously diagonalize both $\mathbf{L}_\infty$ and $\mathbf{C}_\infty$ as[40]

$$\overset{\wedge}{\mathbf{L}}_\infty = \mathbf{T}_V^{-1}\mathbf{L}_\infty\mathbf{T}_I; \quad \overset{\wedge}{\mathbf{C}}_\infty = \mathbf{T}_I^{-1}\mathbf{C}_\infty\mathbf{T}_V; \quad \mathbf{T}_V^t = \mathbf{T}_I^{-1} \tag{2-17}$$

where $\overset{\wedge}{\mathbf{L}}_\infty$ and $\overset{\wedge}{\mathbf{C}}_\infty$ are diagonal matrices, and superscript t refers to the transpose of the matrix. Based on (2-16) and (2-17), (2-2) can be transformed to

$$\overset{\wedge}{\mathbf{V}}(0,s) - \overset{\wedge}{\mathbf{Z}}_\mathbf{C}(s)\overset{\wedge}{\mathbf{I}}(0,s) = \overset{\wedge}{\mathbf{H}}(s)[\overset{\wedge}{\mathbf{V}}(l,s) - \overset{\wedge}{\mathbf{Z}}_\mathbf{C}(s)\overset{\wedge}{\mathbf{I}}(l,s)] \tag{2-18a}$$

$$\overset{\wedge}{\mathbf{V}}(l,s) + \overset{\wedge}{\mathbf{Z}}_\mathbf{C}(s)\overset{\wedge}{\mathbf{I}}(l,s) = \overset{\wedge}{\mathbf{H}}(s)[\overset{\wedge}{\mathbf{V}}(0,s) + \overset{\wedge}{\mathbf{Z}}_\mathbf{C}(s)\overset{\wedge}{\mathbf{I}}(0,s)] \tag{2-18b}$$

where

$$\overset{\wedge}{\mathbf{H}}(s) = e^{-\overset{\wedge}{\mathbf{\Gamma}}(s)l} \tag{2-19}$$

and

$$\overset{\wedge}{\mathbf{\Gamma}}(s) = \mathbf{T}_I^{-1}\mathbf{\Gamma}(s)\mathbf{T}_V; \quad \overset{\wedge}{\mathbf{Z}}_\mathbf{C}(s) = \mathbf{T}_V^{-1}\mathbf{Z}_\mathbf{C}(s)\mathbf{T}_I \tag{2-20}$$

To model the propagation function, for generalized MoC, the delay terms are firstly extracted as

$$\overset{\wedge}{\mathbf{\Gamma}}(s) \approx s(\overset{\wedge}{\mathbf{L}}_\infty\overset{\wedge}{\mathbf{C}}_\infty)^{1/2} + \overset{\wedge}{\mathbf{M}}(s) \tag{2-21}$$

However, $(\hat{\mathbf{L}}_\infty \hat{\mathbf{C}}_\infty)^{1/2} \cdot \hat{\mathbf{M}}(s) \neq \hat{\mathbf{M}}(s) \cdot (\hat{\mathbf{L}}_\infty \hat{\mathbf{C}}_\infty)^{1/2}$. To solve this problem, the matrix $(\hat{\mathbf{L}}_\infty \hat{\mathbf{C}}_\infty)^{1/2} \cdot l$ is expressed as

$$(\hat{\mathbf{L}}_\infty \hat{\mathbf{C}}_\infty)^{1/2} \cdot l = \lambda_{\min} \cdot l\mathbf{E}_n + \hat{\mathbf{M}}_{EX} \cdot l \tag{2-22}$$

where $\lambda_{\min}$ is the minimum eigenvalue of $(\hat{\mathbf{L}}_\infty \hat{\mathbf{C}}_\infty)^{1/2}$ and $\mathbf{E_n}$ is the identity matrix. Then $\hat{\mathbf{H}}(s)$ can be written as

$$\hat{\mathbf{H}}(s) = e^{-\hat{\mathbf{\Gamma}}(s)l} = e^{-s\lambda_{\min} \cdot l\mathbf{E}_n} \hat{\mathbf{Q}}(s) \tag{2-23}$$

where $\hat{\mathbf{Q}}(s) = e^{-s\hat{\mathbf{M}}_{EX} \cdot l + \hat{\mathbf{M}}(s) \cdot l}$. Substituting (2-23) into equations in (2-18) yields

$$\hat{\mathbf{V}}(0,s) - \hat{\mathbf{Z}}_C(s)\hat{\mathbf{I}}(0,s) = e^{-s\lambda_{\min} \cdot l\mathbf{E}_n}\hat{\mathbf{Q}}(s)[\hat{\mathbf{V}}(l,s) - \hat{\mathbf{Z}}_C(s)\hat{\mathbf{I}}(l,s)] \tag{2-24a}$$

$$\hat{\mathbf{V}}(l,s) + \hat{\mathbf{Z}}_C(s)\hat{\mathbf{I}}(l,s) = e^{-s\lambda_{\min} \cdot l\mathbf{E}_n}\hat{\mathbf{Q}}(s)[\hat{\mathbf{V}}(0,s) + \hat{\mathbf{Z}}_C(s)\hat{\mathbf{I}}(0,s)] \tag{2-24b}$$

In order to generate a macromodel, (2-18) is converted into time domain

$$\hat{\mathbf{V}}(0,t) - \hat{\mathbf{z}}_C(t) * \hat{\mathbf{I}}(0,t) = \mathbf{F}_1(l, t - \tau_{\min}) \tag{2-25a}$$

$$\hat{\mathbf{V}}(l,t) + \hat{\mathbf{z}}_C(t) * \hat{\mathbf{I}}(l,t) = \mathbf{F}_2(0, t - \tau_{\min}) \tag{2-25b}$$

where $\tau_{\min} = \lambda_{\min} \cdot l$ is the time delay, $\mathbf{F_1}$ and $\mathbf{F}_2$ are voltage controlled voltage sources whose values are given by

$$\mathbf{F}_1(l,t) = \hat{\mathbf{q}}(t) * [\hat{\mathbf{V}}(l,t) - \hat{\mathbf{z}}_C(t) * \hat{\mathbf{I}}(l,t)] \tag{2-26a}$$

$$\mathbf{F}_2(0,t) = \hat{\mathbf{q}}(t) * [\hat{\mathbf{V}}(0,t) + \hat{\mathbf{z}}_C(t) * \hat{\mathbf{I}}(0,t)] \tag{2-26b}$$

with inverse Laplace transformations

$$\hat{\mathbf{V}}(s) \Leftrightarrow \hat{\mathbf{V}}(t) \quad \hat{\mathbf{I}}(s) \Leftrightarrow \hat{\mathbf{I}}(t) \quad \hat{\mathbf{Z}}_C(s) \Leftrightarrow \hat{\mathbf{z}}_C(t) \quad \hat{\mathbf{Q}}(s) \Leftrightarrow \hat{\mathbf{q}}(t) \tag{2-27}$$

The MoC macromodel for (2+1)-conductor TLs described by (2-16)-(2-27) can be equivalent to a circuit model as shown in Figure 2.21 (the reference is not included). All DC voltage sources in the figure have the role of picking up the wire currents at the ports. For this reason, their impressed voltage is zero. Figure 2.21(a) completes the tansformation of the mode voltages and currents in (2-16) as
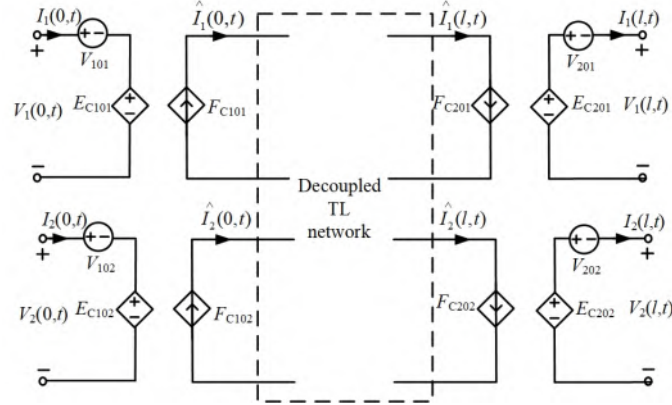
(a) The equivalent circuit of the transformation of mode voltages and currents
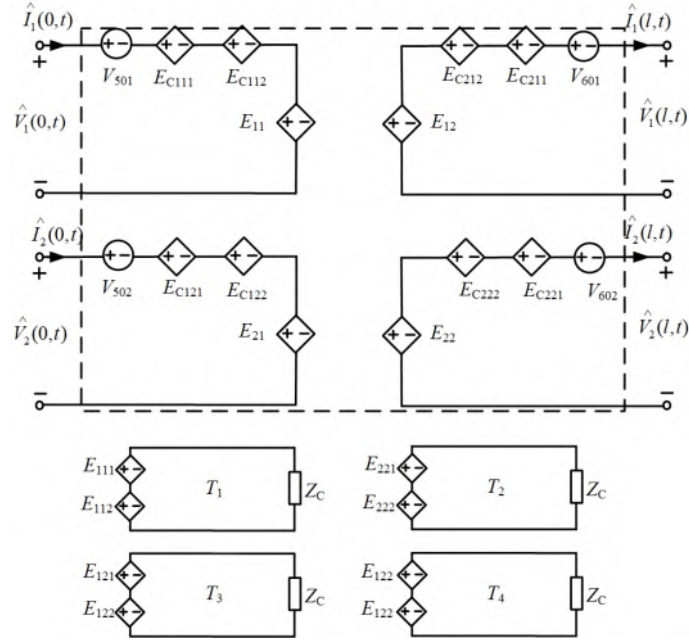
(b) The equivalent circuit of the decoupled TL model

Figure 2.21 The realization of MoC macromodel for a (2+1)-conductor TLs

$$
\begin{bmatrix} V_1(t) \\ V_2(t) \end{bmatrix} = \begin{bmatrix} T_{V11} & T_{V12} \\ T_{V21} & T_{V22} \end{bmatrix} \begin{bmatrix} \hat{V}_1(t) \\ \hat{V}_2(t) \end{bmatrix} = \begin{bmatrix} E_{C1,201} \\ E_{C1,202} \end{bmatrix} \tag{2-28a}
$$

$$
\begin{bmatrix} \hat{I}_1(t) \\ \hat{I}_2(t) \end{bmatrix} = \begin{bmatrix} T_{I11} & T_{I12} \\ T_{I21} & T_{I22} \end{bmatrix}^{-1} \begin{bmatrix} I_1(t) \\ I_2(t) \end{bmatrix} = \begin{bmatrix} F_{C1,201} \\ F_{C1,202} \end{bmatrix} \tag{2-28b}
$$

Figure 2.21(b) represents the implementation of the decoupled TL model described by (2-25)-(2-27). The controlled voltage sources $\mathbf{E_{C1}}$ and $\mathbf{E_{C2}}$ translate the convolution terms on the left hand side of (2-25), i.e.

$$\mathbf{E_{C1}} = \overset{\wedge}{\mathbf{z}}_{\mathbf{C}}(t) * \overset{\wedge}{\mathbf{I}}(0,t) = \begin{bmatrix} E_{C111}(t) + E_{C112}(t) \\ E_{C121}(t) + E_{C122}(t) \end{bmatrix} \tag{2-29a}$$

$$\mathbf{E_{C2}} = \overset{\wedge}{\mathbf{z}}_{\mathbf{C}}(t) * \overset{\wedge}{\mathbf{I}}(l,t) = \begin{bmatrix} E_{C211}(t) + E_{C212}(t) \\ E_{C221}(t) + E_{C222}(t) \end{bmatrix} \tag{2-29b}$$

The controlled voltage sources $\mathbf{E_1}$ and $\mathbf{E_2}$ correspond to the terms on the right hand side (2-25), i.e.

$$\mathbf{E_1} = \mathbf{F}_1(l, t - \tau_{\min}) = \begin{bmatrix} E_{11}(t) \\ E_{12}(t) \end{bmatrix} \tag{2-30a}$$

$$\mathbf{E_2} = \mathbf{F}_2(0, t - \tau_{\min}) = \begin{bmatrix} E_{21}(t) \\ E_{22}(t) \end{bmatrix} \tag{2-30b}$$

in which the time delay $\tau_{\min}$ is realized by ideal delay lines in SPICE and controlled sources. Finally, the controlled voltage sources of ideal delay correspond to terms on the right hand side of (2-26), i.e.

$$\mathbf{F}_1(l,t) = \overset{\wedge}{\mathbf{q}}(t) * [\overset{\wedge}{\mathbf{V}}(l,t) - \overset{\wedge}{\mathbf{z}}_{\mathbf{C}}(t) * \overset{\wedge}{\mathbf{I}}(l,t)] = \begin{bmatrix} E_{111}(t) + E_{112}(t) \\ E_{121}(t) + E_{122}(t) \end{bmatrix} \tag{2-31a}$$

$$\mathbf{F}_2(0,t) = \overset{\wedge}{\mathbf{q}}(t) * [\overset{\wedge}{\mathbf{V}}(0,t) + \overset{\wedge}{\mathbf{z}}_{\mathbf{C}}(t) * \overset{\wedge}{\mathbf{I}}(0,t)] = \begin{bmatrix} E_{211}(t) + E_{212}(t) \\ E_{221}(t) + E_{222}(t) \end{bmatrix} \tag{2-31b}$$

Except for $\mathbf{E_1}$ and $\mathbf{E_2}$, all other controlled voltage sources in Figure 2.21(b) involves the time-domain convolution calculation, which can be modeled straightforwardly by LAPLACE or FREQ parts in ABM.

It should be noted that, in order to extract the propagation delay, the partial decoupling must be performed firstly, though not all parts of the delay can be extracted. However, on the one hand, partial decoupling may not completely simplify and reduce the model complexity of decoupled TLs; on the other hand, the modeling of propagation operator $\mathbf{H}(s)$ is not a significant challenge now owing to frequency-domain ABM devices. Hence, a novel MoC model without delay extraction is constructed here, in which $\mathbf{Z_C}(s)$ and $\mathbf{H}(s)$ are modeled, directly using frequency-domain devices in ABM library. There is no need to implement the procedures of delay extraction and rational approximation during the modeling process, nor is partial decoupling of the generalized MoC algorithm necessary. Also taking a (2+1)-conductor TL as an example here, the un-decoupled equivalent circuit of the MoC macromodel described by (2-7) is shown in Figure 2.22 (the reference is not included).

The DC voltage sources have the same role as them in Figure 2.21. Similarly, all controlled voltage sources translate the convolution calculations in (2-7), specifically,
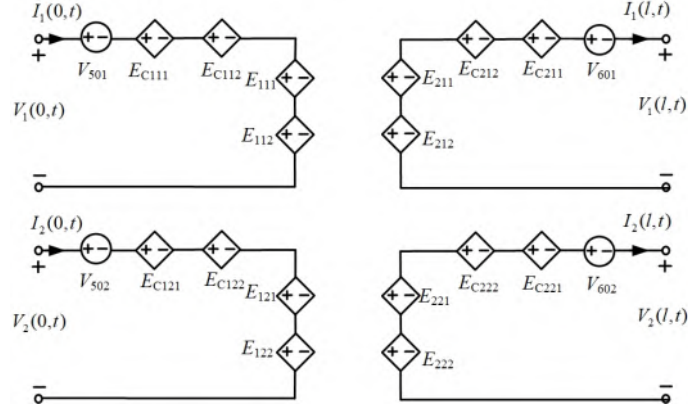
Figure 2.22 The un-decoupled realization of MoC macromodel for a (2+1)-conductor TL

$$\mathbf{E_{C1}} = \mathbf{z_C}(t) * \mathbf{I}(0,t) = \begin{bmatrix} E_{C111}(t) + E_{C112}(t) \\ E_{C121}(t) + E_{C122}(t) \end{bmatrix} \tag{2-32a}$$

$$\mathbf{E_{C2}} = \mathbf{z_C}(t) * \mathbf{I}(l,t) = \begin{bmatrix} E_{C211}(t) + E_{C212}(t) \\ E_{C221}(t) + E_{C222}(t) \end{bmatrix} \tag{2-32b}$$

and

$$\mathbf{h}(t) * [\mathbf{V}(l,t) - \mathbf{z_C}(t) * \mathbf{I}(l,t)] = \begin{bmatrix} E_{111}(t) + E_{112}(t) \\ E_{121}(t) + E_{122}(t) \end{bmatrix} \tag{2-33a}$$

$$\mathbf{h}(t) * [\mathbf{V}(0,t) + \mathbf{z_C}(t) * \mathbf{I}(0,t)] = \begin{bmatrix} E_{211}(t) + E_{212}(t) \\ E_{221}(t) + E_{222}(t) \end{bmatrix} \tag{2-33b}$$

2.4.2 Accuracy and efficiency validation

This section studies a numerical example to demonstrate the accuracy and efficiency of the proposed ABM-based MoC macromodels. The transient responses of coupled TLs are obtained using PSpice circuit software and the simulation times are also compared on a PC equipped with an INTEL i7 3.6-GHz CPU.

We report here transient results of two-coupled TLs with 10-m length above lossy ground in Figure 2.23. The input signal is a double-exponential pulse with the time resolution $\Delta t = 0.5$ ns and the transient analysis time $TSTOP$ being 1 μs. The radius of TLs is 1 mm, and the height is 1 m. The distance between two lines is 0.2 m. This example is solved by various models, and we compare the results in terms of accuracy and execution times.

Figure 2.24 shows the transient responses of two MoC macromodels proposed in 2.4.1, conventional MoC model and the DEPACT macromodel[68, 117] at the terminals of two TLs. The equivalent circuit of the DEPACT macromodel is composed of subnetworks. For ensuring the accuracy, the DEPACT macromodel is divided into five segments. So the relative error of
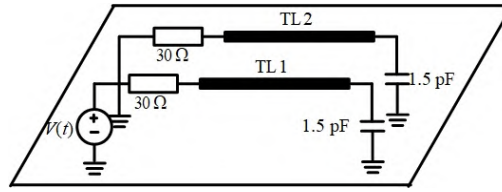
Figure 2.23 A circuit containing two-conductor TLs with frequency-dependent p.u.l parameters

DEPACT model is limited to be less than 0.5 %. Table 2.6 gives a CPU expense comparison of proposed macromodels, including with and without delay extraction, conventional MoC model and DEPACT model.
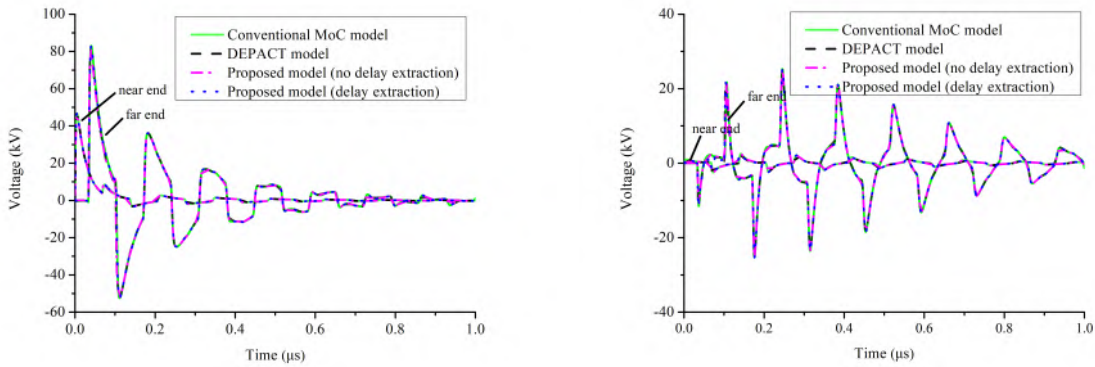
(a) Transient responses on the active line

(b) Transient responses on the quiet line

Figure 2.24 Comparison of transient responses of different models for two-conductor TLs in Figure 2.23

Table 2.6 Comparison of simulation times of several models

Models	Conventional MoC model	DEPACT model	Proposed model with delay extraction	Proposed model without delay extraction
Simulation times (s)	33.59	164.02	25.44	10.03

Figure 2.24 shows that for two-coupled TLs, there are excellent agreements among several models for both responses at the near and far ends. It should be pointed out from Table 2.6 that the proposed macromodel is markedly faster than the conventional MoC macromodel and DEPACT macromodel, and in particular, the model without delay extraction performs best in consideration of not only simulation time but modeling process. The excellent performance of the proposed algorithm can be readily explained by the fact that the current marching-on in time SPICE solution does not suffer from the computational consumption of rational approximations and delay extraction used by MoC approach and line sectioning algorithm required by DEPACT. Besides, the proposed model without delay extraction is also adopted to calculate

a case of 20-m coupled TLs, which consumes about 7.98 s. So the efficiency of the proposed algorithm has less to do with the line length, which ensures that the efficiency would not be limited by the line length. Finally, the CPU comparison in Table 2.6 is fair, since all algorithms have been implemented as callable macromodels; hence, only the time needed to simulate the responses of macromodel by the circuit solver is compared.

2.5 Passivity consideration of the proposed macromodel

Since TLs are passive elements, preservation of the TL passivity is one of key issues of modeling TLs. A passive macromodel means that a network cannot generate more energy than it absorbs[118, 119].

A linear n-port network with an admittance matrix $\mathbf{Y}(s)$ is taken to be passive if, and only if[89, 119]

1. $\mathbf{Y}(s^*) = \mathbf{Y}^*(s)$ for all $s = \sigma + j\omega$, where "*" is the complex conjugate operator;
2. $\mathbf{Y}(s)$ is analytic for all complex values of $s = \sigma + j\omega$ satisfying $\mathrm{Re}(s) = \sigma > 0$;
3. $\mathbf{Y}(s)$ is a positive real (PR) matrix. That is, the product $z^{*T}(\mathbf{Y}^T(s^*) + \mathbf{Y}(s))z \geq 0$ for all complex values of s satisfying $\mathrm{Re}(s) = \sigma > 0$ and for arbitrary vector z.

Therefore, a sufficient condition is specified to guarantee the macromodel without delay extraction for MTLs in section 2.4 is passive.

Theorem: The passivity of the proposed macromodel is guaranteed if parameters $\mathbf{Z}(s) = \mathbf{R}(s) + s\mathbf{L}(s)$ and $\mathbf{Y}(s) = \mathbf{G}(s) + s\mathbf{C}(s)$ are both PR.

The proof of the above condition to preserve passivity of the macromodel given by (2-7) is provided in Appendix A. The above sufficient condition is that the p.u.l parameters $\mathbf{Z}(s)$ and $\mathbf{Y}(s)$ are both PR matrices, which is similar to the passivity condition of the MRA and DEPACT macromodel[68, 120]. It should be noted that the functions of $\mathbf{Z}(s)$ and $\mathbf{Y}(s)$ are always positive real for MTLs, however, these parameters are usually obtained by measurements, empirical formulae or electromagnetic simulation. Hence, in the light of above statement, it is required to be very careful to check and correct passive violations during the entire modeling process.

2.6 Concluding remarks

This chapter starts off with generalized MoC macromodeling approach. Based on the analog behavior modeling, frequency-dependent characteristics (convolution calculation) and non-linear components can be modeled by instantaneous devices and non-instantaneous frequency-domain devices in ABM during transient analysis. Some criteria and constraints on the simulation of frequency-domain parts are also proposed and analyzed to insure the accuracy and efficiency of the models.

Then, an accurate and efficient time-domain MoC-based macromodeling algorithm is pro-

posed to calculate transient responses of MTLs, in which the characteristic impedances (or admittances) and propagation operators of MTLs are modeled using frequency-domain devices (LAPLACE or FREQ) directly. There is no need to implement the procedures of delay extraction and rational approximation during the modeling process, nor is partial decoupling used in generalized MoC and DEPACT macromodels necessary. Furthermore, the passivity of the proposed macromodel is intrinsically guaranteed if the p.u.l. parameters are physically consistent and positive real.

Compared with the existing macromdeling algorithms, the proposed algorithm can not only yield compact and accurate macromodels, but largely simplify and speed up the modeling and simulation processes, especially for long MTLs with large delays. Hence, with the knowledge of the empirical function or tabulated data of parameters, the proposed macromodel can be easily formulated and embedded in the SPICE simulator in an accurate and efficient way for the transient analysis of lossy MTLs terminated with linear or nonlinear loads. The main research contributions in this chapter can be extended to study cases of field coupling to TLs considering effects of lossy ground, which makes a good theoretical foundation for the following chapters.

3   A time-domain macromodel for MTLs and TL networks above lossy ground to field coupling

An accurate and efficient time-domain macromodel based on the ABM and MoC is proposed in the second chapter. Though the efficiency of this novel macromodel would not be limited by the line length, which is a great advantage to model wide-area long-distance MTLs, the excitation of external field is not yet included. Besides, when a lossy earth serves as a return conductor, the Telegrapher's equations must be modified to include the lossy ground effects, which results in additional ground impedance and admittance elements in p.u.l parameters. Hence, accurate and appropriate formulations of earth return correction terms are also required.

In this chapter, in order to calculate current and voltage responses of overhead long-distance MTLs and wide-area TL networks to incident field coupling, the application of the macromodel is firstly extended to incorporate incident field excitation and lossy ground's effects. The lumped excitation sources related to incident field are added external or internal to the TL model, depending on different derivation methods. For TL networks, the macromodel can easily be realized by connecting two-port sub-models of TLs together. Particularly, a simplified model of the network based on Thevenin transformation is proposed to treat discrete branches of network as a one-port Thevenin circuit. Various examples will be studied in this chapter to verify the proposed algorithm. One thing should also be declared is that part of the work described in this chapter has been previously publised in [121] and [122].

The specific content is arranged as: in section 3.1, we give an elaborate derivation of the time-domain macromodel for overhead MTLs above lossy ground to field coupling, and the discussion of formulations of p.u.l line parameters. Section 3.2 provides modeling approach of field coupling to overhead TL networks, and a simplified model based on Thevenin transformation is also presented. Then, aimed at demonstrating the proposed models and carrying out numerical studies, five examples are presented and analyzed in section 3.3. Based on above work, time-domain macromodels for field coupling to MTLs and TL networks above lossy ground are proposed, and the validity and efficiency of them have also been verified. Section 3.4 summaries the research work of this chapter. The research work of this chapter can be extended to cases of buried TLs in the next chapter.

3.1   Derivation of the macromodel for field coupling to overhead MTLs

In this section, the modeling of incident field coupling to overhead MTLs above lossy ground is explicitly described using the macromodel proposed before.

3.1.1 Configuration and formulation of overhead MTLs to field coupling
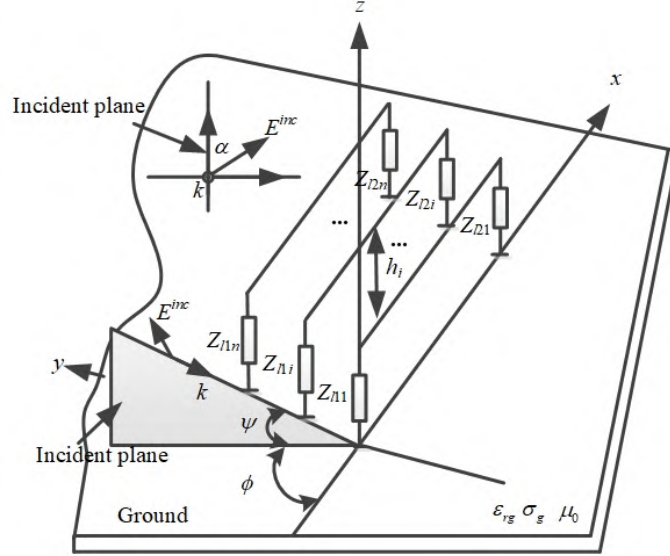
Figure 3.1 The configuration of incident field coupling to MTLs above lossy ground

In this section, to formulate the plane wave coupling to overhead MTLs above lossy ground, we consider the geometric arrangement consists of n ($n \geq 1$) horizontal and parallel conductors, as shown in Figure 3.1. The i-th conductor is located at a height of h_i. l is the length of conductors, and d_{ij} is the distance between the i-th and j-th conductor. Impedances $\mathbf{Z}_{l1}$ and $\mathbf{Z}_{l2}$ are loads at the terminal ends of conductors. The ground lossy is characterized by relative permittivity ε_{rg}, conductivity σ_g, and free-space permeability μ_0. Hence, if the ground acts as the loop conductor of all overhead MTLs, the earth return correction terms on p.u.l parameters must be considered, and the infinite depth below the ground is selected as the zero potential reference.

As introduced before, in order to incorporate the external field into analysis of waveform propagation on TLs, there are several models of Telegraphe's equations available, one of which the Agrawal field-to-wire coupling model is simple and accurate enough[47]. For overhead MTLs in Figure 3.1, the Agrawal model's matrix equations in Laplace domain considering frequency-dependent parameters are

$$\frac{d}{dx}\begin{bmatrix} \mathbf{V}^s(x,s) \\ \mathbf{I}(x,s) \end{bmatrix} + \begin{bmatrix} \mathbf{0} & \mathbf{Z}(s) \\ \mathbf{Y}(s) & \mathbf{0} \end{bmatrix} \begin{bmatrix} \mathbf{V}^s(x,s) \\ \mathbf{I}(x,s) \end{bmatrix} = \begin{bmatrix} \mathbf{E}_x^{ex}(s,x) \\ \mathbf{0} \end{bmatrix} \tag{3-1}$$

in which vectors $\mathbf{V}^s = [V_1^s, \ldots, V_n^s]^T$ and $\mathbf{I} = [I_1, \ldots, I_n]^T$ are scattering voltage vector and total current vector along conductors, T denotes the transpose of the associated matrix or vector. The distributed voltage source $\mathbf{E}_x^{ex}(s,x)$ equals to the x-axial component of electric field at conductors' height. $\mathbf{Z}(s)$ and $\mathbf{Y}(s)$ are p.u.l impedance and admittance matrices. In order to

illustrate the relationship between the scattering voltage and total voltage, the voltage due to the vertical component of the electric field should be considered, so the boundary condition of equation (3-1) can be given as

$$\mathbf{V}^s(0) = -\mathbf{Z}_{l1}\mathbf{I}(0) + \mathbf{E}_{z1} \tag{3-2a}$$

$$\mathbf{V}^s(l) = \mathbf{Z}_{l2}\mathbf{I}(l) + \mathbf{E}_{z2} \tag{3-2b}$$

$\mathbf{E}_{z1}$ and $\mathbf{E}_{z2}$ are related with the vertical component of electric field $E_z^{ex}(x, y, z)$:

$$\mathbf{E}_{z1} = \begin{bmatrix} \int_{-\infty}^{h_1} E_z^{ex}(0, y_1, z)dz \\ \vdots \\ \int_{-\infty}^{h_j} E_z^{ex}(0, y_j, z)dz \\ \vdots \\ \int_{-\infty}^{h_n} E_z^{ex}(0, y_n, z)dz \end{bmatrix} ; \quad \mathbf{E}_{z1} = \begin{bmatrix} \int_{-\infty}^{h_1} E_z^{ex}(l, y_1, z)dz \\ \vdots \\ \int_{-\infty}^{h_j} E_z^{ex}(l, y_j, z)dz \\ \vdots \\ \int_{-\infty}^{h_n} E_z^{ex}(l, y_n, z)dz \end{bmatrix} \tag{3-3}$$

The presence of limited ground conductivity introduces several effects into the above model, which is mainly reflected in two aspects. In the first place, the ground impedance can be viewed as a correction factor to the p.u.l longitudinal impedance if the gournd is not perfect, that is, the p.u.l impedance $\mathbf{Z}(s)$ is composed of p.u.l inductance $\mathbf{L}$, internal resistance of the conductor $\mathbf{Z}_w$ and ground impedance $\mathbf{Z}_g(s)$; and correspondingly, the ground admittance $\mathbf{Y}_g(s)$ combined with conductance $\mathbf{C}$ is also included in the p.u.l shunt admittance matrix $\mathbf{Y}(s)$:

$$\mathbf{Z}(s) = \mathbf{Z}_w(s) + \mathbf{Z}_g(s) + s\mathbf{L} \tag{3-4a}$$

$$\mathbf{Y}(s) = ((s\mathbf{C})^{-1} + \mathbf{Y}_g^{-1}(s))^{-1} \tag{3-4b}$$

These parameters are usually defined in frequency domain by means of electromagnetic quasi-TEM modeling, whose expressions will be discussed and described in the next section. Note that for typical overhead lines ($\sigma_g = 10^{-3} - 10^{-2}$ S/m, $\varepsilon_{rg} = 1 - 10$) the ground admittance $\mathbf{Y}_g(s)$ can be omitted from (3-4b) for simplification in overhead cases[39, 123]. Also, we neglect the wire internal impedance $\mathbf{Z}_w(s)$ from (3-4a) with reasonable approximation[124].

For another, the influence of ground conductivity is also taken into consideration in the reflection coefficient used to calculate the excitation electromagnetic field environment of MTLs. The excitation field is the superposition of incident waves and reflected waves from the earth surface. For a uniform plane wave, the incident field E^{inc} and reflected electric field E^{ref} are expressed analytically as[43, 125]

$$E^{inc} = E_0(\omega)[(\cos\alpha\sin\psi\cos\phi + \sin\alpha\sin\phi)x+$$
$$(-\cos\alpha\sin\psi\sin\phi + \sin\alpha\cos\phi)y + \cos\alpha\cos\psi z]e^{-jkx\cos\psi\cos\phi}e^{jky\cos\psi\sin\phi}e^{jkz\sin\psi}$$

$$(3\text{-}5)$$

$$E^{ref} = E_0(\omega)[(-\cos\alpha\sin\psi\cos\phi R_v + \sin\alpha\sin\phi R_h)x+$$
$$(\cos\alpha\sin\psi\sin\phi R_v + \sin\alpha\cos\phi R_h)y + \cos\alpha\cos\psi R_v z]e^{-jkx\cos\psi\cos\phi}e^{jky\cos\psi\sin\phi}e^{-jkz\sin\psi}$$

$$(3\text{-}6)$$

in which $E_0(\omega)$ is the Fourier transform of the time-domain expression of electric field; R_v and R_h are vertical and horizontal Fresnel reflection coefficient, respectively; $k = \omega\sqrt{\mu_0\varepsilon_0}$ is the wavenumber in free space; The angles α, ψ and ϕ are polarization angle, elevation and azimuthal angle of incident field, as defined in Figure 3.1. The Fresnel reflection coefficients can be written as

$$R_v = \frac{(1 + \frac{\sigma_g}{j\omega\varepsilon_0})\sin\psi - \sqrt{1 + \frac{\sigma_g}{j\omega\varepsilon_0} - \cos^2\psi}}{(1 + \frac{\sigma_g}{j\omega\varepsilon_0})\sin\psi + \sqrt{1 + \frac{\sigma_g}{j\omega\varepsilon_0} - \cos^2\psi}} \tag{3-7}$$

$$R_h = \frac{\sin\psi - \sqrt{1 + \frac{\sigma_g}{j\omega\varepsilon_0} - \cos^2\psi}}{\sin\psi + \sqrt{1 + \frac{\sigma_g}{j\omega\varepsilon_0} - \cos^2\psi}} \tag{3-8}$$

In accordance with above expressions, the x-axial component of excitation field in (3-1) and z-axial component of excitation field in (3-3) are

$$E_x^{ex}(x,y,z) = E_x^{inc} + E_x^{ref}$$
$$= E_0[\cos\alpha\sin\psi\cos\phi(e^{jkz\sin\psi} - R_v e^{-jkz\sin\psi})$$
$$+ \sin\alpha\sin\phi(e^{jkz\sin\psi} + R_h e^{-jkz\sin\psi})]e^{jky\cos\psi\sin\phi}e^{-jkx\cos\psi\cos\phi} \tag{3-9}$$

$$E_z^{ex}(x,y,z) = E_z^{inc} + E_z^{ref}$$
$$= E_0\cos\alpha\cos\psi(e^{jkz\sin\psi} - R_v e^{-jkz\sin\psi})e^{-jkx\cos\psi\cos\phi}e^{jky\cos\psi\sin\phi} \tag{3-10}$$

3.1.2   The formulations of p.u.l parameters for overhead MTLs

To elaborate the expressions of p.u.l paramters, we consider n-conductor overhead TLs, whose cross-section configuration is shown in Figure 3.2. The i-th conductor has the radius a_i and height h_i from the ground plane. Distance d_{ij} and Δ_{ij} are indicated in Figure 3.2.

1) Inductance and capacitance expressions

Firstly, **L** and **C** are inductance and capacitance matrices, whose expressions are given respectively as:
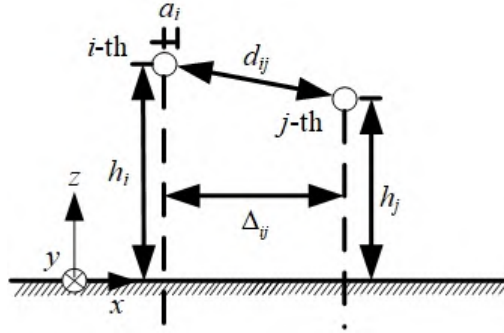
Figure 3.2 The cross-section of the MTLs above lossy ground

$$\mathbf{L} = \frac{\mu_0}{2\pi}\mathbf{A}; \quad \mathbf{C} = \varepsilon_0 2\pi \mathbf{A}^{-1} \tag{3-11}$$

Assuming that $a_i \ll (h_i, d_{ij}, \Delta_{ij})$, the diagonal and non-diagonal elements of matrix $\mathbf{A}$ are:

$$A_{ii} = \ln \frac{2h_i}{a_i}; \quad A_{ij} = \frac{\sqrt{(h_i + h_j)^2 + \Delta_{ij}^2}}{d_{ij}} \tag{3-12}$$

2) Ground impedance and admittance expressions

The first explicit expression proposed for the ground impedance is due to Carson in 1926[126]. This expression holds over low-frequency values and/or good conductivies of the ground. Later, several efforts have been made to propose more appropriate ground impedance expressions at higher frequencies, as well as formulations derived from rigorous full-wave approaches[127–132].

Among these formulations, the one proposed by Sunde has been proved to be particularly accurate, and furthermore, is approximated in a very simple way by himself in case of a single-conductor configuration[43, 128, 133]. So the logarithmic approximation of self ground impedance can be written as:

$$Z_{gii}^{Sunde-\log} = \frac{j\omega\mu_0}{2\pi} \ln \left[\frac{1 + \gamma_g h_i}{\gamma_g h_i} \right] \tag{3-13}$$

where $\gamma_g = \sqrt{j\omega\mu_0(\sigma_g + j\omega\varepsilon_{rg}\varepsilon_0)}$ is the propagation constant in the ground. The only difference between Carson's and Sunde's expressions is that the full propagation constant in the ground was used by Sunde, which means that at higher frequencies the displacement currents in the soil are not be ignored. Hence, in studies about field-to-line coupling problems of overhead power lines in a wide frequency range, the Sunde's logarithmic approximation in (3-13) is widely used. Besides, a considerable contribution of Vance is to relate the ground admittance and ground impedance through propagation constant as

$$Y_g = \gamma_g^2 Z_g^{-1} \tag{3-14}$$

Then, for the mutual ground impedance, the logarithmic impedance expression (3-13) is extended by Rachidi et al.[134] as given in (3-15), and it is claimed that (3-15) is a very good approximation for the mutual ground impedance proposed by Sunde.

$$Z_{gij}^{Sunde-\log} = \frac{j\omega\mu_0}{2\pi} \ln \left[\frac{\left[1 + \left(\frac{\gamma_g(h_i+h_j)}{2}\right)\right]^2 + \left(\frac{\gamma_g\Delta_{ij}}{2}\right)^2}{\left(\frac{\gamma_g(h_i+h_j)}{2}\right)^2 + \left(\frac{\gamma_g\Delta_{ij}}{2}\right)^2} \right] \tag{3-15}$$

Except for widely used logarithmic approximation expressions of self and mutual ground impedance, D'Amore et al. proposed a new formulation of the lossy ground in wide-frequency range and/or under poor ground conductivities[124, 132]. This formulation is developed on the basis of a rigorous curl Maxwell field equation, which is derived by Wait from full-wave analysis[124, 132]. In this method, the lossy soil is not regarded as a lossy conductor, but rather as a generic homogeneous medium. That is, no other approximation is considered so long as the quasi-TEM approximation is valid, thus extending the p.u.l expressions over a frequency range $\omega_c = \sigma_g/(\varepsilon_0\varepsilon_{rg})$. It is the critical frequency at which the displacement currents become equal to the conduction currents. The formulation proposed by D'Amore are also briefly recalled here.

The ground impedance matrix $\mathbf{Z}_g$ can be evaluated by

$$\mathbf{Z}_g = \frac{j\omega\mu_0}{2\pi} \left(\mathbf{F}_1 - \mathbf{F}_3 \right) \tag{3-16}$$

in which the generic elements of matrices $\mathbf{F}_1$ and $\mathbf{F}_3$ are respectively:

$$F_{1ij} = \frac{1}{2} \ln \left\{ 1 + \frac{\xi_1}{\sqrt{(h_i+h_j)^2 + \Delta_{ij}^2}} \right\} \tag{3-17a}$$

$$F_{3ij} = \xi_2 \ln \left\{ 1 + \frac{\xi_3}{\sqrt{(h_i)^2 + \Delta_{ij}^2}} \right\} \tag{3-17b}$$

$$\xi_1 = \frac{2}{\sqrt{k_0^2 - k_g^2}}; \quad \xi_2 = \frac{k_0^2}{\sqrt{k_0^2 + k_g^2}}; \quad \xi_3 = \frac{k_0^2 + k_g^2}{k_0^2\sqrt{k_0^2 - k_g^2}} \tag{3-18}$$

$$k_g = k\sqrt{\varepsilon_{rg} - j\frac{\sigma_g}{\omega\varepsilon_0}} \tag{3-19}$$

The ground admittance has the expression:

$$\mathbf{Y}_g = j\omega\varepsilon_0(\mathbf{F}_2 - \mathbf{F}_3)^{-1} \tag{3-20}$$

The generic elements of matrices $\mathbf{F}_2$ are:

$$F_{2ij} = \xi_2 \ln\left\{1 + \frac{\xi_3}{\sqrt{(h_i + h_j)^2 + \Delta_{ij}^2}}\right\} \tag{3-21}$$

3) Discussion and comparison of Sunde's and D'Amore's ground impedance and admittance formulations

The logarithmic expressions (3-13)-(3-15) as well as D'Amore's expressions (3-16)-(3-21) could lead to different formulations of p.u.l impedance and admittance matrices in (3-4). As a consequence, different prediction of transient responses propagating along TLs may be achieved. Hence, an essential issue concerns the comparison between these two formulations of ground impedance and admittance. Figure 3.3 presents a comparison of different ground impedance expressions for a wire with a=1 cm, located at a height of h=10 m above the ground characterized by σ_g=5 mS/m and ε_{rg}=5.

(a) Real part (b) Imaginary part
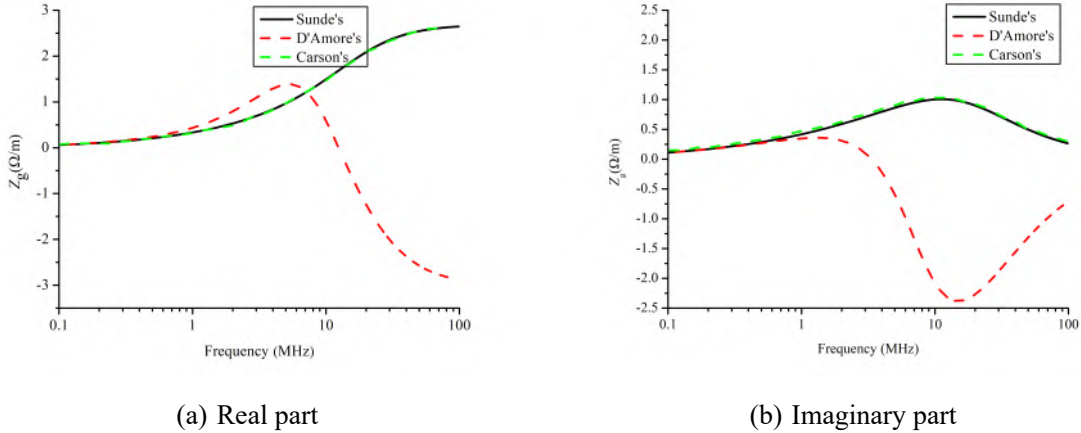
Figure 3.3 Frequency spectra of the real and imagnary parts of the ground impedance

From Figure 3.3, the waveforms of Carson's and Sunde's expressions are nearly coincident with each other, while the D'Amore approximation goes to big difference in the high frequency range (approximately above 1 MHz). Furthermore, both real and imaginary parts of D'Amore's ground impedance become negative in the high-frequency range.

Next, we calculate the ground admittance using (3-14) and (3-20), respectively, taking the same example as above, and the corresponding overall shunt admittance parameters. The comparison is shown in Figure 3.4, from which it can be seen that though the Vance's expression in (3-14) and D'Amore's expression in (3-20) are much different for high frequencies, the ground impedance can be simply neglected for conductors above ground since its negligible

contribution to the overall shunt admittance.

(a) Ground admittance　　　　　　　　　　(b) Shunt admittance
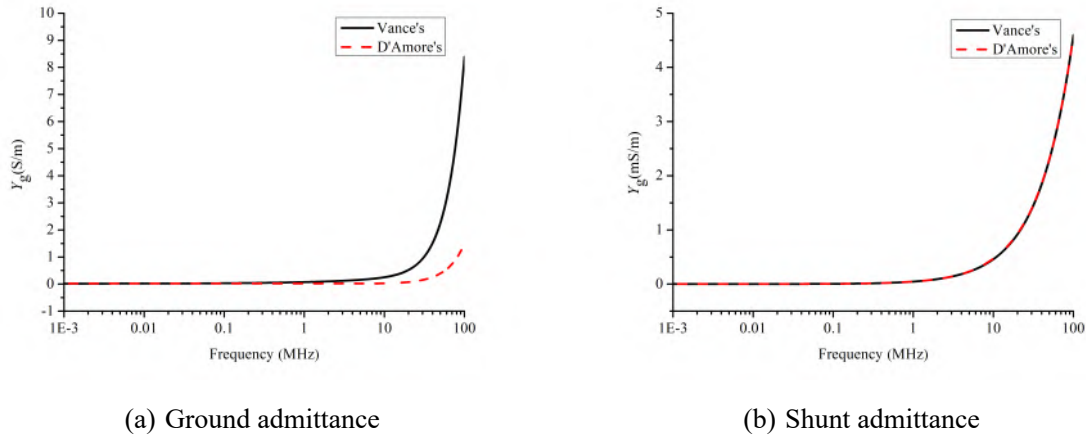
Figure 3.4　Frequency spectra of the ground admittances and shunt admittances

The impact of the above different ground impedance expressions on transient responses of overhead MTLs above lossy ground will be compared and discussed later in the following section.

3.1.3　Parameter simplification of bundle conductors

Bundle conductors refers to a wire arrangement form adopted by ultra-high voltage (UHV) overhead MTLs to suppress corona discharge and reduce line reactance. That is, each phase is composed of several sub-conductors with small diameters, which are spaced at a certain distance and arranged symmetrically on the vertices of a regular polygon, as shown in Figure 3.5. However, the number increase of MTLs will lead to larger memory consumption and lower computation efficiency during waveform propagation analysis.

(a) Two-splitting
conductors

(b) Three-splitting
conductors

(c) Four-splitting
conductors
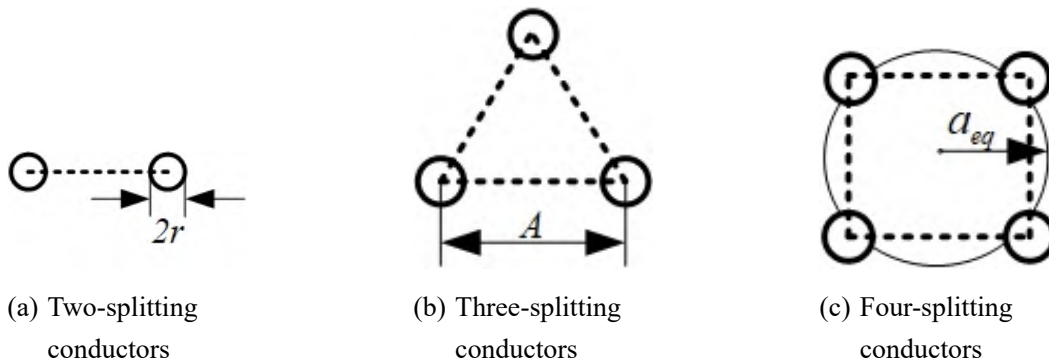
Figure 3.5　Sketch of bundled conductors

As to this problem, an equivalent method can be adopted to simplify the computation[135]. Specifically, because sub-conductors are arranged compactly compared with the distance between phases, the bundle conductors can be regarded as an equivalent conductor, observing

the electromagnetic effects on lines from a certain distance. The equivalent circuit is based on two assumptions:

1. All sub-conductors are connected together at the terminal ends of each phase, and are grounded by load impedances. Hence, we assume that the voltages of all sub-conductors are same, and equal to the voltage V_{eq} of the equivalent phase conductor (m is the number of sub-conductors);

$$V_{eq} = V_1 = ... = V_m \tag{3-22}$$

2. The current of the equivalent phase conductor is the sum of all currents flowing on sub-conductors.

$$I_{eq} = I_1 + ... + I_m \tag{3-23}$$

Hence, the equivalent conductor's scattering voltage and current can also be related by:

$$\frac{d}{dx} \begin{bmatrix} V_{eq}^s(x,s) \\ I_{eq}(x,s) \end{bmatrix} + \begin{bmatrix} 0 & Z_{eq}(s) \\ Y_{eq}(s) & 0 \end{bmatrix} \begin{bmatrix} V_{eq}^s(x,s) \\ I_{eq}(x,s) \end{bmatrix} = \begin{bmatrix} E_x^{ex}(s,x,y,z) \\ 0 \end{bmatrix} \tag{3-24}$$

in which Z_{eq} and Y_{eq} can be evaluated by formulations presented in section 3.1.2, so long as the radius a is substituted by equivalent radius a_{eq}, which can be written as

$$a_{eq} = \left(m \times r \times A^{m-1} \right)^{1/m} \tag{3-25}$$

with r being the radius of sub-conductors, and A being the distance between adjacent sub-conductors in Figure 3.5.

3.1.4 The application of the macromodel to incident field coupling

In order to derive the lumped equivalence of distributed excitation sources, the Laplace-domain solution to the field-to-wire coupling matrix equation (3-1) is firstly written as

$$\begin{bmatrix} \mathbf{V}^s(l,s) \\ \mathbf{I}(l,s) \end{bmatrix} = e^{\mathbf{B}(s)l} \begin{bmatrix} \mathbf{V}^s(0,s) \\ \mathbf{I}(0,s) \end{bmatrix} + \begin{bmatrix} \mathbf{V}_{TF}(l,s) \\ \mathbf{I}_{TF}(l,s) \end{bmatrix} \tag{3-26}$$

where

$$\mathbf{B}(s) = \begin{bmatrix} \mathbf{0} & -\mathbf{Z}(s) \\ -\mathbf{Y}(s) & \mathbf{0} \end{bmatrix} \tag{3-27}$$

Here, the $\mathbf{Z}(s)$ and $\mathbf{Y}(s)$ matrices have been defined in (3-4). The forcing function $\begin{bmatrix} \mathbf{V}_{TF}(l,s) \\ \mathbf{I}_{TF}(l,s) \end{bmatrix}$ related to the incident field can be expressed as follows

$$\begin{bmatrix} \mathbf{V}_{TF}(l,s) \\ \mathbf{I}_{TF}(l,s) \end{bmatrix} = \int_0^l e^{\mathbf{B}(s)(l-s)} \mathbf{F}(s,x) dx \tag{3-28}$$

The term $\mathbf{F}(s,x)$ represents the interaction of the incoming field with TLs as

$$\mathbf{F}(s,x) = \begin{bmatrix} \mathbf{V}_F(s,x) \\ \mathbf{I}_F(s,x) \end{bmatrix} = e^{-jk_x x \mathbf{E}_{2n}} \mathbf{F}'(s) \tag{3-29}$$

$\mathbf{E}_{2n}$ is a unity matrix with same size as $\mathbf{B}$. $k_x = k\cos\psi\cos\phi$ is the x-component of the propagation constant, and

$$\mathbf{V}_F(s,x) = \begin{bmatrix} \vdots \\ E_0[\cos\alpha\sin\psi\cos\phi(e^{jk z_i \sin\psi} - R_v e^{-jk z_i \sin\psi}) \\ + \sin\alpha\sin\phi(e^{jk z_i \sin\psi} + R_h e^{-jk z_i \sin\psi})]e^{jk y_i \cos\psi\sin\phi}e^{-jk_x x} \\ \vdots \end{bmatrix} \tag{3-30a}$$

$$\mathbf{I}_F(s,x) = \begin{bmatrix} \vdots \\ 0 \\ \vdots \end{bmatrix} \tag{3-30b}$$

Next define

$$\mathbf{A} = -\mathbf{B} - jk_x x \mathbf{E}_{2n} \tag{3-31}$$

Then, using the expression (3-28)-(3-31), the forcing function $\begin{bmatrix} \mathbf{V}_{TF}(l,s) \\ \mathbf{I}_{TF}(l,s) \end{bmatrix}$ can be obtained as

$$\begin{bmatrix} \mathbf{V}_{TF}(l,s) \\ \mathbf{I}_{TF}(l,s) \end{bmatrix} = -e^{\mathbf{B}(s)l} \mathbf{A}^{-1} \mathbf{F}'(s) + e^{-jk_x x \mathbf{E}_{2n} l} \mathbf{A}^{-1} \mathbf{F}'(s) \tag{3-32}$$

Incorporating (3-32) into (3-26) yields

$$\begin{bmatrix} \mathbf{V}^s(l,s) \\ \mathbf{I}(l,s) \end{bmatrix} = e^{\mathbf{B}(s)l} \left\{ \begin{bmatrix} \mathbf{V}^s(0,s) \\ \mathbf{I}(0,s) \end{bmatrix} + \begin{bmatrix} \mathbf{V}_{F1}(0,s) \\ \mathbf{I}_{F1}(0,s) \end{bmatrix} \right\} + \begin{bmatrix} \mathbf{V}_{F2}(l,s) \\ \mathbf{I}_{F2}(l,s) \end{bmatrix} \tag{3-33}$$

where

$$\begin{bmatrix} \mathbf{V}_{F1}(0,s) \\ \mathbf{I}_{F1}(0,s) \end{bmatrix} = -\mathbf{A}^{-1} \mathbf{F}'(s) \tag{3-34}$$

represents the equivalent voltage and current sources due to incident field at the near ends of TLs and

$$\begin{bmatrix} \mathbf{V}_{F2}(l,s) \\ \mathbf{I}_{F2}(l,s) \end{bmatrix} = e^{-jk_x x \mathbf{E}_{2n}l} \mathbf{A}^{-1} \mathbf{F}'(s) \tag{3-35}$$

represents the equivalent voltage and current sources due to incident field at the far ends of TLs.

It should be noted that the forcing sources are independent of the model of TLs, but solely depend on the parameters of TLs and incident field. So the representation of the equation (3-33) is described in Figure 3.6 (taking 2-conductor TLs as an example with the reference being ground), in which the unexcited TLs has been modeled and shown in Figure 2.22. $\mathbf{V}_{Fi}(t) = [V_{Fi1}(t), V_{Fi2}(t)]^T$ and $\mathbf{I}_{Fi}(t) = [I_{Fi1}(t), I_{Fi2}(t)]^T$ $(i = 1, 2)$ are voltage and current sources related to the incident field, $\mathbf{V}_{Fi}(t)$ and $\mathbf{I}_{Fi}(t)$ are time-domain conversions of $\mathbf{V}_{Fi}$ and $\mathbf{I}_{Fi}$ in (3-34) and (3-35). The voltage sources $\mathbf{E}_{z1}(t) = [E_{z11}(t), E_{z12}(t)]^T$ and $\mathbf{E}_{z2}(t) = [E_{z21}(t), E_{z22}(t)]^T$ transform the scattering voltages to total voltages, $\mathbf{E}_{z1}(t)$ and $\mathbf{E}_{z2}(t)$ are time-domain representation of $\mathbf{E}_{z1}$ and $\mathbf{E}_{z2}$ in (3-2). In addition, though all voltage and current sources in Figure 3.6 cannot be analytically expressed in time domain directly, they are to be determined by a numerical inverse Laplace transform.
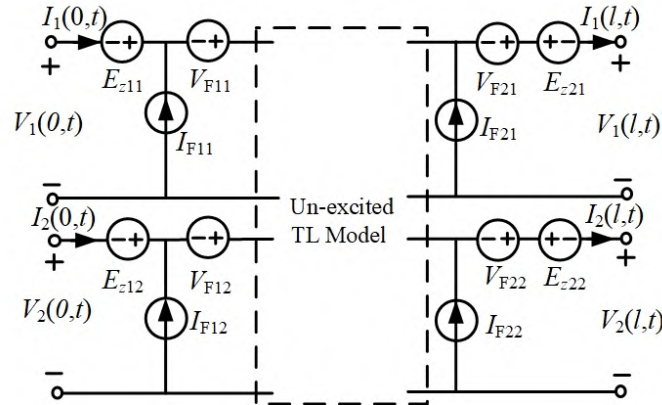
Figure 3.6 Equivalent circuit of incident field coupling to 2-conductor TLs (external excited)

The model in Figure 3.6 is referred to the external excited model in the following context, because all sources due to excited field are external to the model of MTLs. Then the equation (3-26) can be rewritten as

$$\begin{bmatrix} \mathbf{V}^s(l,s) \\ \mathbf{I}(l,s) \end{bmatrix} = \begin{bmatrix} \mathbf{\Phi}_{11} & \mathbf{\Phi}_{12} \\ \mathbf{\Phi}_{21} & \mathbf{\Phi}_{22} \end{bmatrix} \begin{bmatrix} \mathbf{V}^s(0,s) \\ \mathbf{I}(0,s) \end{bmatrix} + \begin{bmatrix} \mathbf{V}_{TF}(l,s) \\ \mathbf{I}_{TF}(l,s) \end{bmatrix} \tag{3-36}$$

in which

$$\boldsymbol{\Phi}_{11} = \cosh(\sqrt{\mathbf{ZY}}l) \tag{3-37a}$$

$$\boldsymbol{\Phi}_{12} = -\sinh(\sqrt{\mathbf{ZY}}l)\mathbf{Z_C} \tag{3-37b}$$

$$\boldsymbol{\Phi}_{21} = -\mathbf{Y_C}\sinh(\sqrt{\mathbf{ZY}}l) \tag{3-37c}$$

$$\boldsymbol{\Phi}_{22} = \mathbf{Y_C}\cosh(\sqrt{\mathbf{ZY}}l)\mathbf{Z_C} \tag{3-37d}$$

with

$$\mathbf{Z_C} = \sqrt{\mathbf{ZY}}\mathbf{Y}^{-1} = (\sqrt{\mathbf{ZY}})^{-1}\mathbf{Z}; \quad \mathbf{Y_C} = \mathbf{Z_C^{-1}} \tag{3-38}$$

Then, after several mathematical manipulations, we can get

$$\mathbf{V}^s(l,s) + \mathbf{Z_C}(s)\mathbf{I}(l,s) = \mathbf{H}(s)\left[\mathbf{V}^s(0,s) + \mathbf{Z_C}(s)\mathbf{I}(0,s)\right] + \mathbf{V}_{sF}(s) \tag{3-39a}$$

$$\mathbf{V}^s(0,s) - \mathbf{Z_C}(s)\mathbf{I}(0,s) = \mathbf{H}(s)\left[\mathbf{V}^s(l,s) - \mathbf{Z_C}(s)\mathbf{I}(l,s)\right] + \mathbf{V}_{sB}(s) \tag{3-39b}$$

with $\mathbf{H}(s) = e^{-\sqrt{\mathbf{ZY}}l}$ and

$$\mathbf{V}_{sF}(s) = \mathbf{V}_{TF}(l,s) + \mathbf{Z_C}(s)\mathbf{I}_{TF}(l,s) = e^{-\sqrt{\mathbf{ZY}}l}\mathbf{F}'(s)\int_0^l e^{\left(\sqrt{\mathbf{ZY}}-sk_x\mathbf{U}_{2n}\right)x}dx = $$
$$e^{-\sqrt{\mathbf{ZY}}l}\left(\sqrt{\mathbf{ZY}} - jk_x\mathbf{U}_{2n}\right)^{-1}\left(e^{\left(\sqrt{\mathbf{ZY}}-jk_x\mathbf{U}_{2n}\right)l} - \mathbf{U}_{2n}\right)\mathbf{F}'(s) \tag{3-40a}$$

$$\mathbf{V}_{sB}(s) = -e^{-\sqrt{\mathbf{ZY}}l}\left(\mathbf{V}_{TF}(l,s) - \mathbf{Z_C}(s)\mathbf{I}_{TF}(l,s)\right) = -\mathbf{F}'(s)\int_0^l e^{\left(-\sqrt{\mathbf{ZY}}-jk_x\mathbf{U}_{2n}\right)x}dx = $$
$$\left(\sqrt{\mathbf{ZY}} + jk_x\mathbf{U}_{2n}\right)^{-1}\left(e^{-\left(\sqrt{\mathbf{ZY}}+jk_x\mathbf{U}_{2n}\right)l} - \mathbf{U}_{2n}\right)\mathbf{F}'(s) \tag{3-40b}$$

representing the total effects of the distributed sources related to incident field at the terminal ends of the model.

Analogizing with (2-2), the proposed macromodel in Figure 2.22 can be extended to model equations in (3-39) by adding extra voltage sources, as shown in Figure 3-41. The voltage sources realize

$$\mathbf{V}_{sB}(t) = \begin{bmatrix} V_{sB1}(t) \\ V_{sB2}(t) \end{bmatrix}; \quad \mathbf{V}_{sF}(t) = \begin{bmatrix} V_{sF1}(t) \\ V_{sF2}(t) \end{bmatrix} \tag{3-41}$$

in which $\mathbf{V}_{sB}(t)$ and $\mathbf{V}_{sF}(t)$ are inverse transformations of $\mathbf{V}_{sB}(s)$ and $\mathbf{V}_{sF}(s)$ in (3-39) from Laplace domain to time domain. All other controlled voltage sources are similar to those in Figure 2.22, so they are not to be clarified here. We denote the equivalent circuit in Figure 3.7 as internal excited model corresponding with external excited model in Figure 3.6.
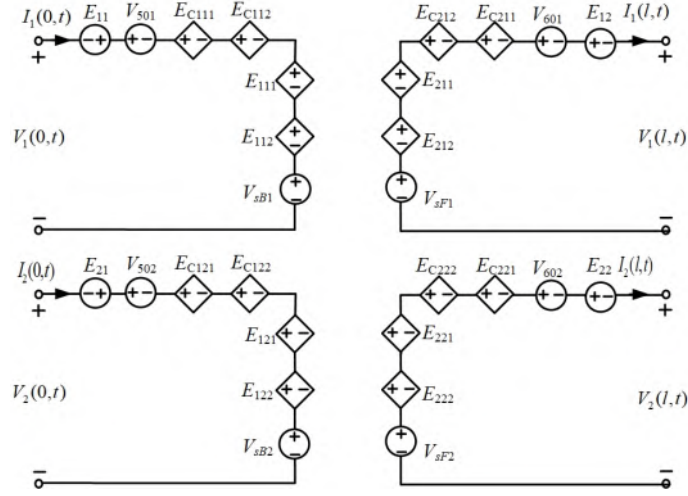
Figure 3.7 Equivalent circuit of incident field coupling to a 2-conductor TLs (internal excited)

Here, based on the above analysis, we summarize the following steps to build an ABM-based MoC macromodel for incident field coupling to overhead MTLs described by (3-1)-(3-4):

1. Identify the method (empirical formulae or numerical procedures) to generate the p.u.l parameters $\mathbf{L}$, $\mathbf{C}$, $\mathbf{Z}_g(s)$ and $\mathbf{Y}_g(s)$;

2. Using the sufficient condition of passivity verification in 2.5 to check if $\mathbf{Z}(s)$ and $\mathbf{Y}(s)$ are both PR;

3. Generate excited source files with the suffix '.stl'. These files are written in the form of syntax of time-domain piecewise linear sources in SPICE;

4. Choose the appropriate implementation methods of frequency-domain devices in the macromodel (FREQ or LAPLACE parts), and confirm the definition parameters using relevant rules, such as f_{MAX} and $NFFT$;

5. Prepare the netlists of the overall macromodel, and embed them into SPICE environment to perform the transient analysis.

3.2 Derivation of the macromodel for field coupling to the TL network

The preceding development of the macromodel has focused on overhead MTLs to external field coupling. In this section, the propagation and field coupling study will move to cases of TL networks.

3.2.1 Configuration and modeling of the TL network

Figure 3.8 illustrates a typical example of one-to-two network topology formed by three single conductors above lossy ground. These conductors are connected either with an impedance at their ends, or to one or more additional conductors. In order to compute the voltage and

current responses at the nodes of network excited by external fields or lumped sources, we primarily put forward several conditions to simplify this problem. The coupling between the line segments is only probably through the interaction of parallel lines, and the voltage/current relationships at the junctions. That is, the mutual coupling between the currents and charges on each of the non-parallel TL branches in the network is neglected.
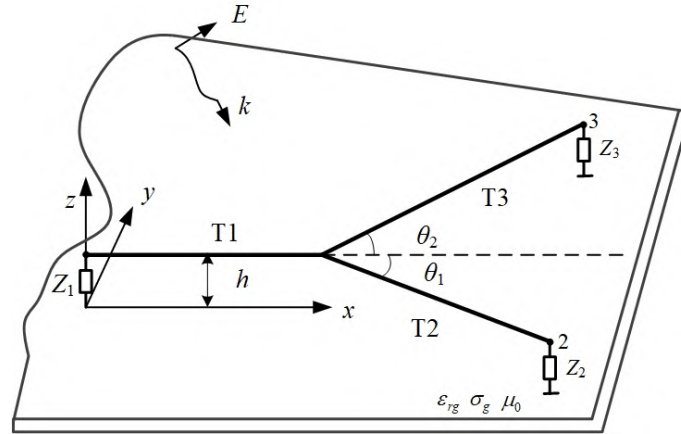
Figure 3.8　A TL network formed by interconnection of TLs

There are several different approaches for treating such networks. A general approach is to develop a BLT equation for the entire linear network, then solve for the voltages/currents at each nodes of the network[136]. However, this frequency-domain method is limited to analyze systems with linear and invariant elements, when it comes to nonlinear devices and processes, the macromodel of TLs excited by external field is recommended to obtain the responses of the network. Besides, as mentioned above, the macromodel is featured with modularity and independence, so it can decompose complex networks into several parts and greatly simplify the modeling and calculation processes, especially for huge networks with MTLs. The specific modeling process are presented below according to a simple TL network in Figure 3.8.

The observation locations must be firstly specified among all junctions loaded with impedance in network. Consider a simple TL network illustrated in Figure 3.8, in which the currents flowing through the impedance Z_1, Z_2 and Z_3 are desired responses, this network can easily be divided into three segments, i.e. the conductor T1 with the load Z_1, T2 with the load Z_2 and T3 with the load Z_3, respectively. Hence, the complete macromodel of the network is composed of three two-port sub-models, as shown in Figure 3.9, and each of them can be realized in accordance with advocated models in Figure 3.6 or Figure 3.7.

Then, there is only one point left concerning the modification of excitation source expression in (3-1) deserves elaboration. We must point out that all expressions related with excitation field should be formulated based on a consistent zero time, but different rectangular coordinates. Generally, each conductor in the network has their own local coordinate system, in which conductors are always parallel with the x-axis. However, the zero time of transient
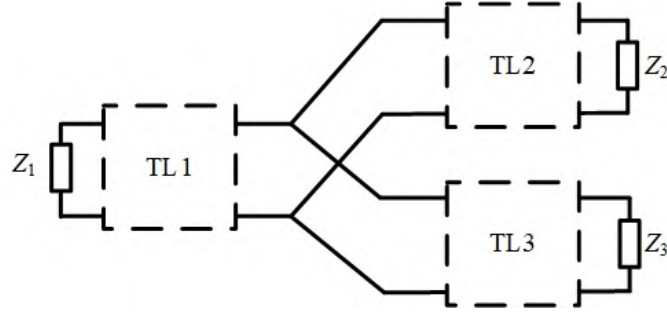
Figure 3.9 The macromodel of the TL network in Figure 3.8

analysis for networks with MTLs is always set up as the time point when plane wave propagates until arriving at one of ends on TLs for the first time. For the network in Figure 3.8, the coordinate system of T1 has been depicted out. Assuming that the time when incident field arrives at the node 1 on T1 is the zero time, and the parameters of incident field in coordinate of T1 are α_1, ψ_1 and ϕ_1. For insuring the consistent zero time of all conductors, the expression E_x^{ex} in (3-1) for T2 and T3 must be modified to realize the time of flight, i.e,

$$E_x^{ex} = E_x^{ex} \times e^{-jk_x l_1} \tag{3-42}$$

in which l_1 is the length of conductor T1. And also, angle parameters of incident field are also changed for T2 and T3 in their local coordinate systems. The azimuthal angles for T2 and T3 are:

$$\phi_2 = \phi_1 - \theta_1 \tag{3-43a}$$

$$\phi_3 = \phi_1 + \theta_2 \tag{3-43b}$$

The other two angles are unchanged. Once the macromodels of all conductors are established, they can be combined together and perform the transient analysis as sub-circuits in the SPICE solver.

3.2.2 Simplification of the network model by Thevenin transformation

The discrete branches with linear loads can be equivalent to one-port Thevenin circuits, which are just composed by voltage sources and input impedances. Then they are combined with models of other branches to get responses at a specified observation point. We also consider the simple three-branch network in Figure 3.8, in which Z_1 is assumed to be a linear load, and the current responses of Z_2 and Z_3 are desired. As shown in Figure 3.10, the T1 with Z_1 can be replaced by an equivalent Thevenin circuit containing an open-circuit voltage V_{eq1} and an input impedance Z_{in1}. For completing this kind of transformation, expressions of the V_{eq1} and Z_{in1} are needed. There are several methods to derive these two formulae, here we

start from the equation (3-36), just substituting scattering voltage $\mathbf{V}^s(l, s)$ with total voltage $\mathbf{V}(l, s)$:
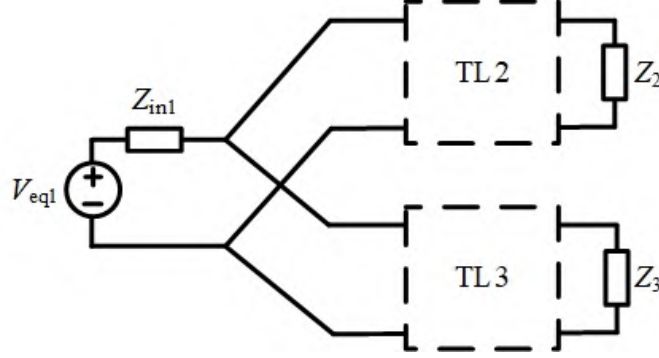
Figure 3.10 Collapse of the TL network in Figure 3.8 using Tevenin circuit

$$\begin{bmatrix} \mathbf{V}(l, s) \\ \mathbf{I}(l, s) \end{bmatrix} = \begin{bmatrix} \mathbf{\Phi}_{11} & \mathbf{\Phi}_{12} \\ \mathbf{\Phi}_{21} & \mathbf{\Phi}_{22} \end{bmatrix} \begin{bmatrix} \mathbf{V}(0, s) \\ \mathbf{I}(0, s) \end{bmatrix} + \begin{bmatrix} \mathbf{V}_{TF}(l, s) \\ \mathbf{I}_{TF}(l, s) \end{bmatrix} \tag{3-44}$$

It should be noted that the forcing function can also be obtained by (3-28)-(3-29), but the $\mathbf{V}_F(s, x)$ and $\mathbf{I}_F(s, x)$ change to

$$\mathbf{V}_F(s, x) = \begin{bmatrix} \vdots \\ -\frac{\partial}{\partial x} \int_0^{h_i} E_x^{ex}(x, y_i, z) dz + E_x^{ex}(x, y_i, h_i) \\ \vdots \end{bmatrix} \tag{3-45a}$$

$$\mathbf{I}_F(s, x) = -\mathbf{Y}(s) \begin{bmatrix} \vdots \\ \int_0^{h_i} E_x^{ex}(x, y_i, z) dz \\ \vdots \end{bmatrix} \tag{3-45b}$$

We also have the boundary condition $\mathbf{V}(0, s) = -\mathbf{Z}_1 \mathbf{I}(0, s)$, and $\mathbf{Z}_1$ is the diagonal matrix containing the load impedances of conductors. Substituting it into (3-44) gives

$$\begin{aligned} \mathbf{V}(l, s) &= (-\mathbf{\Phi}_{11} \mathbf{Z}_1 + \mathbf{\Phi}_{12}) (\mathbf{\Phi}_{22} - \mathbf{\Phi}_{21} \mathbf{Z}_1)^{-1} \mathbf{I}(l, s) \\ &+ \mathbf{V}_{TF}(l, s) - (-\mathbf{\Phi}_{11} \mathbf{Z}_1 + \mathbf{\Phi}_{12}) (\mathbf{\Phi}_{22} - \mathbf{\Phi}_{21} \mathbf{Z}_1)^{-1} \mathbf{I}_{TF}(l, s) \end{aligned} \tag{3-46}$$

Then, the Thevenin circuit of T1 will be realized in Figure 3.9 according to (3-46), just by reducing it to a scalar equation. So the expressions of V_{eq1} and Z_{in1} can be written as

$$Z_{in1} = -(-\Phi_{11}Z_1 + \Phi_{12})(\Phi_{22} - \Phi_{21}Z_1)^{-1} \tag{3-47a}$$

$$V_{eq1} = \mathrm{V}_{TF}(l, s) - (-\Phi_{11}Z_1 + \Phi_{12})(\Phi_{22} - \Phi_{21}Z_1)^{-1} \mathrm{I}_{TF}(l, s) \tag{3-47b}$$

As outlined on the previous chapter, the frequency-dependent impedance Z_{in1} can be modeled directly by the frequency-domain devices (LAPLACE or FREQ). So the Thevenin equivalent circuit is straightforward to be implemented in SPICE and interconnected with other sub-models in the network. Evidently, some networks may require multiple Thevenin transformations to collapse the branches to the observation point, during which multiple excitation including incident field and lumped sources provided by other equivalent circuit must be deduced and expressed prudently.

3.3 Accuracy and efficiency validation by simulation

In this section, five examples are studied and analyzed to validate the proposed macro-modeling approach for not only overhead MTLs but TL networks to field coupling. The simulation results and times are compared with those of other macromodels. Numerical studies of induced responses concerning parameters of lines and lossy ground are also carried out. The simulations are implemeted using PSpice on a PC equipped with an INTEL i7 3.6-GHz CPU.

3.3.1 Example 1: the transient field coupling to a single-conductor TL

This example is devoted to study the transient plane wave coupling to a single-conductor TL[137] terminated with linear loads. In addition, effects of line and ground parameters, and $\mathbf{Z}_g$ formulations on transient responses are also studied in this example. The power line LJ35 is made of aluminum with the conductivity being 3.45×10^7 S/m. This example refers to a TL terminated by its characteristic impedance and placed at 2 m height above a lossy ground. The conductor radius a is 3.31 mm. This conductor is illuminated by a double-exponential pulse, with $\alpha=90°$, $\psi=33°$ and $\phi=90°$. The time expression of the amplitude of the incident field is $E_0(t) = 1.3 \times 20 \times (e^{-t \times 4 \times 10^7} - e^{-t \times 6 \times 10^8})$ kV/m.

1) Accuracy and efficiency validation

To validate the accuracy of the proposed macromodels in Figure 3.6 and Figure 3.7, the induced currents at the near end for different line lengths are calculated using the proposed macromodels and shown in Figure 3.11. For comparison, in Figure 3.11, we also plotted the results in [137]. Besides, in accordance with the ground impedance adopted in [137], the expression in (3-13) is utilized firstly here, and the effect of different $\mathbf{Z}_g$ expressions on transient responses will be discussed later.

The frequency-domain LAPLACE device is adopted in the macromodels of this example. To insure the accuracy of the transient analysis, the time resolution of input files of excitation sources in macromodels is 1.22×10^{-10} s and the length of transient analysis $TSTOP$ is 1 μs. Figure 3.11 shows the induced currents at the near end when the line length is 10 m, 50 m
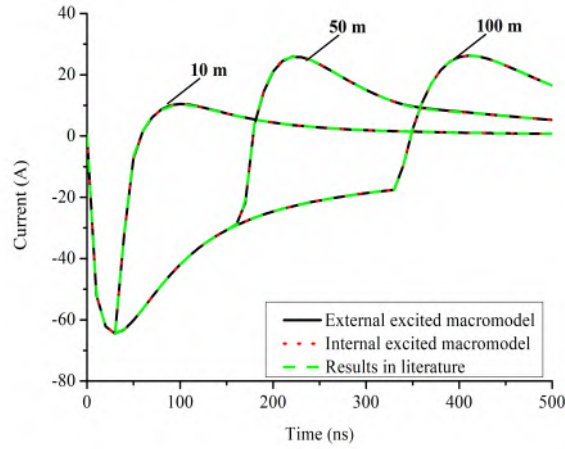
Figure 3.11 The induced currents at the near end for different line lengths ($\sigma_g = 0.001$ S/m, $\varepsilon_{rg}=4$)

Table 3.1 CPU time comparison of two macromodels

Simulations	External excited macromodel (s)	Internal excited macromodel (s)
10 m	3.53	3.16
50 m	3.61	3.22
100 m	3.75	3.45

and 100 m, respectively. The results of three lengths obtained by external and internal excited macromodels agree well with the results in [137]. The maximum deviation of peak values among three cases is about 0.28 A, corresponding to 9 % of the peak value of currents. In addition, the simulation times of two macromodels are compared in Table 3.1. It should be noted that the internal excited model is a little bit faster than another one, which may owe to its simpler model structure, and it can be speculated that this merit will be more highlighted for more number of conductors. Hence, the internal excited macromodel will be utilized and denoted as 'proposed macromodel' for simplification in the following context.

2) The effect of different $\mathbf{Z}_g$ formulations on transient responses

As introduced in section 3.1.2, there are two kinds of widely used expressions of ground impedance $\mathbf{Z}_g$ formulated in a wide frequency range. The expression in (3-3) is proposed and then simplified into a logarithmic form by Sunde, another one in (3-16) is modeled by D'Amore et al. based on a rigorous derivation from Maxwell equations. Hence, this part is devoted to investigate the influence of these two formulations on transient responses. The induced currents at the near end for different ground conductivities σ_g are calculated when length is 100 m, the results are compared in Figure 3.12. All other parameters of incident field and the TL remain the same.
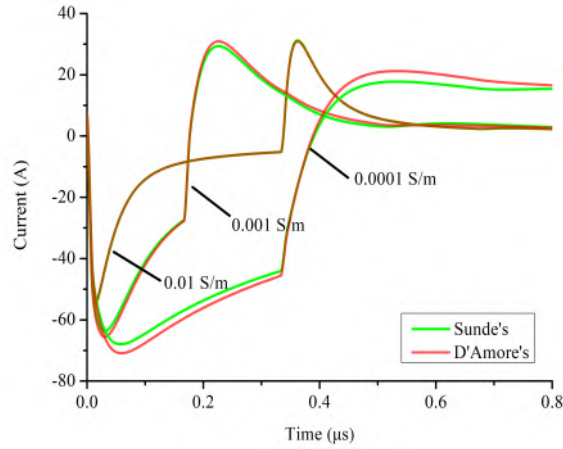
Figure 3.12 Comparison of induced currents at the near end using Sunde's expression (black dash curves) and D'Amore's expression (green solid curves) when ε_{rg}=4

It is important to observe from Figure 3.12 that the curves obtained by $\mathbf{Z}_g$ expression of D'Amore are characterized by greater peak value and steeper wavefront. The differences are more evident for lower ground conductivities. The maximum deviation of peak values among all curves is about 2.96 A, which refers to σ_g=0.0001 S/m. While for typical σ_g values ranging from 10^{-3} to 10^{-2} S/m, the transient responses obtained by these two formulations are similar.
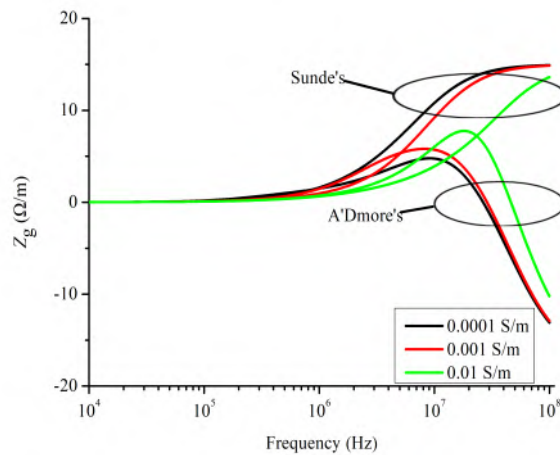
Figure 3.13 Comparison of real part of $\mathbf{Z}(s)$ at the near end using Sunde's expression and D'Amore's expression for different σ_g

We also plotted the real part of p.u.l impedance $\mathbf{Z}(s)$ corresponding to two different $\mathbf{Z}_g$, as shown in Figure 3.13. It is clear that the real part of $\mathbf{Z}(s)$ obtained by D'Amore's expression will go below 0 for frequencies higher than a few dozens of MHz. Hence, because the frequency spectrum of the excitation field can be up to a few hundreds of MHz, the passivity of

the developed macromodel cannot be guaranteed. Besides, considering the computation complexity of these two expressions, the Sunde's logarithmic approximation of $\mathbf{Z}_g$ is preferable, and will be utilized by default in the following simulation unless otherwise specified.

3) The influence of line parameters on transient responses
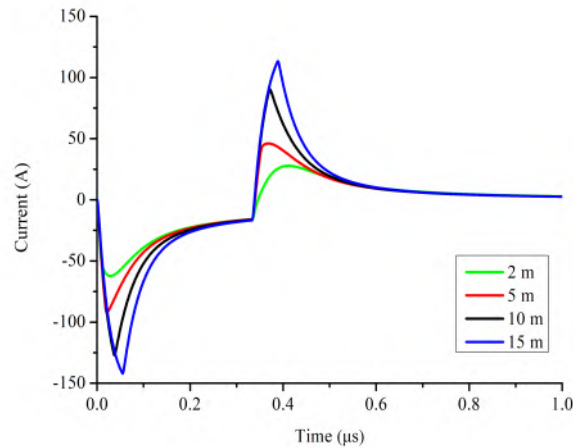
Figure 3.14 Comparison of induced currents at the near end for different heights

From Figure 3.11, the magnitudes of current responses maintain constant for lengths longer than 10 m. In fact, according to [137], we have known that the responses due to uniform electromagnetic fields on TLs will increase with the growth of the line length until it reaches and exceeds the critical length. So for the circumstance in this example, the critical length is at most 10 m or even shorter.

Then, in order to study the line height's impact on transient responses, the induced currents at the near end for different heights when length is 100 m are calculated and shown in Figure 3.14, all other parameters are fixed. We can see that the peak value and pulse-width of the current response becomes larger with the increase of the line height.

4) The influence of lossy ground on transient responses

As shown earlier in Figure 3.12, the ground conductivity can significantly affect the induced currents in magnitude, shape, and polarity. In particular, the peak value and pulse-width of the induced current becomes lower with the increase of the ground conductivity. In fact, the intensity of the electromagnetic field reflected from the ground becomes stronger when the conductivity increases. As a result, the electromagnetic field along the x axis becomes smaller.

Then, the induced current at the near end for different ground relative permittivities ε_{rg} are calculated and compared in Figure 3.15, when σ_g=0.001, height is 2 m and length is 100 m. It can be seen that, for the common real ground ($\varepsilon_{rg} = 1 - 10$), the peak value of the
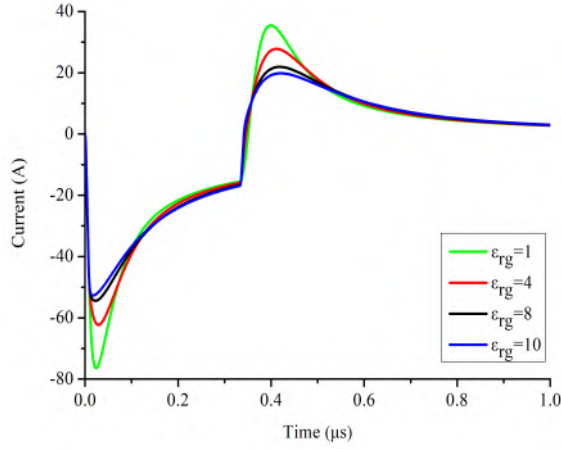
Figure 3.15 Comparison of induced currents at the near end for different ε_{rg}

induced current becomes lower with the increase of the relative permittivity, though its effect on pulse-width will not be significant compared with the ground conductivity.

3.3.2 Example 2: the transient field coupling to three-phase TLs
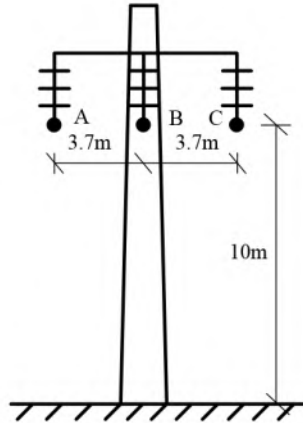
Figure 3.16 Configuration of three-phase overhead TLs

This example will focus on demonstrating the validity of the proposed macromodel for field coupling to MTLs terminated with nonlinear loads. In this example, the incident field couples to a 100 m-long horizontally-configured three-phase 35 kV power TLs loaded with metal oxide arresters (MOA), for which the configuration is shown in Figure 3.16. The three conductors are all located at a height of 10 m above the ground, with radius a_i ($i = 1, 2, 3$) is 0.01 cm. The ground conductivity σ_g equals to 0.01 S/m, and the relative ground permittivity ε_{rg} is 10. The expression of the amplitude of incident field is $E_0(t) = 65 \times (e^{-t \times 4 \times 10^7} - e^{-t \times 6 \times 10^8})$ kV/m, with $\alpha=0°$, $\psi=30°$ and $\phi=0°$. The MOA behaves as a nonlinear device and its V-I characteristic has the same feature as what Figure 2.8 shows, which can be described by three

exponential segments, as follows:

$$V = \begin{cases} 146.46 \times 10^3 \cdot I^{0.2} & ,0mA \leq I < 1mA \\ 51.97 \times 10^3 \cdot I^{0.05} & ,1mA \leq I < 1A \\ 51.97 \times 10^3 \cdot I^{0.06} & ,1A \leq I < 6kA \end{cases} \tag{3-48}$$
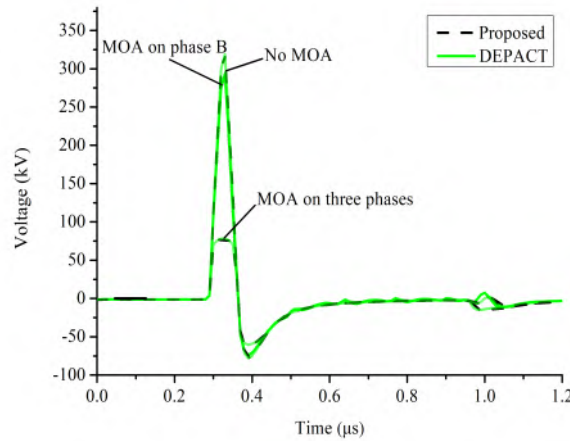
(a) Induced voltages at the far end of phase A
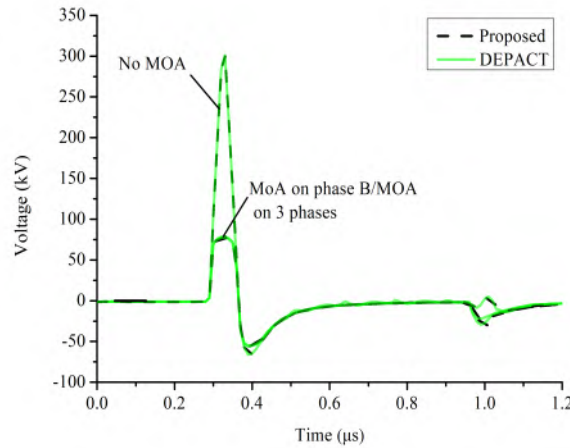
(b) Induced voltages at the far end of phase B

Figure 3.17 The induced voltages at the far end of lines. No MOA refers to scenario (i); MOA on phase B refers to scenario (ii); MOA on 3 phases refers to scenario (iii)

There are three scenarios to be investigated here: (i) the three phases are terminated with their characteristic impedances; (ii) the far end of phase B is loaded with extra MOA in parallel with its characteristic impedance, while phase A and C are not; (iii) the far end of three phases are all loaded with characteristic impedance in parallel with MOA devices. Evidently, the

responses on phase A and B are same due to their symmetrical position, hence in Figure 3.17, the induced voltages at the far end of phase A and phase B for different scenarios are calculated with the proposed macromodel and compared with the results of the DEPACT macromodel.

As we can see, the results obtained by proposed macromodel and DEPACT macromodel are all in excellent agreement, which demonstrates the validity of the proposed macromodel for dealing with field coupling to MTLs terminated with linear and nonlinear loads described in scenarios (i)-(iii). Comparing the responses in Figure 3.17(a) and Figure 3.17(b) firstly, the MOA can not only reduce induced voltages on phases with MOA effectively, but influence another phase through coupling effects between each conductors, though the protection is not reliable enough. Hence, the placement of MOA on each phase is more reliable for protection of lines and devices at the terminal ends.

3.3.3 Example 3: the influence assessment of overhead ground wires
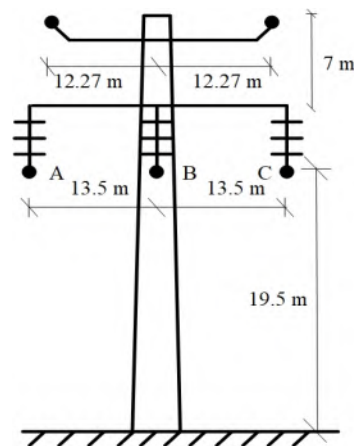
Figure 3.18 Configuration of three-phase overhead TLs with double ground wires
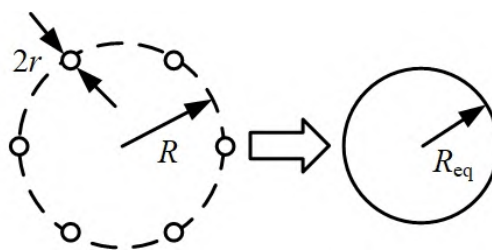
Figure 3.19 Geometry of six-splitting conductors and equivalent single conductor

In this section, we will take a 1000 m-long horizontally-configured three-phase 750 kV power TLs shown in Figure 3.18 as an example, to study the influence of overhead ground wires on transient responses of overhead MTLs to incident field coupling. The specific parameters are as follows: the six-splitting conductors are generally adopted by 750 kV power TLs with the type of sub-conductor being LGJ-400/50, as shown in Figure 3.19, and the spacing of bundle conductors is 400 mm; the double ground wires are made of galvanized steel, and the type
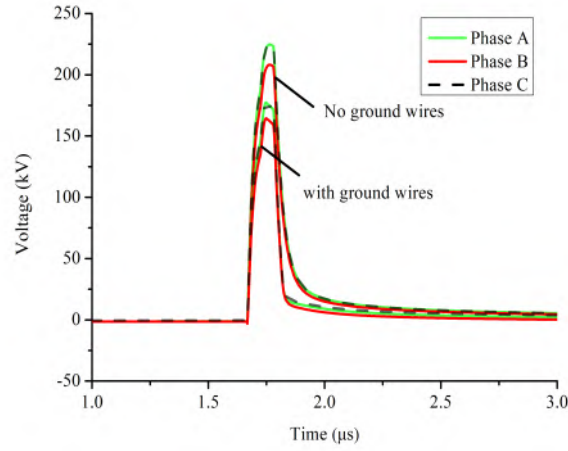
Figure 3.20 Induced voltages on three phases with and without ground wires

is JLB20A-150; the tower adopts a wine-glass type with two ground wires and three-phase conductors; The height and distance of these lines have been shown in Figure 3.18. According to 3.1.3, the splitting sub-conductors can be equivalent to a single conductor, and the equivalent radius in this example is 0.3077 m. The σ_g equals to 0.01 S/m, and ε_{rg} is 10. The expression of the amplitude of the incident field is $E_0(t) = 65 \times (e^{-t \times 4 \times 10^7} - e^{-t \times 6 \times 10^8})$ kV/m, with $\alpha = 0°$, $\psi = 60°$ and $\phi = 0°$.

The three phases are terminated with their characteristic impedances, the double ground wires are connected to the earth through small ground resistances, which are all taken as $10 \ \Omega$ here. The induced voltages at the far ends of three phases with and without the consideration of ground wires are calculated by the proposed macromodel, Figure 3.20 shows the comparison results. From Figure 3.20, the overhead ground wires have a certain shielding effect of incident field, which can reduce the induced voltages on three-phase TLs. Hence, the effect of ground wires must be taken into consideration when modeling the real power TL systems.

3.3.4 Example 4: the efficiency assessment of the proposed macromodel

This example is aimed at assessing the calculation efficiency of the proposed model compared with other existing macromodels. Three configurations are chosen in this example for the efficiency assessment of the proposed macromodel. The transient plane wave coupling to different lengths of single-, two- and three-conductor overhead TLs terminated by their respective characteristic impedance are simulated. All lines are placed at 10-m height, and other parameters referred to ground and incident field are the same as those in Example 2. To demonstrate the efficiency, we compare the results of proposed model in Figure 3.7 with other two macromodeling algorithms, including generalized MoC with delay extraction and DEPACT with both delay extraction and sectioning method. In this example, the 50 m-long and 500

m-long TLs are divided into 4 and 12 segments for DEPACT models in order to ensure that the relative errors are all less than 6 % considering a frequency band up to 100 MHz. The induced voltages at the far end for different lengths are shown in Figure 3.21 - Figure 3.23. Table 3.2 presents a comparison of the CPU time.
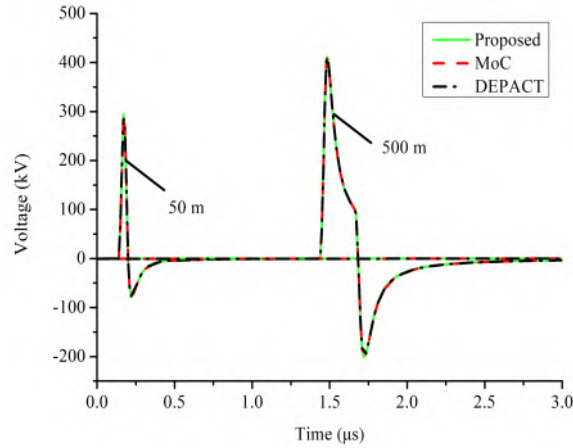
Figure 3.21 Induced voltages at the far end of a single conductor for different lengths
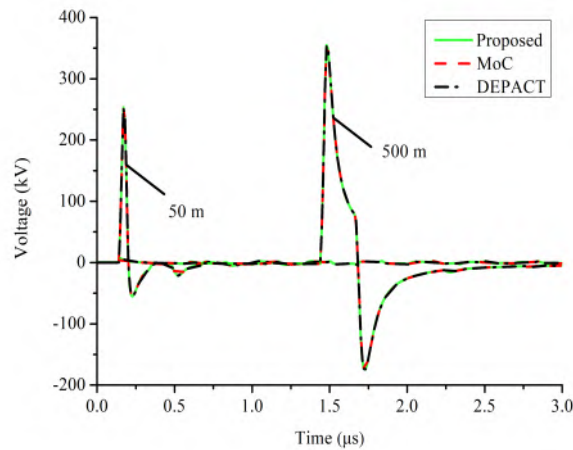
Figure 3.22 Induced voltages at the far end of two conductors for different lengths

As Figure 3.21 to Figure 3.23 show, the responses of these algorithms match well with each other for three configurations. Table 3.2 provides a comparison of the CPU time of the proposed method, conventional MoC and DEPACT. It should be noted that the proposed method is markedly faster than the other two modeling methods. Just as shown, the proposed method is 4x to 16x faster than the DEPACT method, and 2x to 3x faster than the conventional MoC. Besides, the efficiency of the proposed algorithm has less to do with the line length, which ensures that the efficiency would not be limited by the line length.
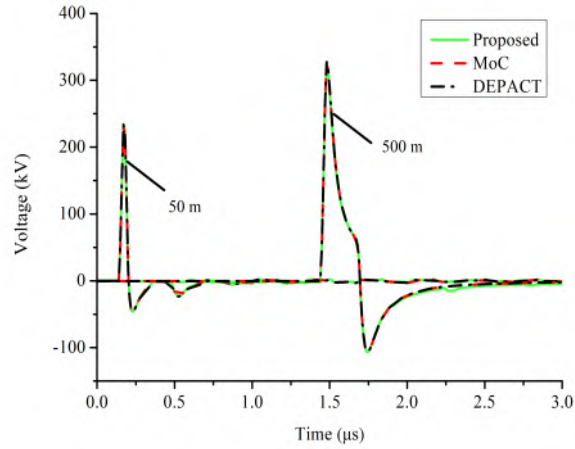
Figure 3.23 Induced voltages at the far end of three conductors for different lengths

Table 3.2 CPU time comparison of different macromodels

Model	single		Two		Three	
	50 m	500 m	50 m	500 m	50 m	500 m
Proposed (s)	1.84	2.00	8.71	8.64	10.26	11.99
MoC (s)	7.97	8.24	15.21	16.82	31.20	34.51
DEPACT (s)	28.03	76.05	39.19	85.56	42.60	90.56

3.3.5 Example 5: the transient field coupling to a TL network
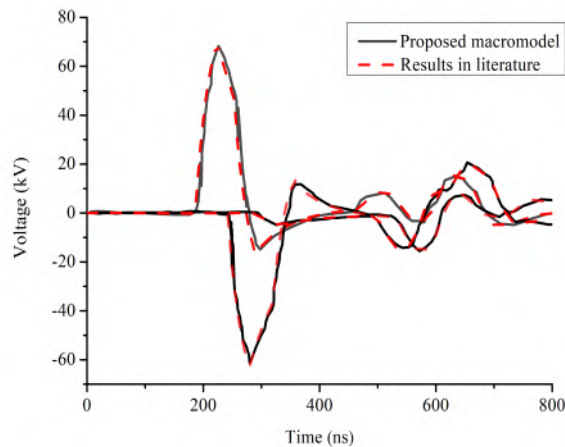
Figure 3.24 Induced voltages on the terminal ends obtained via macromodel and BLT equation

In this example, the research is focused on a TL network above lossy ground, whose configuration has been shown in Figure 3.8. The lengths of T1, T2 and T3 are 50 m, 60 m and

40 m, respectively. The angles θ_1 and θ_2, which are the angles between T2 and T3 with the x-axis, are $30°$ and $45°$, respectively. The height of the network is 8 m and the radii of all TLs are 1 mm. The loads of the network Z_1, Z_2 and Z_3 are all 100 Ω. The σ_g equals to 0.001 S/m, and ε_{rg} is 4. This network is illuminated by a double-exponential pulse, with time expression of the amplitude is $E_0(t) = 1.3 \times 50 \times (e^{-t \times 4 \times 10^7} - e^{-t \times 6 \times 10^8})$ kV/m. The parameter of angles are $\alpha=90°$, $\psi=45°$ and $\phi=0°$. The induced voltages on Z_1, Z_2 and Z_3 obtained by the macromodel in Figure 3.9 are depicted in Figure 3.24, and for comparison, the results in [137] obtained by BLT equation are also shown in figure. It is obvious that the induced voltages obtained by two different methods agree well with each other, which proves the validity of the proposed macromodel for TL network to field coupling.

Then, if only responses on Z_2 and Z_3 are required, and because Z_1 is a linear load, the network macromodel can be simplified to the model in Figure 3.10. The induced voltages on Z_2 and Z_3 obtained by the simplified model are shown in Figure 3.25. For the sake of comparison, the results of the complete macromodel are again shown in Figure 3.25.
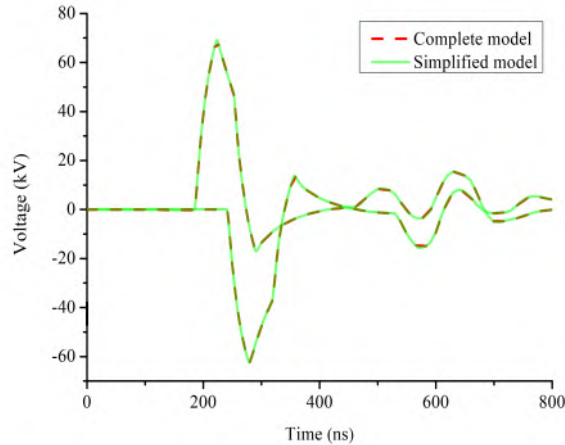
Figure 3.25 Induced voltages on the terminal ends obtained via complete and simplified macromodels

The results in Figure 3.25 shows that the voltages on loads Z_2 and Z_3 obtained by the simplified model are the same with those obtained by the complete macromodel of network. But the simplified model just consumes 8.03 s to carry out the simulation, and it is markedly faster compared with 11.45 s costed by the complete macromodel.

3.4 Concluding remarks

Based on the time-domain macromodeling algorithm for MTLs proposed in chapter 2, this chapter extends it by including the excitation of external field and lossy ground to model overhead MTLs and TL networks to field coupling.

We start from the formulation of field coupling to overhead MTLs above lossy ground.

And specifically, the expressions of p.u.l parameters, especially for ground impedance, are elaborated and discussed. Then the macromodel is established by incorporating the excitation sources with the TL model, and according to the position relationship between excitation sources and the TL model, the macromodels are divided into external excited and internal excited models. Finally, taking a one-to-two overhead TL network as an example, the modularity and independence of macromodel are utilized to model the TL network, by connecting two-port sub-models together. In addition, for certain scenarios, we proposed a simplified model of the network based on Thevenin transformation, in which the discrete branches of the network is equivalent to a one-port Thevenin circuit.

Several examples are presented in this chapter, including field coupling to overhead single-conductor TL, MTLs, and TL network. According to the numerical validation, the proposed macromodel is proved to be accurate and efficient enough to deal with the cases of long-distance MTLs and wide-area TL networks terminated with linear and nonlinear loads to field coupling. The macromodel has been utilized to carry out numerical studies about effects of line parameters, lossy ground, and ground wires on induced responses.

Last but not the least, the ground parameters (relative permittivity ε_{rg} and conductivity σ_g) are considered as constants here. The frequency dependency of ground parameters can also be readily taken into account by the proposed macrmodel without any difficulty once the frequency dependence of these electrical parameters in the typical frequency range of interest are accurately characterized. An extension of model to the field coupling to buried wires will be considered in the research work of the next chapter.

4 A time-domain macromodel for field coupling to underground cables

From the perspective of practical applications, it has been proven that in most cases, the TL theory is a valid and beneficial approximation for problems of underground TLs to field coupling[54]. In fact, due to the presence of nonlinear components and phenomena in transmission systems, an efficient and accurate time-domain method for straightforward transient evaluation of underground lines is desirable. FDTD method, the most commonly used in field-to-buried wire cases, is inadequate because of several challenges in implementation process and inefficient simulation. Hence, a macromodeling algorithm is necessary, but no macromodel for buried cables to field coupling has been developed yet.

In the previous chapter, we have presented a macromodel using ABM and the generalized MoC for field coupling to overhead MTLs and TL networks. However, on the one hand, compared with overhead lines, cables are more commonly used in underground power and communication systems. The cable could have multiple metallic layers, and the induced voltages and currents on outermost layer may couple to not only external environment of the cable, but also to the internal conductors (inner shield or core) due to imperfect shield; on the other hand, in contrast with overhead lines, the contribution of ground admittance is non-negligible in the TL equation of buried cables.

The aim of this chapter is to present a macromodel for buried cables to field coupling that can estimate transient responses on multiple conducting layers of cables. In this chapter, the previous modeling methodology is extended with some modifications to include practical cable arrangements with metallic shield/sheath and internal conductors, and the effect of both ground impedance and admittance. Specifically, the coaxial cable is modeled by decomposing it into several discrete TL systems, in which they couple with each other only through the transfer parameters of each conducting layer. Besides, we adopt a general semi-infinite integral analytic formulation of the self and mutual ground impedance and admittance[138, 139]. To avoid using time-consuming numerical integration techniques, the approximation expressions for both ground impedance and admittance are also proposed in this chapter. Various examples will be studied in this chapter to verify the proposed algorithm. Part of the work described in this chapter has been previously publised in [140] and [141].

The content of this chapter is arranged as follows: in section 4.1, we give a derivation of the time-domain macromodel for underground coaxial cables to field coupling, and formulations of p.u.l ground parameters. Section 4.2 provides three examples to demonstrate the proposed models and carry out numerical studies. Section 4.3 summaries the research work of this chapter.

4.1 Derivation of the macromodel for field coupling to buried cables

4.1.1 Configuration and formulation of field coupling to buried cables

To formulate the plane wave coupling to underground single-core (SC) cables, the general arrangement consist of n ($n \geq 1$) horizontally insulated conductors buried in lossy homogeneous earth, as shown in Figure 4.1 (two cables are depicted for simplification), is considered. The cross-section of the common cable structure used in buried transmission systems are also shown in this figure. The region $z > 0$ is free-space, characterized by permittivity ε_0 and permeability μ_0. The region $z < 0$ is designated as the earth, characterized by relative permittivity ε_{rg}, conductivity σ_g, and free-space permeability μ_0. The j-th cable is buried at a depth of h_j from the earth surface, which consists of an inner conducting core (ε_{1j}, σ_{1j}, μ_{1j}, radius is r_{1j}), an inner insulator (ε_{ins1j}, radius is r_{2j}), a metallic sheath/shield (ε_{2j}, σ_{2j}, μ_{2j}, radius is r_{3j}), and an outer insulator (ε_{ins2j}, radius is r_{4j}). y_{jk} is the horizontal distance between the j-th and k-th cable.

Because the vertical component of electric field E_z^{tran} transmitting into the ground is small enough to be neglected[43], then the voltages and currents along cables induced by external field can be evaluated in terms of Agrawal model equations in Laplace domain as

$$\frac{d}{dx} \begin{bmatrix} \mathbf{V}(x,s) \\ \mathbf{I}(x,s) \end{bmatrix} + \begin{bmatrix} \mathbf{0} & \mathbf{Z}(s) \\ \mathbf{Y}(s) & \mathbf{0} \end{bmatrix} \begin{bmatrix} \mathbf{V}(x,s) \\ \mathbf{I}(x,s) \end{bmatrix} = \begin{bmatrix} \mathbf{E}_x^{tran}(x,s) \\ \mathbf{0} \end{bmatrix} \tag{4-1}$$

For defining the vectors and matrices in (4-1) more clearly, we firstly consider the vertical section of a SC cable, given in Figure 4.2. The coaxial SC cable can be treated as two transmission systems. The outer system is formed with sheath/shield, outer insulator and external return, while the inner system is composed by the inner core, inner insulator and the internal part of the shield/sheath. Define loop currents flowing through inner and outer systems are I_1 and I_2, respectively. Also currents flowing into the core and sheath are I_c and I_s. Voltages between the core, sheath/shield and outer medium (soil) are V_1 and V_2, which can also be referred to loop voltages. The voltages V_c and V_s are those of conducting layers with respect to zero potential reference, respectively. Then, the relations for above currents and voltages are

$$I_1 = I_c; \quad I_2 - I_1 = I_s \tag{4-2a}$$

$$V_1 = V_c - V_s; \quad V_2 = V_s \tag{4-2b}$$

Above relations are useful for transformations by which one can get specific values as needed. Hence, based on the loop voltages and currents, we have wave equations like:
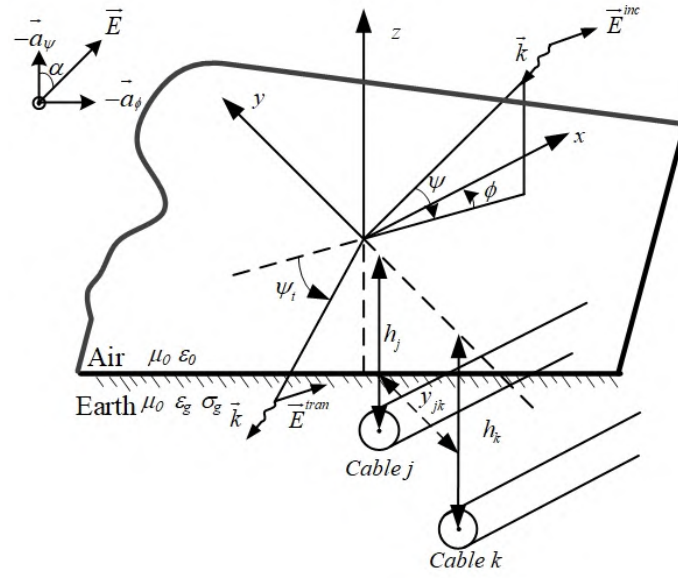
(a) Geometric configuration of buried cables in homogeneous
earth (the geometry of the external field is also illustrated)
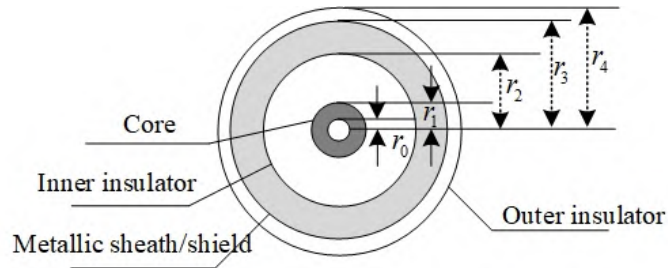
(b) Cross-section of the single-core cable

Figure 4.1 The configuration of buried cables to incident field coupling and the cross-section of a single-core
cable
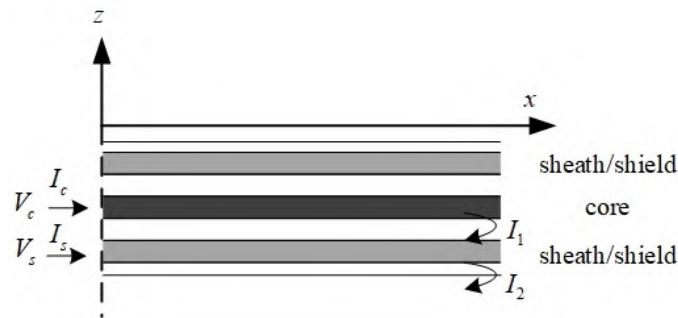
Figure 4.2 Vertical-section of the SC cable

$$\frac{d}{dx}\begin{bmatrix} V_1(x,s) \\ V_2(x,s) \end{bmatrix} + \begin{bmatrix} Z_{11} & Z_{12} \\ Z_{21} & Z_{22} \end{bmatrix}\begin{bmatrix} I_1(x,s) \\ I_2(x,s) \end{bmatrix} = \begin{bmatrix} 0 \\ V_{s2} \end{bmatrix} \qquad (4\text{-}3a)$$

$$\frac{d}{dx}\begin{bmatrix} I_1\,(x,s) \\ I_2\,(x,s) \end{bmatrix} + \begin{bmatrix} Y_{11} & Y_{12} \\ Y_{21} & Y_{22} \end{bmatrix}\begin{bmatrix} V_1\,(x,s) \\ V_2\,(x,s) \end{bmatrix} = \begin{bmatrix} 0 \\ I_{s2} \end{bmatrix} \tag{4-3b}$$

in which $V_{s2} = E_x^{tran}(x,s)$ and $I_{s2} = 0$. The impedance parameters in (4-3a) are defined as

$$Z_{11} = Z_{c-out} + Z_{ins1} + Z_{s-in} \tag{4-4a}$$

$$Z_{12} = Z_{21} = -Z_{s-transfer} \tag{4-4b}$$

$$Z_{22} = Z_{s-out} + Z_{ins2} + Z_g \tag{4-4c}$$

The admittance parameters in (4-3b) are given by

$$Y_{11} = Y_{ins1} \tag{4-5a}$$

$$Y_{12} = Y_{21} = Y_{s-transfer} \tag{4-5b}$$

$$Y_{22} = Y_{ins2}||Z_g \tag{4-5c}$$

Concretely, the component of p.u.l impedances in (4-4) are given as follows: Z_{c-out} is the impedance of core outer surface; Z_{ins1} is the inner insulator impedance with expression $Z_{ins1} = s\mu_0/\,(2\pi)\cdot\ln(r_2/r_1)$; Z_{s-in} is the internal impedance of sheath or shield inner surface; $Z_{s-transfer}$ is the transfer impedance contributing to the coupling between the metallic shield/sheath and inner conductor; Z_{s-out} is the internal impedance of sheath/shield outer surface; Z_{ins2} is the outer insulator impedance with expression $Z_{ins2} = s\mu_0/\,(2\pi)\cdot\ln(r_4/r_3)$; Z_g is the earth return impedance. The p.u.l admittances are composed by terms including: $Y_{ins1} = j\omega C_{ins1} = j\omega 2\pi\varepsilon_0\varepsilon_{ins1}/\ln(r_2/r_1)$ is the admittance of inner insulator; $Y_{s-transfer}$ is the transfer admittance representing the coupling between the outer conducting layer and the inner conductor; $Y_{ins2} = j\omega C_{ins2} = j\omega 2\pi\varepsilon_0\varepsilon_{ins2}/\ln(r_4/r_3)$ is the admittance of outer insulator; Y_g is the earth return admittance.

Hence, vectors $\mathbf{V}_{2n\times 1}$ and $\mathbf{I}_{2n\times 1}$ represent inner and outer loop voltages and currents along n cables; $\mathbf{E}_x^{tran}$ is also a $2n \times 1$ vector representing the horizontal component of the electric field transmitting into the soil. It should be noted that the external field only couples with and induces the response on the outside conductor of cables, so it will be included in the outer loop system. The specific elements in these vectors can be written as

$$\mathbf{V} = [V_{11}, V_{12}, \cdots, V_{j1}, V_{j2}, \cdots, V_{n1}, V_{n2}]^T \tag{4-6a}$$

$$\mathbf{I} = [I_{11}, I_{12}, \cdots, I_{j1}, I_{j2}, \cdots, I_{n1}, I_{n2}]^T \tag{4-6b}$$

$$\mathbf{E}_x^{tran} = \left[0, E_x^{tran}(s,x,y_1,z_1), \cdots, 0, E_x^{tran}(s,x,y_j,z_j), \cdots, 0, E_x^{tran}(s,x,y_n,z_n)\right]^T \tag{4-7}$$

The longitudinal impedance matrix $\mathbf{Z}_{2n \times 2n}$ and transversal admittance matrix $\mathbf{Y}_{2n \times 2n}$ are expressed in the following form

$$\mathbf{Z} = \mathbf{Z}_{in} + \mathbf{Z}_g \tag{4-8a}$$

$$\mathbf{Y} = s\mathbf{P}^{-1} \tag{4-8b}$$

$$\mathbf{P} = \mathbf{P}_{in} + \mathbf{P}_g \tag{4-8c}$$

in which $\mathbf{Z}_{in}$, $\mathbf{P}_{in}$, $\mathbf{Z}_g$ and $\mathbf{P}_g$ denote p.u.l internal impedance, internal potential coefficient, ground impedance and ground potential coefficient matrices respectively, i.e.,

$$\mathbf{Z}_{in} = \begin{bmatrix} [\mathbf{Z}_{in1}] & [\mathbf{0}] & \cdots & [\mathbf{0}] \\ [\mathbf{0}] & [\mathbf{Z}_{in2}] & \cdots & [\mathbf{0}] \\ \vdots & \vdots & \ddots & \vdots \\ [\mathbf{0}] & [\mathbf{0}] & \cdots & [\mathbf{Z}_{inn}] \end{bmatrix}_{2n \times 2n} \tag{4-9}$$

$$\mathbf{Z}_g = \begin{bmatrix} [\mathbf{Z}_{g11}] & [\mathbf{Z}_{g12}] & \cdots & [\mathbf{Z}_{g1n}] \\ [\mathbf{Z}_{g21}] & [\mathbf{Z}_{g22}] & \cdots & [\mathbf{Z}_{g2n}] \\ \vdots & \vdots & \ddots & \vdots \\ [\mathbf{Z}_{gn1}] & [\mathbf{Z}_{gn2}] & \cdots & [\mathbf{Z}_{gnn}] \end{bmatrix}_{2n \times 2n} \tag{4-10}$$

All the off-diagonal submatrices of $\mathbf{Z}_{in}$ are zero, and diagonal submatrices express the self-impedance matrices of SC cables. The self-impedance matrix $[\mathbf{Z}_{inj}]$ $(1 \le j \le n)$ is given by

$$[\mathbf{Z}_{inj}] = \begin{bmatrix} Z_{c-outj} + Z_{ins1j} + Z_{s-inj} & -Z_{s-transferj} \\ -Z_{s-transferj} & Z_{s-outj} + Z_{ins2j} \end{bmatrix} \tag{4-11}$$

Submatrices $[\mathbf{Z}_{gij}])$ $(1 \le i \le n)$ $(1 \le j \le n)$ of the earth return impedance in (4-10) is given by

$$[\mathbf{Z}_{gij}] = \begin{bmatrix} 0 & 0 \\ 0 & Z_{gij} \end{bmatrix} \tag{4-12}$$

The admittance matrix of a cable system is evaluated from the potential coefficient matrix $\mathbf{P}$ as given in (4-8), in which

$$\mathbf{P}_{in} = \begin{bmatrix} [\mathbf{P}_{in1}] & [\mathbf{0}] & \cdots & [\mathbf{0}] \\ [\mathbf{0}] & [\mathbf{P}_{in2}] & \cdots & [\mathbf{0}] \\ \vdots & \vdots & \ddots & \vdots \\ [\mathbf{0}] & [\mathbf{0}] & \cdots & [\mathbf{P}_{inn}] \end{bmatrix}_{2n \times 2n} \tag{4-13}$$

$$\mathbf{P}_g = \begin{bmatrix} [\mathbf{P}_{g11}] & [\mathbf{P}_{g12}] & \cdots & [\mathbf{P}_{g1n}] \\ [\mathbf{P}_{g21}] & [\mathbf{P}_{g22}] & \cdots & [\mathbf{P}_{g2n}] \\ \vdots & \vdots & \ddots & \vdots \\ [\mathbf{P}_{gn1}] & [\mathbf{P}_{gn2}] & \cdots & [\mathbf{P}_{gnn}] \end{bmatrix}_{2n \times 2n} \tag{4-14}$$

All the off-diagonal submatrices of $\mathbf{P}_{in}$ are zero, and diagonal submatrices express the potential matrices of SC cables. The potential matrix $[\mathbf{P}_{inj}]\,(1 \leq j \leq n)$ is given by

$$[\mathbf{P}_{inj}] = \begin{bmatrix} P_{ins1j} & P_{s-transferj} \\ P_{s-transferj} & P_{ins2j} \end{bmatrix} \tag{4-15}$$

with potential coefficients being inversely related to admittances:

$$P_{ins1j} = 1/Y_{ins1j}; \quad P_{s-transferj} = 1/Y_{s-transferj}; \quad P_{ins2j} = 1/Y_{ins2j} \tag{4-16}$$

Submatrices $[\mathbf{P}_{gij}])\,(1 \leq i \leq n)\,(1 \leq j \leq n)$ of the earth return potential in (4-14) is given by

$$[\mathbf{P}_{gij}] = \begin{bmatrix} 0 & 0 \\ 0 & P_{gij} \end{bmatrix} \tag{4-17}$$

4.1.2 Study on characteristics of underground electric field environment

The excitation electromagnetic field environment of underground TLs is the transmitted field of incident waves. Since the vertical component of electric field transmitted into the soil is small enough to be ignored, the induced responses on buried cables are only related to the horizontal component of electric field (x-axis direction in Figure 4.1). For uniform plane waves, the transmitted field E_x^{tran} can be expressed analytically as[43]

$$E_x^{tran} = E_0(\omega)\,[T_v \cos \alpha \sin \psi_t \cos \phi + T_h \sin \alpha \sin \phi]\,e^{-\gamma_g x \cos \psi_t \cos \phi} e^{\gamma_g y \cos \psi \sin \phi} e^{\gamma_g z \sin \psi_t} \tag{4-18}$$

in which $E_0(\omega)$ is the Fourier transform of incident field's time-domain expression; T_v and T_h are vertical and horizontal transmission coefficient, respectively; $\gamma_g = \sqrt{j\omega\mu_0(\sigma_g + j\omega\varepsilon_{rg}\varepsilon_0)}$ is the propagation constant in the ground; The angles α, ψ and ϕ are polarization, elevation and azimuthal angles of incident field; The complex transmission angle ψ_t is the complex transmission angle, as defined in Figure 4.1. By Snell's law, the transmitted angle ψ_t is given by the expression

$$\cos \psi_t = \frac{jk}{\gamma_g} \cos \psi \tag{4-19}$$

with $k = \omega\sqrt{\mu_0\varepsilon_0}$. T_v and T_h can be expressed as

$$T_v = \frac{2n_f \sin\psi}{n_f^2 \sin\psi + \sqrt{n_f^2 - \sin^2\psi}} \tag{4-20a}$$

$$T_h = \frac{2\sin\psi}{\sin\psi + \sqrt{n_f^2 - \cos^2\psi}} \tag{4-20b}$$

$n_f = \sqrt{\varepsilon_{rg} + \sigma_g/(j\omega\varepsilon_0)}$ is the complex reflection coefficient. Then, for studying the environment of transmitted electric field in soil and the variation characteristics related to ground parameters and depth, the following calculation and analysis are carried out in time domain and frequency domain, respectively. We adopt an incident field with time-domain amplitude expression being $E_0(t) = 65000 \times (e^{-t\times 4\times 10^7} - e^{-t\times 6\times 10^8})$ V/m.
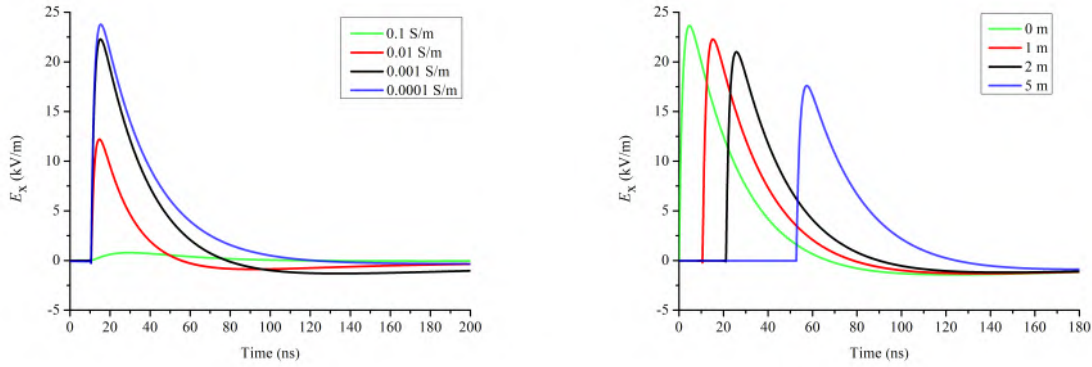
(a) Different ground conductivities (h=1 m)   (b) Different depths ($\sigma_g = 0.001$ S/m)

Figure 4.3 Time-domain waveform of underground transmitted electric field for different ground conductivities and depths

Firstly, the time-domain waveforms of electric field for different values of ground conductivity σ_g at a depth of 1 m are calculated and shown in Figure 4.3(a); Then, when $\sigma_g = 0.001$ S/m, the time-domain waveforms of electric field at different depths are depicted in Figure 4.3(b). The vertical polarized waves with $\psi = 90°$ and $\phi = 0°$ are used in this section to obtain the maximum electric field. It can be seen from Figure 4.3(a) that with the soil conductivity increases, the peak value of the transmitted electric field decreases, the wave-front slows down and the pulse-width becomes wider. These results indicate that the transmission component of electric field in soil decays with the increase of soil conductivity, especially the high-frequency component of electric field decays faster. Particularly, when the ground is perfectly conducting, the electric field at the air-earth interface will be reflected completely and not transmit into the soil. According to Figure 4.3(b), with the increase of the depth, the amplitude attenuation of transmitted electric field increases, but the waveform is broadly stable.

The amplitude spectrum and cumulative energy flow spectrum of horizontal component

of transmitted electric field corresponding to different ground conductivities are studied respectively in the frequency domain, and their characteristics are also analyzed. By Paswal's theorem, the energy spectrum defined by $S(f) = 2|E(f)|^2/Z$ can describe the change of energy flow with frequency, and Z is the wave impedance in earth. Hence, the normalized cumulative energy flow of the electric field transmitted into the soil can be expressed as

$$W = W_f/W_t \tag{4-21a}$$

$$W_f = \int_0^f S df \tag{4-21b}$$

$$W_t = \int_0^{+\infty} S df \tag{4-21c}$$

Figure 4.4 and Figure 4.5 show the amplitude spectrum of transmitted electric field, corresponding to different soil conductivities and depths, as well as the curve of normalized cumulative energy flow changing with frequency. For comparison, the spectrum and the cumulative energy flow of incident field in free space ($E_{incident}$) are also shown in figures.
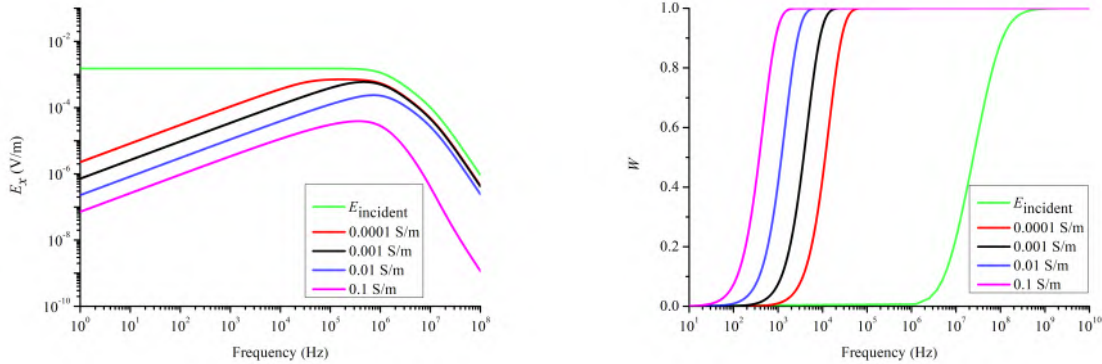
(a) Amplitude spectrum of electric field (h=1 m) (b) Normalized cumulative energy flow of electric field (h=1 m)

Figure 4.4   Amplitude spectrum and normalized cumulative energy flow of transmitted electric field for different ground conductivities

The amplitude spectrum in Figure 4.4(a) and Figure 4.5(a) show that the amplitude of transmitted electric field is smaller than that of incident electric field, and the bandwidth becomes narrow. Furthermore, with the increase of soil conductivity, the amplitude and bandwidth decay faster, while the depth has a small impact on the amplitude and bandwidth. As we know, 96 % energy of the incident electric field distributes in the range of 100 kHz-100 MHz. Accordingly, it can be seen from the cumulative energy flow spectrum in Figure 4.4(b) and Figure 4.5(b) that, compared with the incident electric field waveform, with the increase of the soil conductivity and depth, the main frequency range of the energy of transmitted electric

field becomes narrow and the frequency value decreases.
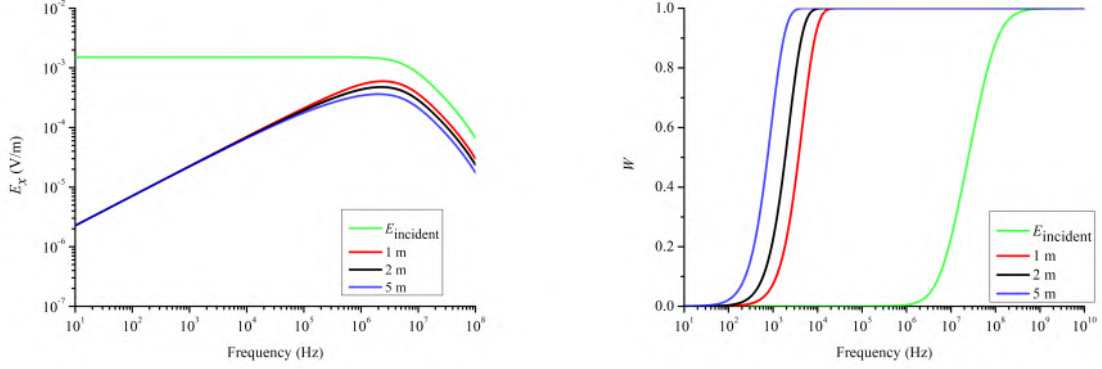
(a) Amplitude spectrum of electric field ($\sigma_g = 0.001$ S/m)

(b) Normalized cumulative energy flow of electric field ($\sigma_g = 0.001$ S/m)

Figure 4.5 Amplitude frequency spectrum and normalized cumulative energy flow of transmitted electric field for different depths

4.1.3 The formulation of p.u.l parameters for buried cables

1) The p.u.l internal impedance matrix and internal admittance (potential coefficient) matrix

Consider the metallic sheath or shield in Figure 4.1 being a hollow conductor, Schelknoff gives a discussion on the surface and transfer impedances of hollow solid cylindrical shells[19, 142], and the expressions have been derived in the form of Bessel function. Wedepohl and Wilcox[143] have proposed a very simple approximation for surface and transfer impedances without any Bessel functions, as given in (4-22). They are valid only for $(r_{3j} - r_{2j}) / (r_{3j} + r_{2j}) <$ 1/8. The expression of Z_{c-outj} can be obtained just by substituting r_{3j} and r_{2j} in (4-22b) with r_{1j} and r_{0j}.

$$Z_{s-inj} \approx \frac{\sqrt{j\omega\mu_{2j}\sigma_{2j}}}{2\pi\sigma_{2j}r_{2j}} \coth\left(\sqrt{j\omega\mu_{2j}\sigma_{2j}}\left(r_{3j} - r_{2j}\right) - \frac{1}{2\pi\sigma_{2j}r_{2j}\left(r_{3j} + r_{2j}\right)}\right) \tag{4-22a}$$

$$Z_{s-outj} = \frac{\sqrt{j\omega\mu_{2j}\sigma_{2j}}}{2\pi\sigma_{2j}r_{3j}} \coth\left(\sqrt{j\omega\mu_{2j}\sigma_{2j}}\left(r_{3j} - r_{2j}\right) - \frac{1}{2\pi\sigma_{2j}r_{3j}\left(r_{3j} + r_{2j}\right)}\right) \tag{4-22b}$$

$$Z_{s-transferj} = \frac{\sqrt{j\omega\mu_{2j}\sigma_{2j}}}{\pi\sigma_{2j}\left(r_{3j} + r_{2j}\right)} \frac{1}{\sinh\left(\left(r_{3j} - r_{2j}\right)\sqrt{j\omega\mu_{2j}\sigma_{2j}}\right)} \tag{4-22c}$$

For the transfer admittance, we have known the contribution of it to the total response of a cable is very small. Hence, for practical problems involving solid shields, this term is usually neglected[43]. However, for cases of braided shield cables containing apertures, the contribution

of transfer admittance could be important.

Many practical cables are shielded by a flexible, woven braid made of conducting filaments, hence, the transfer impedance and admittance will not be the same as discussed above. Because of inhomogeneous construction of braided shields and the complexity external field penetrating into the braid, the most reliable method for determining transfer parameters is by measurement. In [127], Vance mentioned that there will be two components that contribute to the transfer impedance. One is due to the diffusion of electromagnetic energy across the shield's thickness, and the other is due to the penetration of the magnetic field through braid's apertures. So the transfer impedance for the braided shield can be expressed as[19]

$$Z_{s-transferj} = Z_d + j\omega L_{12} \tag{4-23a}$$

$$Z_d = r_{dc} \frac{2r_{bw}\sqrt{j\omega\mu_{2j}\sigma_{2j}}}{\sinh\left(2r_{bw}\sqrt{j\omega\mu_{2j}\sigma_{2j}}\right)} \tag{4-23b}$$

The leakage inductance term L_{12} represents the penetration or the leakage part of the total transfer impedance. The values of Z_d and L_{12} are mainly determined by shield geometries and braid parameters. The term r_{dc} is the dc resistance of shield, and r_{bw} is radius of the carrier wire with which the shield is formed. Associated formulas of terms in (4-23) can be found in [127].

The transfer admittance of the braided shield can be approximately given by[19]

$$Y_{s-transferj} = j\omega C_{transferj} \tag{4-24a}$$

$$C_{transferj} \approx C_{ins1j}C_{ins2j}S_{sj} \tag{4-24b}$$

C_{ins1j} is the p.u.l capacitance of the inner insulator, C_{ins2j} is the p.u.l capacitance of the outer insulator, and S_{sj} is an electrostatic shield leakage parameter described in [127].

2) The p.u.l ground impedance and ground admittance (potential coefficient) matrix

Several researchers have developed or modified formulae for ground impedance of buried cables. The characteristics and accuracy of these expressions or approximations have been analyzed in several literatures[33, 55, 56]. A simple and efficient logarithmic approximation proposed by Petrache et al.[33] is widely accepted in the literature for the evaluation of ground impedance within TL approximation. It neglects the wire depth, and may result in inaccuracies, especially in the low frequency range[144]. To overcome this, Theethayi et al. modified the expression into an empirical logarithmic-exponential one (LE for short)[55], which includes the wire depth, i.e.

$$Z_{gjk} = \frac{s\mu_0}{2\pi} \left\{ \ln\left[\frac{1 + \gamma_g y_{jk}}{\gamma_g y_{jk}}\right] + \left[\frac{2e^{-2h|\gamma_g|}}{4 + \gamma_g^2 y_{jk}^2}\right]\right\} \qquad (4\text{-}25)$$

where h is the average depth of j-th and k-th cable. For self-impedance, y_{jk} should be replaced by the outer radius and h by the depth of the corresponding cable.

For ground admittance, Vance[127] originally proposed that it can be related to the ground impedance through the propagation constant $\gamma_g = \sqrt{s\mu_0(\sigma_g + s\varepsilon_0\varepsilon_{rg})}$ in the ground, as follows

$$Y_g \cong \frac{\gamma_g^2}{Z_g} \qquad (4\text{-}26)$$

However, the above approximation is only for a single conductor. And, as pointed out by Vance, (4-26) is based on a large depth of burial, i.e. $h \gg \delta$, with $\delta = 1/\sqrt{\pi f \mu_0 \sigma_g}$ being the penetration depth in the soil. Hence, this condition cannot be satisfied in most practical cases of underground transmission systems.

In our research work, an analytic integral (AI for short) formulation of self and mutual ground impedance and admittance proposed by Papadopoulos et al.[138, 139] is regarded as a preferable choice. It is derived by a rigorous solution of the electromagnetic field equations and takes into account the topology and electromagnetic properties of all involved media. The expressions are

$$Z_{gjk} = \frac{s\mu_0}{2\pi} \int_0^{+\infty} F(\lambda)\cos(y_{jk}\lambda)\cdot d\lambda \qquad (4\text{-}27)$$

$$Y_{gjk} = sP_{gjk}^{-1} \qquad (4\text{-}28)$$

where

$$P_{gjk} = \frac{s}{2\pi(\sigma_g + s\varepsilon_0\varepsilon_{rg})} \times \int_0^{+\infty} [F(\lambda) + G(\lambda)]\cos(y_{jk}\lambda)\cdot d\lambda \qquad (4\text{-}29)$$

$$F(\lambda) = \frac{e^{-\alpha_1|h_j - h_k|} - e^{-\alpha_1(h_j + h_k)}}{\alpha_1} + \frac{2e^{-\alpha_1(h_j + h_k)}}{\alpha_1 + \alpha_0} \qquad (4\text{-}30)$$

$$G(\lambda) = \frac{2\alpha_1(\gamma_1^2 - \gamma_0^2)e^{-\alpha_1(h_j + h_k)}}{(\alpha_1 + \alpha_0)(\alpha_1\gamma_0^2 + \alpha_0\gamma_1^2)} \qquad (4\text{-}31)$$

$\alpha_k = \sqrt{\lambda^2 + \gamma_k^2 + k_x^2}$, $\gamma_1^2 = j\omega\mu_0(\sigma_g + j\omega\varepsilon_0\varepsilon_{rg})$, and $\gamma_0^2 = -\omega^2\mu_0\varepsilon_0$ for $k = 0$ and 1, λ is the integral variable. The self-impedance and admittance (potential coefficient) of the conductor j is derived by replacing the y_{jk} with the outer radius and h_k with h_j.

In other well-known earth-return formulae, the unknown propagation constant of involved

media γ_x is always set equal to zero under a common approximation. This may neglect the earth correction term for the admittance, and limit the validity of formulae in the high-frequency range. Hence, γ_x is assumed as $jk_x = j\omega\sqrt{\mu_0\varepsilon_0\varepsilon_{rg}}$ in (4-27)-(4-31) for higher frequencies. It is noteworthy that these analytical expressions are in the form of a semi-infinite integral, which needs to be calculated by using a complicated numerical integration technique[145]. In this dissertation, in order to simplify the calculation, we propose the following approximation:

$$\int_0^{+\infty} F(\lambda)\cos(y_{jk}\lambda)\cdot d\lambda \approx \ln\left[\frac{1+\sqrt{\gamma_g^2+k_x^2}y_{jk}}{\sqrt{\gamma_g^2+k_x^2}y_{jk}}\right] + \left[\frac{2e^{-(h_i+h_j)\sqrt{\gamma_g^2+k_x^2}}}{4+(\gamma_g^2+k_x^2)y_{jk}^2}\right] \tag{4-32}$$

This expression is proposed by analogy with Theethayi's expression of the ground impedance. Clearly, if k_x is set equal to zero, (4-27) is reduced to the corresponding formula of Sunde[128], and it has been proven that the empirical logarithmic-exponential expression in (4-25) is a valid approximation of Sunde's ground impedance[146]. Hence, (4-32) is obtained by replacing γ_g with $\sqrt{\gamma_g^2+k_x^2}$. Accordingly, the expressions (4-27) and (4-30) can be approximated as follows:

$$Z_{gjk} = \frac{s\mu_0}{2\pi}\left\{\ln\left[\frac{1+\sqrt{\gamma_g^2+k_x^2}y_{jk}}{\sqrt{\gamma_g^2+k_x^2}y_{jk}}\right] + \left[\frac{2e^{-(h_i+h_j)\sqrt{\gamma_g^2+k_x^2}}}{4+(\gamma_g^2+k_x^2)y_{jk}^2}\right]\right\} \tag{4-33}$$

$$P_{gjk} = \frac{s}{2\pi(\sigma_g+s\varepsilon_0\varepsilon_{rg})} \times \left\{\begin{array}{l} \ln\left[\frac{1+\sqrt{\gamma_g^2+k_x^2}y_{jk}}{\sqrt{\gamma_g^2+k_x^2}y_{jk}}\right] + \left[\frac{2e^{-(h_i+h_j)\sqrt{\gamma_g^2+k_x^2}}}{4+(\gamma_g^2+k_x^2)y_{jk}^2}\right] \\ + \int_0^{+\infty} G(\lambda)\cos(y_{jk}\lambda)\cdot d\lambda \end{array}\right\} \tag{4-34}$$

Though a semi-infinite integral is still present in (4-34), it can be evaluated directly by integral evaluation function in MATLAB instead of numerical integration. Therefore, adopting the proposed expressions (4-33) and (4-34) largely improves the efficiency of the parameter evaluation procedure.

Figure 4.6 presents a comparison between various formulae for an insulated cable with outer diameter being 1.2 cm, buried at a depth of 1 m. Two different values of σ_g, namely, 0.01 S/m and 0.001 S/m and of the ground relative permittivity ε_{rg}, namely 10 and 5 are considered. In addition, the root-mean-square (RMS) error is calculated and compared to evaluate approximations numerically (AI expressions proposed by Papadopoulos et al. are considered as the reference). The RMS error is defined as $\sigma = \sqrt{(E_1^2 + E_2^2 + \cdots E_N^2)/N}$, N being the number of frequency samples and E_m ($m = 1, 2, \ldots N$) being the error of two formulae at the m-th frequency point.

Figure 4.6 shows that the proposed approximation and the AI expression proposed by Papadopoulos et al. agree very well for both ground impedance and admittance in the considered
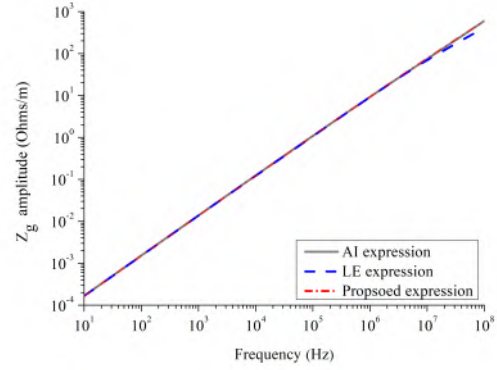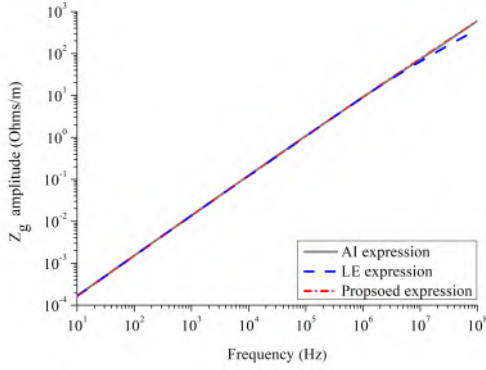
(a) Ground impedance ($\sigma_g = 0.001$ S/m, $\varepsilon_{rg} = 10$)   (b) Ground impedance ($\sigma_g = 0.001$ S/m, $\varepsilon_{rg} = 5$)
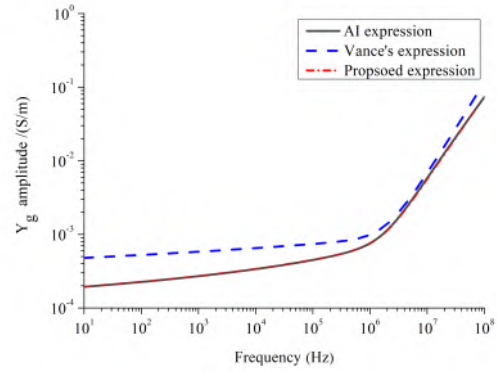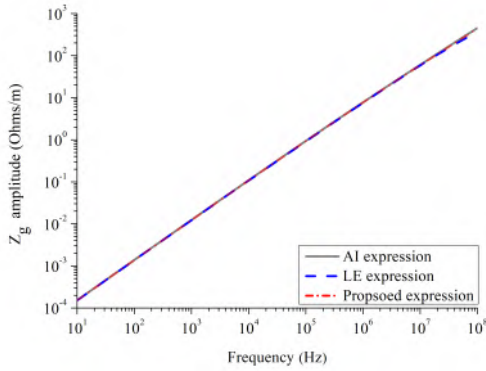
(c) Ground impedance ($\sigma_g = 0.01$ S/m, $\varepsilon_{rg} = 10$)   (d) Ground admittance ($\sigma_g = 0.001$ S/m, $\varepsilon_{rg} = 10$)
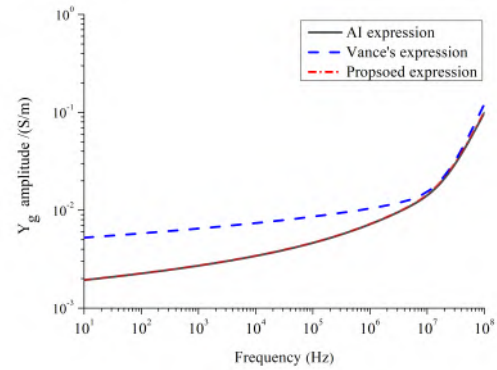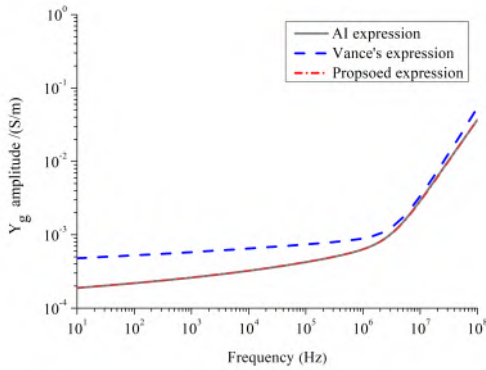
(e) Ground admittance ($\sigma_g = 0.001$ S/m, $\varepsilon_{rg} = 5$)   (f) Ground admittance ($\sigma_g = 0.01$ S/m, $\varepsilon_{rg} = 10$)

Figure 4.6 Comparison between different formulae for ground impedance and admittance

frequency range, while there are discrepancies in the amplitude of ground admittance obtained by (4-25) and (4-26) with other two expressions, which is mainly due to the approximations in the approach of [55] and [127]. From Table 4.1, we could see RMS errors of proposed approximations (4-32)-(4-34) for both ground impedance and admittance are far less than those of (4-25) and (4-26). Table 4.2 shows that the calculation efficiency of proposed approximations

Table 4.1 The RMS errors of different expressions for ground impedance and admittance

Approximations		$\sigma_g = 0.001$ S/m		$\sigma_g = 0.01$ S/m
		$\varepsilon_{rg} = 10$	$\varepsilon_{rg} = 5$	$\varepsilon_{rg} = 10$
Proposed	Z_g	2.2907	2.2907	2.7750
	Y_g	$2.1485e-4$	$7.9626e-5$	$7.9626e-5$
LE	Z_g	35.5132	29.2479	12.5798
	Y_g	0.0064	0.0024	0.0045

Table 4.2 The comparison of simulation times for different expressions

Approximations	$\sigma_g = 0.001$ S/m		$\sigma_g = 0.01$ S/m
	$\varepsilon_{rg} = 10$	$\varepsilon_{rg} = 5$	
Proposed (s)	8.782	8.243	7.605
AI (s)	349.680	345.550	344.033

is significantly improved compared with that of the AI expression on the same computing platform. The impact of above different expressions on transient responses of underground cables will be compared and discussed later.

4.1.4 Generation of the time-domain macromodel

In order to generate the macromodel for buried cables to incident field coupling, one assumption is made firstly for the sake of simplicity: due to the good shielding approximation, the energy transferred from the inner system to the outer system through the shield/sheath is neglected, that is, Z_{21} in (4-4b) and Y_{21} in (4-5b) become 0 while Z_{12} and Y_{12} remain unchanged. According to equations in (4-3), we figured out that the voltage and current of the outer transmission system are induced by primary distributed voltage and current sources V_{s2} and I_{s2}, but independent of the inner voltage and current; the response of inner loop are excited by coupling of outer loop through transfer impedance and admittance. Hence, in the following part, the macromodeling approach of field coupling to buried cables will be presented, for outer and inner transmission systems, respectively.

1) Outer system's model

Rewriting the TL equations for outer system's voltages and currents of n buried cables as

$$\frac{d}{dx}\begin{bmatrix} \mathbf{V}_2(x,s) \\ \mathbf{I}_2(x,s) \end{bmatrix} + \begin{bmatrix} \mathbf{0} & \mathbf{Z}_2(s) \\ \mathbf{Y}_2(s) & \mathbf{0} \end{bmatrix}\begin{bmatrix} \mathbf{V}_2(x,s) \\ \mathbf{I}_2(x,s) \end{bmatrix} = \begin{bmatrix} \mathbf{V}_{s2}(x,s) \\ \mathbf{I}_{s2}(x,s) \end{bmatrix} \tag{4-35}$$

in which

$$\mathbf{V}_2 = [V_{12}, \cdots, V_{j2}, \cdots, V_{n2}]_{1\times n}^T \tag{4-36a}$$

$$\mathbf{I}_2 = [I_{12}, \cdots, I_{j2}, \cdots, I_{n2}]_{1\times n}^T \tag{4-36b}$$

$$\mathbf{V}_{s2} = \left[E_x^{tran}(s,x,y_1,z_1), \cdots, E_x^{tran}(s,x,y_j,z_j), \cdots, E_x^{tran}(s,x,y_n,z_n)\right]_{1\times n}^T \tag{4-36c}$$

$$\mathbf{I}_{s2} = [0, \cdots, 0, \cdots, 0]_{1\times n}^T \tag{4-36d}$$

And the p.u.l impedance matrix $\mathbf{Z}_2(s)$ and admittance matrix $\mathbf{Y}_2(s)$ are defined as

$$\mathbf{Z}_2(s) = \begin{bmatrix} Z_{ins21} & 0 & \cdots & 0 \\ 0 & Z_{ins22} & \cdots & 0 \\ \vdots & \vdots & \ddots & \vdots \\ 0 & 0 & \cdots & Z_{ins2n} \end{bmatrix}_{n\times n} + \begin{bmatrix} Z_{g11} & Z_{g12} & \cdots & Z_{g1n} \\ Z_{g21} & Z_{g22} & \cdots & Z_{g2n} \\ \vdots & \vdots & \ddots & \vdots \\ Z_{gn1} & Z_{gn2} & \cdots & Z_{gnn} \end{bmatrix}_{n\times n} \tag{4-37}$$

$$\mathbf{Y}_2 = s\mathbf{P}_2^{-1} \tag{4-38a}$$

$$\mathbf{P}_2 = \begin{bmatrix} P_{ins21} & 0 & \cdots & 0 \\ 0 & P_{ins22} & \cdots & 0 \\ \vdots & \vdots & \ddots & \vdots \\ 0 & 0 & \cdots & P_{ins2n} \end{bmatrix}_{n\times n} + \begin{bmatrix} P_{g11} & P_{g12} & \cdots & P_{g1n} \\ P_{g21} & P_{g22} & \cdots & P_{g2n} \\ \vdots & \vdots & \ddots & \vdots \\ P_{gn1} & P_{gn2} & \cdots & P_{gnn} \end{bmatrix}_{n\times n} \tag{4-38b}$$

Similar to overhead TLs, the characteristic impedance (admittance) and propagation operator for the outer transmission system of buried cables can also be defined as

$$\mathbf{Z_{C2}} = \sqrt{\mathbf{Z}_2\mathbf{Y}_2}\mathbf{Y}_2^{-1} = (\sqrt{\mathbf{Z}_2\mathbf{Y}_2})^{-1}\mathbf{Z}_2; \quad \mathbf{Y_{C2}} = \mathbf{Z_{C2}^{-1}}; \quad \mathbf{H}_2(s) = e^{-\sqrt{\mathbf{Z}_2\mathbf{Y}_2}l} \tag{4-39}$$

l is the length of cables. Then making an analogy with cases in chapter 3 of overhead MTLs to field coupling, a macromodel for (4-35) can easily be realized in terms of an equivalent circuit, like Figure 3.7, just by substituting all parameters of overhead lines and external field with those of buried cables and transmitted field. And beyond this, in order to prepare for deriving the macromodel for the inner transmission system, we express the outer system's voltage $\mathbf{V}_2$ and current $\mathbf{V}_2$ as

$$\mathbf{V}_2(x) = \frac{1}{2}\left[\mathbf{V}_{F2}(0)e^{-\sqrt{\mathbf{Z}_2\mathbf{Y}_2}x} + \mathbf{V}_{B2}(l)e^{\sqrt{\mathbf{Z}_2\mathbf{Y}_2}(x-l)} + \mathbf{V}_{sF2}(x) + \mathbf{V}_{sB2}(x)\right] \tag{4-40a}$$

$$\mathbf{I}_2(x) = \frac{1}{2}\mathbf{Z_{C2}^{-1}}\left[\mathbf{V}_{F2}(0)e^{-\sqrt{\mathbf{Z}_2\mathbf{Y}_2}x} - \mathbf{V}_{B2}(l)e^{\sqrt{\mathbf{Z}_2\mathbf{Y}_2}(x-l)} + \mathbf{V}_{sF2}(x) - \mathbf{V}_{sB2}(x)\right] \tag{4-40b}$$

in which $\mathbf{V}_{F2}(0)$ is the forward voltage wave at $x = 0$ and $\mathbf{V}_{B2}(l)$ is the backward voltage wave at $x = l$. They are given by

$$\mathbf{V}_{F2}(0) = \mathbf{V}_2(0) + \mathbf{Z}_{\mathbf{C2}}\mathbf{I}_2\,(0) \tag{4-41a}$$

$$\mathbf{V}_{B2}(l) = \mathbf{V}_2(l) - \mathbf{Z}_{\mathbf{C2}}\mathbf{I}_2\,(l) \tag{4-41b}$$

$\mathbf{V}_{sF2}(x)$ and $\mathbf{V}_{sB2}(x)$ are total effects of the distributed sources at x, which are expressed as

$$\mathbf{V}_{sF2}(x) = \int_0^x \left[\mathbf{V}_{s2}(\tau) + \mathbf{Z}_{\mathbf{C2}}\mathbf{I}_{s2}(\tau)\right] e^{-\sqrt{\mathbf{Z}_2\mathbf{Y}_2}(x-\tau)} d\tau \tag{4-42a}$$

$$\mathbf{V}_{sB2}(x) = \int_l^x \left[\mathbf{V}_{s2}(\tau) - \mathbf{Z}_{\mathbf{C2}}\mathbf{I}_{s2}(\tau)\right] e^{\sqrt{\mathbf{Z}_2\mathbf{Y}_2}(x-\tau)} d\tau \tag{4-42b}$$

2) Inner system's model

As mentioned before, the voltage and current of the inner loop are only excited by outer loop's coupling of the same cable, so for the sake of simplicity, the derivation of the inner system's model will be presented for only one cable, without considering the coupling of other cables. Hence, the TL equations for an inner system can be written as

$$\frac{d}{dx}\begin{bmatrix} V_1(x,s) \\ I_1(x,s) \end{bmatrix} + \begin{bmatrix} 0 & Z_1(s) \\ Y_1(s) & 0 \end{bmatrix}\begin{bmatrix} V_1(x,s) \\ I_1(x,s) \end{bmatrix} = \begin{bmatrix} V_{s1}(x,s) \\ I_{s1}(x,s) \end{bmatrix} \tag{4-43}$$

in which

$$Z_1(s) = Z_{c-out} + Z_{ins1} + Z_{s-in} \tag{4-44a}$$

$$Y_1(s) = sP_1^{-1} \tag{4-44b}$$

$$P_1 = P_{ins1} \tag{4-44c}$$

$$V_{s1}(x,s) = Z_{s-transfer}I_2(x,s) \tag{4-44d}$$

$$I_{s1}(x,s) = -Y_{s-transfer}V_2(x,s) \tag{4-44e}$$

Hence, according to (3-39), the inner system can also be equivalent to a two-port circuit model characterized by equations as

$$V_1(l,s) + Z_{c1}(s)I_1(l,s) = H_1(s)\left[V_1(0,s) + Z_{c1}(s)I_1(0,s)\right] + V_{sF1}(l,s) \tag{4-45a}$$

$$V_1(0,s) - Z_{c1}(s)I_1(0,s) = H_1(s)\left[V_1(l,s) - Z_{c1}(s)I_1(l,s)\right] + V_{sB1}(0,s) \tag{4-45b}$$

where $Z_{c1} = \sqrt{Z_1/Y_1}$ and $H_1(s) = e^{-\sqrt{Z_1Y_1}l}$ are the characteristic impedance and propagation operator of the inner system, respectively. $V_{sF1}(l,s)$ and $V_{sB1}(0,s)$ are distributed sources

related to the voltage and current of the outer system. Obviously, there is no other difficulties to model the inner system except for obtaining appropriate representation of $V_{sF1}(l, s)$ and $V_{sB1}(0, s)$. Here the expressions of them are given by

$$V_{sF1}(l, s) = \int_0^l e^{-\sqrt{Z_1 Y_1}(l-\tau)} \left[V_{s1}(\tau) + Z_{c1} I_{s1}(\tau) \right] d\tau \qquad (4\text{-}46\text{a})$$

$$V_{sB1}(0, s) = -\int_0^l e^{-\sqrt{Z_1 Y_1}\tau} \left[V_{s1}(\tau) - Z_{c1} I_{s1}(\tau) \right] d\tau \qquad (4\text{-}46\text{b})$$

where

$$\begin{aligned}
&V_{s1}(\tau) + Z_{c1} I_{s1}(\tau) = Z_{s-transfer} I_2(\tau) - Z_{c1} Y_{s-transfer} V_2(\tau) \\
&= Z_{s-transfer} \times \frac{1}{2Z_{c2}} \left[V_{F2}(0) e^{-\sqrt{Z_2 Y_2}\tau} - V_{B2}(l) e^{\sqrt{Z_2 Y_2}(\tau-l)} + V_{sF2}(\tau) - V_{sB2}(\tau) \right] \\
&- Z_{c1} \times \frac{Y_{s-transfer}}{2} \left[V_{F2}(0) e^{-\sqrt{Z_2 Y_2}\tau} + V_{B2}(l) e^{\sqrt{Z_2 Y_2}(\tau-l)} + V_{sF2}(\tau) + V_{sB2}(\tau) \right]
\end{aligned} \qquad (4\text{-}47\text{a})$$

$$\begin{aligned}
&V_{s1}(\tau) - Z_{c1} I_{s1}(\tau) = Z_{s-transfer} I_2(\tau) + Z_{c1} Y_{s-transfer} V_2(\tau) \\
&= Z_{s-transfer} \times \frac{1}{2Z_{c2}} \left[V_{F2}(0) e^{-\sqrt{Z_2 Y_2}\tau} - V_{B2}(l) e^{\sqrt{Z_2 Y_2}(\tau-l)} + V_{sF2}(\tau) - V_{sB2}(\tau) \right] \\
&+ Z_{c1} \times \frac{Y_{s-transfer}}{2} \left[V_{F2}(0) e^{-\sqrt{Z_2 Y_2}\tau} + V_{B2}(l) e^{\sqrt{Z_2 Y_2}(\tau-l)} + V_{sF2}(\tau) + V_{sB2}(\tau) \right]
\end{aligned} \qquad (4\text{-}47\text{b})$$

Hence, the $V_{sF1}(l, s)$ and $V_{sB1}(l, s)$ can be written as

$$V_{sF1}(l, s) = \frac{Z_{s-transfer} - Z_{c1} Y_{s-transfer} Z_{c2}}{2Z_{c2}} E_{sF11} - \frac{Z_{s-transfer} + Z_{c1} Y_{s-transfer} Z_{c2}}{2Z_{c2}} E_{sF12}$$
$$(4\text{-}48\text{a})$$

$$V_{sB1}(l, s) = -\frac{Z_{s-transfer} + Z_{c1} Y_{s-transfer} Z_{c2}}{2Z_{c2}} E_{sB11} + \frac{Z_{s-transfer} - Z_{c1} Y_{s-transfer} Z_{c2}}{2Z_{c2}} E_{sB12}$$
$$(4\text{-}48\text{b})$$

where

$$E_{sF11} = \int_0^l V_{F2}(0) e^{-\sqrt{Z_1 Y_1}(l-\tau)} e^{-\sqrt{Z_2 Y_2}\tau} d\tau + \int_0^l V_{sF2}(\tau) e^{-\sqrt{Z_1 Y_1}(l-\tau)} d\tau \qquad (4\text{-}49\text{a})$$

$$E_{sF12} = \int_0^l V_{B2}(l) e^{-\sqrt{Z_1 Y_1}(l-\tau)} e^{-\sqrt{Z_2 Y_2}(l-\tau)} d\tau + \int_0^l V_{sB2}(\tau) e^{-\sqrt{Z_1 Y_1}(l-\tau)} d\tau \qquad (4\text{-}49\text{b})$$

$$E_{sB11} = \int_0^l V_{F2}(0) e^{-\sqrt{Z_1 Y_1}\tau} e^{-\sqrt{Z_2 Y_2}\tau} d\tau + \int_0^l V_{sF2}(\tau) e^{-\sqrt{Z_1 Y_1}\tau} d\tau \qquad (4\text{-}49\text{c})$$

$$E_{sB12} = \int_0^l V_{B2}(l) e^{-\sqrt{Z_1 Y_1}\tau} e^{-\sqrt{Z_2 Y_2}(l-\tau)} d\tau + \int_0^l V_{sB2}(\tau) e^{-\sqrt{Z_1 Y_1}\tau} d\tau \qquad (4\text{-}49\text{d})$$

For simplicity, we adopted A_1 and A_2 to denote two expressions as

$$A_1 = -\frac{Z_{s-transfer} + Z_{c1} Y_{s-transfer} Z_{c2}}{2Z_{c2}} \qquad (4\text{-}50\text{a})$$

$$A_2 = \frac{Z_{s-transfer} - Z_{c1}Y_{s-transfer}Z_{c2}}{2Z_{c2}} \tag{4-50b}$$

Converting the equations in (4-47) into time domain, we have

$$V_1(l,t) + z_{c1}(t) * I_1(l,t) = h_1(t) * [V_1(0,t) + z_{c1}(t) * I_1(0,t)] + V_{sF1}(l,t) \tag{4-51a}$$

$$V_1(0,s) - z_{c1}(t) * I_1(0,s) = h_1(t) * [V_1(l,s) - z_{c1}(t) * I_1(l,t)] + V_{sB1}(0,t) \tag{4-51b}$$

$$V_{sF1}(l,t) = A_2(t) * E_{sF11}(t) + A_1(t) * E_{sF12}(t) \tag{4-52a}$$

$$V_{sB1}(0,t) = A_1(t) * E_{sB11}(t) + A_2(t) * E_{sB12}(t) \tag{4-52b}$$

where the correspondence with the Laplace variables of (4-47) is listed below:

$$V_1(s) \Leftrightarrow V_1(t); \quad I_1(s) \Leftrightarrow I_1(t); \quad Z_{c1}(s) \Leftrightarrow z_{c1}(t); \quad H_1(s) \Leftrightarrow h_1(t) \tag{4-53a}$$

$$A_i(s) \Leftrightarrow A_i(t); \quad E_{sF1i}(s) \Leftrightarrow E_{sF1i}(t); \quad E_{sB1i}(s) \Leftrightarrow E_{sB1i}(t); \quad i = 1,2 \tag{4-53b}$$

The convolution operator in (4-51) and (4-52) can be realized by frequency-domain devices of ABM library during transient analysis. Therefore, the solutions to $E_{sF1i}(t)$ and $E_{sB1i}(t)$ ($i = 1, 2$) is the key point of the modeling here. In a bid to become more organized, we break these four terms into two categories: one is related to contributions of outer system's terminal voltage and current: $V_{F2}(0)$ and $V_{B2}(l)$; another one is contributed by excitation field on the outer system: V_{sF2} and V_{sB2}. Denote F_{ti} ($i = 1, \cdots, 4$) as

$$F_{t1} = \int_0^l V_{F2}(0)e^{-\sqrt{Z_1Y_1}(l-\tau)}e^{-\sqrt{Z_2Y_2}\tau}d\tau = B_1(s) \times V_{F2}(0) \tag{4-54a}$$

$$F_{t2} = \int_0^l V_{B2}(l)e^{-\sqrt{Z_1Y_1}(l-\tau)}e^{-\sqrt{Z_2Y_2}(l-\tau)}d\tau = B_2(s) \times V_{B2}(l) \tag{4-54b}$$

$$F_{t3} = \int_0^l V_{F2}(0)e^{-\sqrt{Z_1Y_1}\tau}e^{-\sqrt{Z_2Y_2}\tau}d\tau = B_2(s) \times V_{F2}(0) \tag{4-54c}$$

$$F_{t4} = \int_0^l V_{B2}(l)e^{-\sqrt{Z_1Y_1}\tau}e^{-\sqrt{Z_2Y_2}(l-\tau)}d\tau = B_1(s) \times V_{B2}(l) \tag{4-54d}$$

where

$$B_1(s) = \frac{e^{-\sqrt{Z_2Y_2}l} - e^{-\sqrt{Z_1Y_1}l}}{\sqrt{Z_1Y_1} - \sqrt{Z_2Y_2}} \tag{4-55a}$$

$$B_2(s) = \frac{1 - e^{-(\sqrt{Z_2Y_2}+\sqrt{Z_1Y_1})l}}{\sqrt{Z_1Y_1} + \sqrt{Z_2Y_2}} \tag{4-55b}$$

The distributed sources $V_{s1}(x,s)$ and $I_{s1}(x,s)$ of the outer system for the transmitted elec-

trical field can be expressed as

$$V_{s2}(x,s) = E_x^{tran}(s,x,y,z)$$
$$= E_0(s) \left[T_v \cos\alpha \sin\psi_t \cos\phi + T_h \sin\alpha \sin\phi\right] e^{\gamma_g y \cos\psi \sin\phi} e^{\gamma_g z \sin\psi_t} \qquad \text{(4-56a)}$$
$$\times e^{-\gamma_g x \cos\psi_t \cos\phi} = C(s)e^{-\gamma x}$$

$$I_{s2}(x,s) = 0 \qquad \text{(4-56b)}$$

where

$$C(s) = E_0(s) \left[T_v \cos\alpha \sin\psi_t \cos\phi + T_h \sin\alpha \sin\phi\right] e^{\gamma_g y \cos\psi \sin\phi} e^{\gamma_g z \sin\psi_t} \qquad \text{(4-57a)}$$

$$\gamma = \gamma_g \cos\psi_t \cos\phi \qquad \text{(4-57b)}$$

Substituting (4-56) into (4-42), and calculating integrals yields

$$V_{sF2}(x) = \int_0^x \left[V_{s2}(\tau) + Z_{c2} I_{s2}(\tau)\right] e^{-\sqrt{Z_2 Y_2}(x-\tau)} d\tau$$
$$= C(s) \frac{1}{\sqrt{Z_2 Y_2} - \gamma} \left(e^{-\gamma x} - e^{-\sqrt{Z_2 Y_2} x}\right) \qquad \text{(4-58a)}$$

$$V_{sB2}(x) = \int_l^x \left[V_{s2}(\tau) - Z_{c2} I_{s2}(\tau)\right] e^{\sqrt{Z_2 Y_2}(x-\tau)} d\tau$$
$$= C(s) \frac{e^{\sqrt{Z_2 Y_2} x}}{\gamma + \sqrt{Z_2 Y_2}} \left(e^{-(\gamma+\sqrt{Z_2 Y_2})l} - e^{-(\gamma+\sqrt{Z_2 Y_2})x}\right) \qquad \text{(4-58b)}$$

Then, denote F_{si} $(i = 1, \cdots, 4)$ as

$$F_{s1} = \int_0^l V_{sF2}(\tau) e^{-\sqrt{Z_1 Y_1}(l-\tau)} d\tau = C(s) \frac{1}{\sqrt{Z_2 Y_2} - \gamma} \left(\frac{e^{-\gamma l} - e^{-\sqrt{Z_1 Y_1} l}}{\sqrt{Z_1 Y_1} - \gamma} - \frac{e^{-\sqrt{Z_2 Y_2} l} - e^{-\sqrt{Z_1 Y_1} l}}{\sqrt{Z_1 Y_1} - \sqrt{Z_2 Y_2}}\right)$$

$$\text{(4-59a)}$$

$$F_{s2} = \int_0^l V_{sB2}(\tau) e^{-\sqrt{Z_1 Y_1}(l-\tau)} d\tau = C(s) \frac{1}{\sqrt{Z_2 Y_2} + \gamma} \left(\frac{e^{-\gamma l} - e^{-(\sqrt{Z_1 Y_1} + \sqrt{Z_2 Y_2} + \gamma)l}}{\sqrt{Z_1 Y_1} + \sqrt{Z_2 Y_2}} - \frac{e^{-\gamma l} - e^{-\sqrt{Z_1 Y_1} l}}{\sqrt{Z_1 Y_1} - \gamma}\right)$$

$$\text{(4-59b)}$$

$$F_{s3} = \int_0^l V_{sF2}(\tau) e^{-\sqrt{Z_1 Y_1} \tau} d\tau = C(s) \frac{1}{\sqrt{Z_2 Y_2} - \gamma} \left(\frac{1 - e^{-(\sqrt{Z_1 Y_1} + \gamma)l}}{\sqrt{Z_1 Y_1} + \gamma} - \frac{1 - e^{-(\sqrt{Z_1 Y_1} + \sqrt{Z_2 Y_2})l}}{\sqrt{Z_1 Y_1} + \sqrt{Z_2 Y_2}}\right)$$

$$\text{(4-59c)}$$

$$F_{s4} = \int_0^l V_{sB2}(\tau) e^{-\sqrt{Z_1 Y_1} \tau} d\tau = C(s) \frac{1}{\sqrt{Z_2 Y_2} + \gamma} \left(\frac{e^{-(\sqrt{Z_1 Y_1} + \gamma)l} - e^{-(\sqrt{Z_2 Y_2} + \gamma)l}}{\sqrt{Z_2 Y_2} - \sqrt{Z_1 Y_1}} + \frac{e^{-(\gamma + \sqrt{Z_1 Y_1})l} - 1}{\sqrt{Z_1 Y_1} + \gamma}\right)$$

$$\text{(4-59d)}$$

Hence, the time-domain expressions of $E_{sF1i}(t)$ and $E_{sB1i}(t)$ $(i = 1, 2)$ can be written as

$$E_{sF11}(t) = F_{t1}(t) + F_{s1}(t) = B_1(t) * V_{F2}(0,t) + F_{s1}(t) \qquad \text{(4-60a)}$$

$$E_{sF12}(t) = F_{t2}(t) + F_{s2}(t) = B_2(t) * V_{B2}(l,t) + F_{s2}(t) \qquad \text{(4-60b)}$$

$$E_{sB11}(t) = F_{t3}(t) + F_{s3}(t) = B_2(t) * V_{F2}(0,t) + F_{s3}(t) \qquad \text{(4-60c)}$$

$$E_{sB12}(t) = F_{t4}(t) + F_{s4}(t) = B_1(t) * V_{B2}(l,t) + F_{s4}(t) \qquad \text{(4-60d)}$$

3) SPICE equivalent circuit

The SPICE circuit model for the inner transmission system of cables can be established according to (4-51)-(4-52), and (4-60), as shown in Figure 4.7.
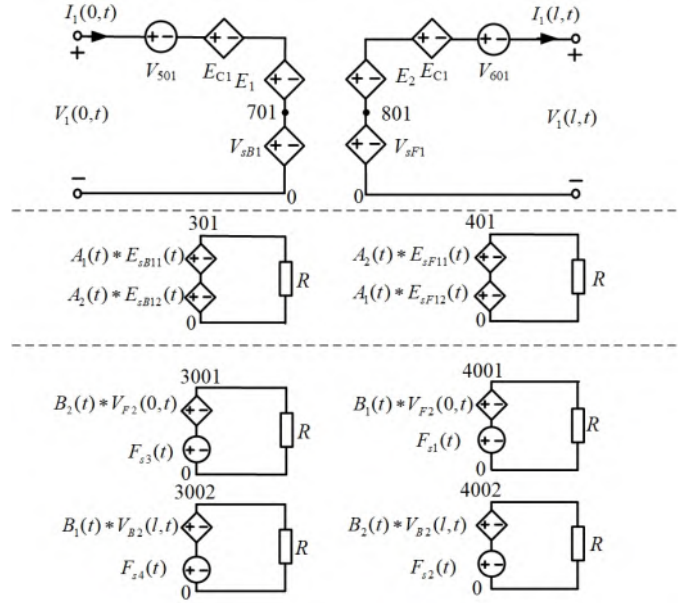
Figure 4.7 The equivalent circuit of macromodel for an inner transmission system of the cable

The voltage controlled voltage sources V_{sB1} and V_{sF1} between circuit nodes $(701,0)$ and $(801,0)$ are given by

$$V_{sB1}=V(301,0); \quad V_{sF1}=V(401,0) \qquad \text{(4-61)}$$

Obviously, the voltages between $(301,0)$ and $(401,0)$ are both determined by combination of two controlled voltage sources, which calculate the convolutions in time domain. Further, $E_{sF1i}(t)$ and $E_{sB1i}(t)$ $(i=1,2)$ can also be reresented by controlled voltage sources:

$$E_{sB11}(t) = V(3001,0) \qquad \text{(4-62a)}$$

$$E_{sB12}(t) = V(3002,0) \qquad \text{(4-62b)}$$

$$E_{sF11}(t) = V(4001,0) \qquad \text{(4-62c)}$$

$$E_{sF12}(t) = V(4002,0) \qquad \text{(4-62d)}$$

In addition, the controlled voltage sources E_{c1} and E_{c2} translate the convolution terms on the left side of (4-51):

$$E_{c1} = z_{c1}(t) * I_1(0, s) \tag{4-63a}$$

$$E_{c2} = z_{c1}(t) * I_1(l, t) \tag{4-63b}$$

The controlled voltage sources E_1 and E_2 correspond to the convolution terms on the right side of (4-51):

$$E_1 = h_1(t) * [V_1(l, s) - z_{c1}(t) * I_1(l, t)] \tag{4-64a}$$

$$E_2 = h_1(t) * [V_1(0, t) + z_{c1}(t) * I_1(0, t)] \tag{4-64b}$$

Except for controlled voltage sources V_{sB1} and V_{sF1}, all other controlled voltage sources realize convolution calculations in time domain by frequency-domain devices in ABM library of SPICE. It also should be noted that, all resistances R in the circuit are $1\ \Omega$, which are used to avoid floating nodes, and DC voltage sources V_{501} and V_{601} are used to pick up the currents at the ports.

4.2 Accuracy and efficiency validation by simulation

This section is firstly devoted to demonstrating the validity and efficiency of the proposed macromodel. For simplification, an example of field coupling to a buried insulated SC cable in [43] is investigated and the transient responses are compared with corresponding ones obtained by other numerical algorithms. At the same time, the impact of different earth return expressions on transient responses are considered in this example. Then, in order to validate the proposed macromodel of shielded cables, it is firstly used to study the incident field coupling to an RG-58 coaxial cable, which is usually adopted in communication systems, and the results are compared with those in the literature. Then, the transient responses of a buried RG-58 coaxial cable are calculated and analyzed. Because the overvoltage protection for metallic sheath layer of high-voltage power cables is a key point in practical engineering application, so several scenarios of underground power cables with different arrangements and sheath of cables terminating with nonlinear protective devices are finally analyzed adopting proposed macromodel. In the following part, the PSpice circuit simulation software is utilized to simulate all examples on a PC equipped with an INTEL i7 3.6-GHz CPU.
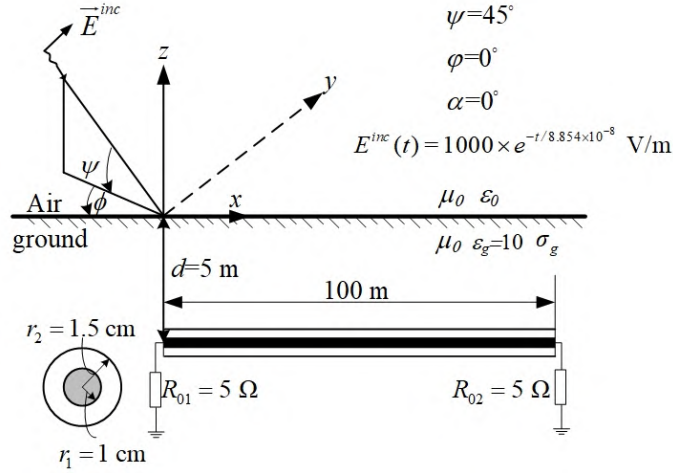
Figure 4.8 The geometry of transient plane wave coupling to a buried insulated cable loaded with grounding resistances

4.2.1 Example 1: the transient field coupling to an insulated buried cable

This example mainly focus on validating the proposed model for transient plane wave coupling to a buried cable terminated with linear loads. In addition, the impact of different earth return expressions on transient responses are also studied in this example. Figure 4.8 shows the geometry of an example of transient plane wave coupling to a l00-m long insulated buried cable in [43]. All parameters of cable, earth and incident field are all listed in it. The buried cable is analyzed when $\sigma_g = 0.01$ S/m, 0.01 S/m, 0.001 S/m and 0.0001 S/m, respectively. In this example, the proposed modeling algorithm is validated by comparing the induced current flowing through the far terminal grounding resistance simulated by both proposed model and FDTD method. Because the integral in AI formulation of ground impedance and admittance must be evaluated numerically, for fair comparison, the frequency-domain response table device of ABM, i.e. FREQ, is adopted in the macromodels for this example. The time resolution of input excited sources is 1.22×10^{-10} s and the length of transient analysis $TSTOP$ is 10 μs. Hence, according to the criteria proposed in Chapter 2, the frequency range f_c are chosen to be 100 MHz, with $NFFT$ taken to be 8192. The space (length) and time discretization Δx and Δt in FDTD simulation are set as 0.5 m and 16.67 ns, which satisfy the Courant condition. The results obtained using above two methods relevant to currents at the terminal end for different ground conductivities are shown in Figure 4.9.

As seen in Figure 4.9, the results are all in good agreement. Slight deviations between these curves could be ascribed to numerical errors inherent in the methods (including fitting errors, discretization of FDTD, etc.). The simulation times of the FDTD method for all cases are about 5 min, which highly depend on the line length and mesh size, while the proposed model runs in less than 10 s for all different ground conductivities, with little influence of
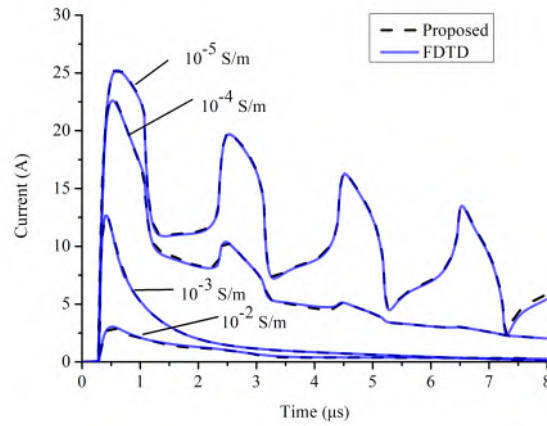
Figure 4.9 Induced currents at the far end of the buried cable for different σ_g. Comparison is presented between FDTD method (blue solid curves) and the proposed model (black dash curves)

the line length on the macromodel simulation[147]. The computation efficiency is thus greatly improved compared to the FDTD method. As an additional comment, we would like to point out the well-known fact that the intensity of transient electromagnetic field transmitted into the soil becomes stronger when the conductivity decreases. As a result, the electromagnetic energy coupling to buried conductors increases as well as the induced current on the wire. Hence, the results of this example validate the proposed method and confirm its credibility and efficiency in simulating field coupling to buried conductors.
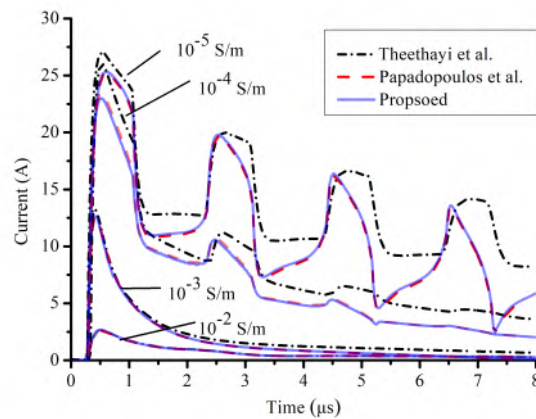
Figure 4.10 Comparison of induced currents at the far terminal grounding resistive load, using Theethayi's expressions (4-25)-(4-26) (black dash dot curves), Papadopoulos's expressions (4-27)-(4-31) (red dash dot curves), and proposed expressions in (4-32)-(4-34) (blue solid curves)

Then, the impact of three different earth return formulations on transient responses are considered in this case. Figure 4.10 illustrates the comparison of induced currents at the far end for four different ground conductivities using LE expressions in (4-25)-(4-26), AI expressions

in (4-27)-(4-31) and the proposed expressions in (4-32)-(4-34), respectively. Other conditions are the same as those shown in Figure 4.9. As can be observed from Figure 4.10, transient responses at the far end of the cable obtained using AI expressions and the proposed approximations have comparable results, which indicates the validity of the proposed expressions. In addition, the formulations (4-25)-(4-26) lead to discrepancies in transient responses. This finding can be explained by the restriction of Vance's admittance approximation, which apparently could not be satisfied in the frequency range of interest (≤ 10 MHz) for the arrangement of this example. And in particular, according to the definition of penetration depth, with the decrease of ground conductivity, the differences will become more significant. This inference has also been confirmed by the peak values and attenuation trend of waveforms in Figure 4.10. Hence, the AI expressions or the proposed approximation expressions are preferable choices for the evaluation of ground admittance in most of the transient problems of buried cables.

4.2.2 Example 2: the transient field coupling to a shielded cable

(a) Wire-to-shield voltage   (b) Shield-to-ground voltage
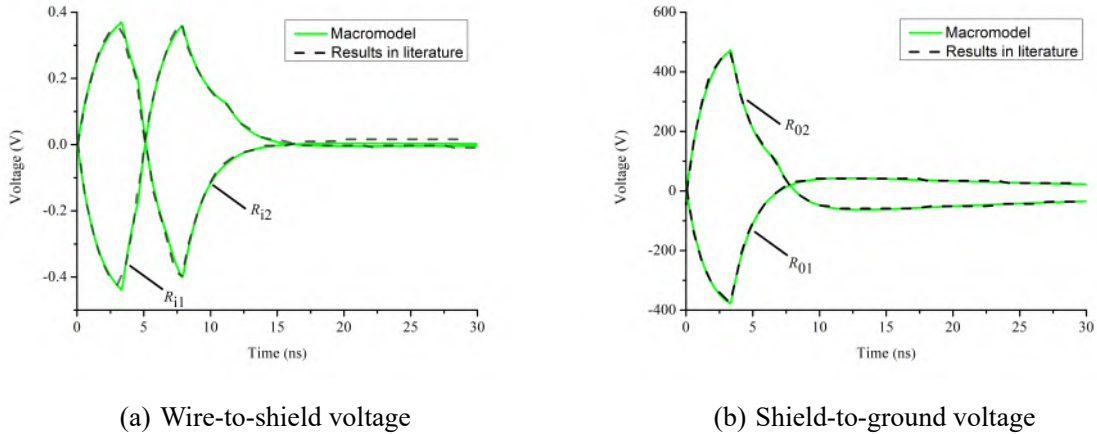
Figure 4.11 The voltage responses on the internal and external loads of the shielded cable

In this example，we firstly consider a numerical example of incident field coupling to an RG-58 coaxial cable in [148] to validate the proposed macromodel for shielded cables.

The cable is with height $h = 0.1$ cm, length $l = 1$ m. The outer radius of the shield layer r_3 is 1.52 mm, and the shield thickness is 0.127 mm. The relative permittivity ε_{ins1} of the internal dielectric filling is 1.85. The DC resistance r_{dc} is 14.2 mΩ/m, the aperture leakage inductance L_{12} is 1 nH/m, and the electrostatic shield leakage parameter S_s is 6.6×10^7 m/F. The terminal loads connecting the shield and the ground are $R_{01} = 100$ Ω and $R_{02} = 150$ Ω. The inner terminals are matched with $R_{i1} = 50$ Ω and $R_{i2} = 50$ Ω. The time-domain amplitude expression of the incident electircal field is $E_0(t) = 65 \times (e^{-t \times 4 \times 10^7} - e^{-t \times 6 \times 10^8})$ kV/m, with α=0°, ψ=90° and ϕ=0°.

The voltage responses on the loads R_{01}, R_{02}, R_{i1} and R_{i2} computed by the proposed
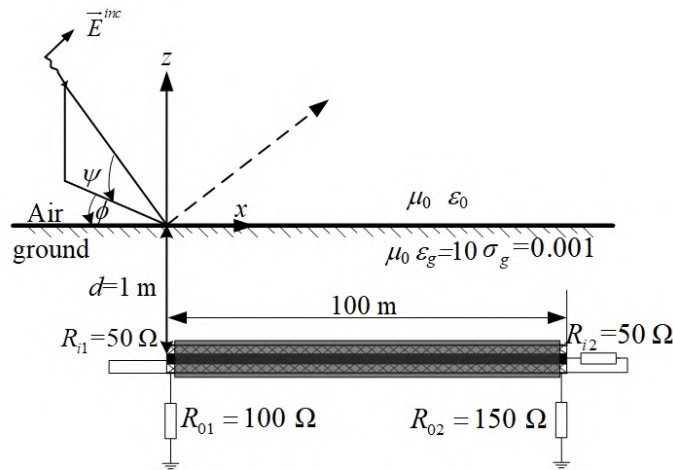
Figure 4.12 The geometry of transient plane wave coupling to a buried shielded cable
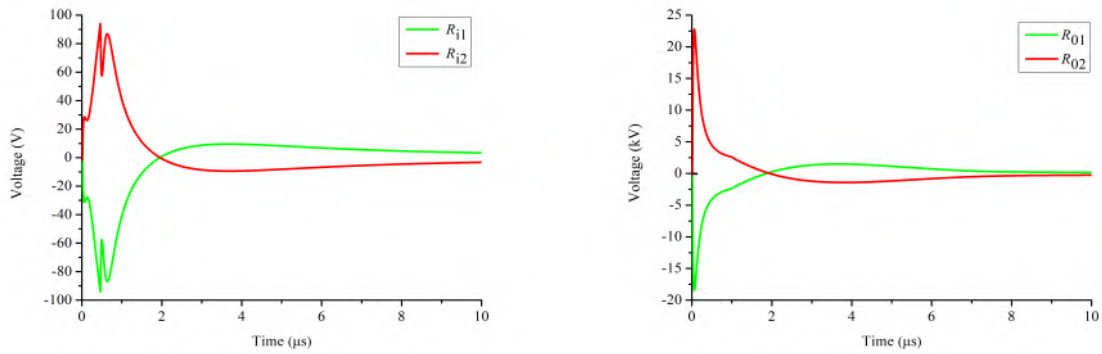
(a) Wire-to-shield voltage   (b) Shield-to-ground voltage

Figure 4.13 The voltage responses on the internal and external loads of the buried shielded cable

macromodel are shown in Figure 4.11. For comparison, the results in [148] obtained by the frequency-domain method with inverse Fourier transform are also shown in the figure. Apparently, all results are in good agreement.

Then the transient responses of incident field coupling to a buried RG-58 coaxial cable in Figure 4.12 are calculated and analyzed. The parameters of incident field and cables are same as those of the above one. The voltage responses on all internal and external loads computed by the proposed macromodel are shown in Figure 4.13, from which the induced current with a peak value of about $90/50 = 1.8$ A flows through the inner load. If the cable were not shielded, the induced current on the outer loop is about 150 A, which will give rise to peak values on the order of $150 \times 50 = 7.5$ kV. So the shield layer plays a relatively good role ($20lg(150/1.8) = 38.4$ dB) in protecting internal electronic systems from the external transient field coupling.

4.2.3 Example 3: the transient field coupling to three-phase buried cables

This example will focus on demonstrating the validity of the proposed model for field coupling to buried cables terminated with nonlinear loads. In this example, the incident field couples to buried 500-m long horizontally-configured three-phase 110 kV power cables. The cable cross-section has been shown in Figure 4.1. Because the over-voltage protection for metallic sheath layer of high voltage power cables is a key point in practical engineering application, In this case, we only consider the induced responses on metallic sheath, so only the outer insulation and metallic sheath are depicted in the following figures. Generally, one end of metallic sheath of three-phase cables must be interconnected and well-grounded, as shown in Figure 4.14, while the other end cannot be grounded directly, due to the existence of circulation current flowing on the metallic sheath. Nevertheless, external field may irradiate the metallic sheath, and induce high surge voltages on ungrounded ends, which may exceed the insulation level of the outer sheath, severely damage the cable and result in multipoint earthing fault.
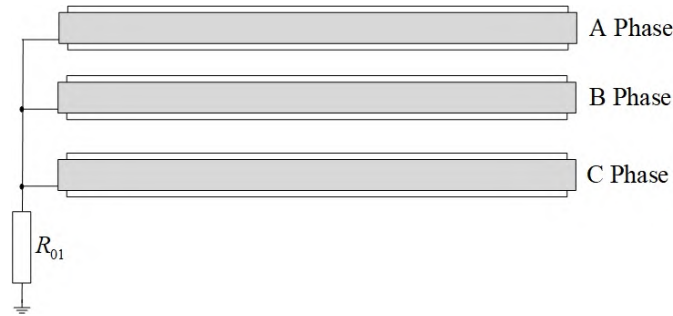
Figure 4.14 The configuration of three-phase buried cables with metallic sheaths interconnected and well-grounded at one end

The induced voltage on sheath of three-phase cables in horizontal configuration (see Figure 4.15) are chosen to be investigated. The radius of outer insulator and metallic sheath r_4 and r_3 are 36.75 mm and 32.75 mm, respectively. The time expression of the amplitude of incident field is $E_0(t) = 1.3 \times 50 \times (e^{-t \times 4 \times 10^7} - e^{-t \times 6 \times 10^8})$ kV/m and its incident angles are $\psi = 45°$, $\phi = 0°$ and $\alpha = 0°$. In practice, geometric arrangements of three phases depend on actual requirement of engineering, which generally include horizontal, triangular and perpendicular configurations. In this example, the horizontal arrangement (see Figure 4.15) of cables are considered, and modeling of other arrangements can also be easily realized without any difficulty. Using the proposed model, the induced voltages at the open-circuited ends of phases A, B and C are calculated when ground conductivity σ_g are 0.001 S/m and 0.01 S/m, respectively. All results are shown in Figure 4.16.

As shown in Figure 4.16, the waveforms of induced voltages on phases A, B and C for different conductivities almost overlap. The peak value of the induced voltages on phase B conductor is lowest due to the shielding effect of the other two phases. Table 4.3 lists the
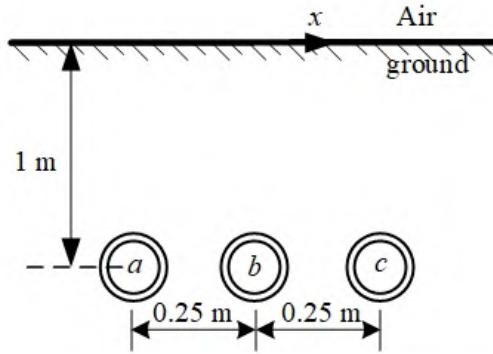
Figure 4.15 The horizontal configuration of three-phase buried cables (the inner core is not depicted)
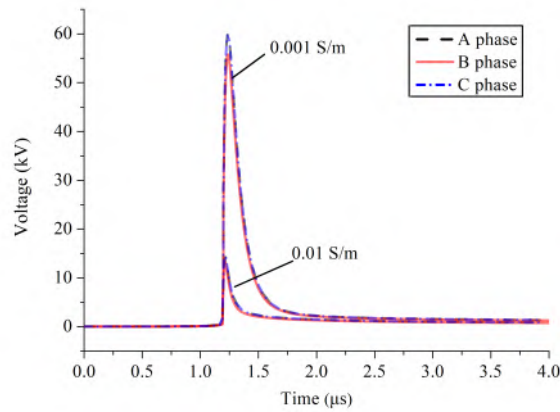
Figure 4.16 The induced voltages on metallic sheaths at the open-circuited end of the three-phase buried cables in Figure 4.15

Table 4.3 Simulation times of the proposed model

ground conductivity (S/m)	simulation time (s)
0.01	13.79
0.001	12.53

simulation time of the proposed method for two conductivity values. It is worth noting that all the simulation times of the proposed model for field coupling to multi-conductor buried cables is within 15 s, which is markedly faster than that of the FDTD method for a buried cable.

Furthermore, when σ_g is 0.001 S/m, the peak voltages on metallic sheath increase considerably, which exceed the impulse insulation level of 50 kV for 110 kV power cable and may affect the cable itself. Therefore, in reality, the ungrounded end of the metallic sheath can be connected to a sheath protector (see Figure 4.17), which generally consists of zinc oxide varistors, and behaves as a nonlinear device. In the following part, the field coupling to cables connected with the nonlinear protective device, as shown in Figure 4.17, is simulated using the

proposed model.
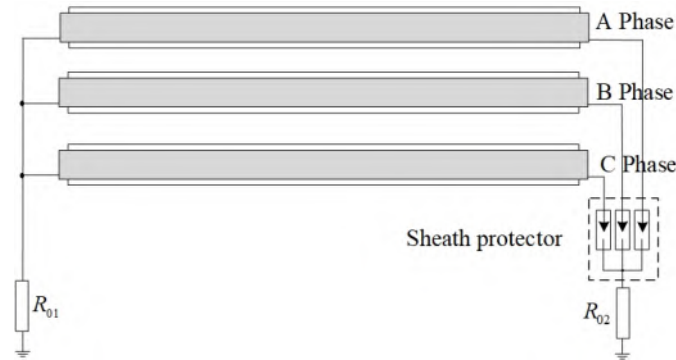
Figure 4.17 The configuration of three-phase buried cables connected with a sheath protector

The type of sheath protector adopted here is BHQ-8/600. Its V-I characteristic is depicted in Figure 4.18, and the specific parameters are listed in Table 4.4. All other parameters of incident field and cables are same as those in the above simulation. The induced voltages for two ground conductivities are shown in Figure 4.19, where the results of open-circuited cases are also shown for comparison.
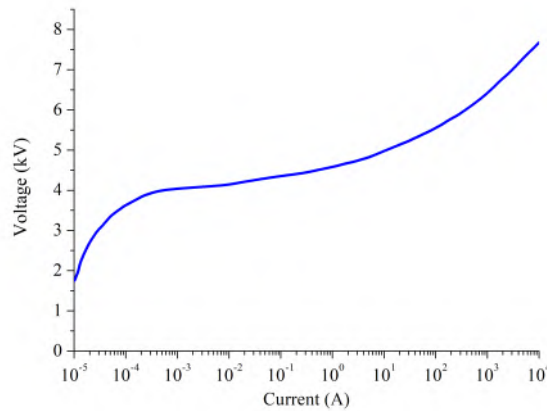
Figure 4.18 V-I characteristic of the sheath protector BHQ-8/600

Table 4.4 Main technical parameters of the sheath protector

Type	Rated Voltage (kV)	8/20 μs nominal discharge current/kA	DC U_{1mA} voltage reference/kV	Residual voltage under the nominal discharge current/kV
BHQ-8/600	110	10	≥ 4	8

As Figure 4.19 shows, the peak values of voltage impulses decrease significantly with the adoption of the protective nonlinear device, and 1.4 times of the residual voltages of the sheath
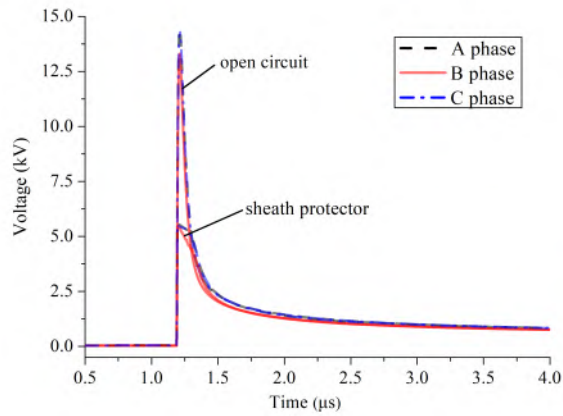
(a) Induced voltages for $\sigma_g = 0.01$ S/m
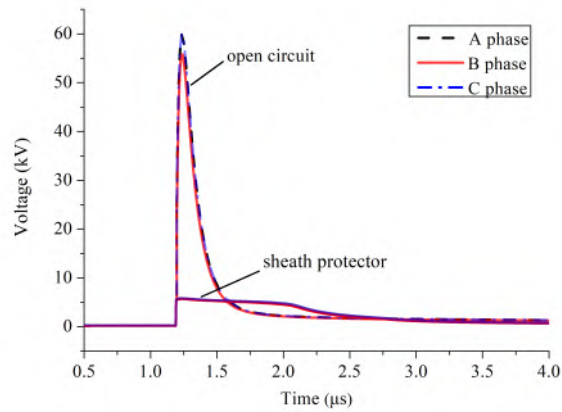
(b) Induced voltages for $\sigma_g = 0.001$ S/m

Figure 4.19 The induced voltages at the end of the metallic sheath of three-phase cables for two different ground conductivities

protector are still lower than the impulse insulation level, which meets the requirements of the insulation margin for protectors in the standard.

4.3 Concluding remarks

A time-domain macromodeling method is proposed in this chapter to calculate transient responses of buried cables to incident field coupling. The frequency-dependent variables are modeled using frequency response tables in ABM library directly, by which the time-domain convolution is calculated by the solver. Furthermore, approximation expressions for integral formulation of self and mutual ground impedance and admittance are proposed by an analogy with the existing closed-form expressions. It has been assessed that the evaluation time is reduced significantly compared to that of the AI formulation on the same computing platform.

Hence, compared with the existing time-domain numerical algorithms, the proposed algorithm avoids the time and spatial discretization and inefficient transient ground parameter evaluation, largely simplifies and speeds up the modeling and simulation processes. Several examples are presented in this chapter, including field coupling to underground communication and power insulated cables. According to the numerical validation, the proposed macromodel is proved to be accurate and efficient enough to carry out transient analysis for field coupling to buried cables terminated with linear and nonlinear loads. Besides, this algorithm can also be modified to model field coupling to overhead shielded cables above lossy ground, which is especially of great significance for the analysis of radiated and conducted susceptibilities of communication systems. Also like overhead TL networks, it is also convenient to model field coupling to buried TL networks, which is not be covered in this chapter to avoid repetition.

Nevertheless, the proposed 2-n port model can only estimate responses at terminal ports of n-cables in time domain. As for the most commonly used FDTD method, though the time and spatial discretization cannot be avoided, the voltages and currents at any position along the lines can be obtained via this method. Hence, if only responses on terminal devices are required, the proposed model will be a preferable choice compared to FDTD because of its higher efficiency and accuracy. And FDTD is still a necessary method to compute responses at any positions along lines, though it requires more time and memory space.

5 A wide-frequency circuit model for windings of power transformers

The MTL model, in which each turn in the winding is treated as a TL with the same length, has been widely used for wide-frequency modeling of large power transformer windings. At present, in the field of simulation analysis for the transformer winding, the MTLs model is mostly carried out in the frequency domain. Though the tedious convolution integral will be avoided, the spectrum aliasing and leakage may lead to errors. Furthermore, considering the presence of non-linear components and phenomena, an efficient and accurate time-domain modeling method for straightforward transient evaluation of over-voltages in the winding is desirable. And above all, the proposed model can be realized in the circuit solver, and be directly combined with equivalent circuit models of MTLs or other divices which have been studied and discussed in previous chapters.

Hence, in this chapter, we aim at presenting a modeling approach, by which the MTLs equations of transformer windings can be solved, to obtain responses in time domain by the equivalent circuit in SPICE efficiently. In the previous chapter, we have proposed an accurate and efficient macromodel for MTLs, and the frequency-domain devices of ABM library are adopted to model frequency-dependent parameters and calculate convolutions. So in this chapter, the macromodel of MTLs is firstly modified to model the transformer winding by considering the boundary condition. Then, the input impedance's formula of the winding and transfer functions of the voltage responses are derived by solving Telegrapher's equations. So the input-port model of the winding and the transfer function's circuit model can be established. The proposed models can be combined with models of MTLs or other elements, to perform transient analysis of system's multiple components conveniently and efficiently.

The specific content is arranged as follows: in section 5.1, we give a derivation of the circuit model for the transformer winding. Then in section 5.2, two examples are presented and analyzed to demonstrate the proposed models.

5.1 Derivation of the circuit model for the transformer winding

5.1.1 The input-port model of the transformer

As introduced in [149], the connection between the high-voltage winding of the power transformer and the power system is usually through bushing, so an equivalent circuit in Figure 5.1 could be considered for analyzing the invading voltage wave at the port of winding and induced responses in the inner winding.

In Figure 5.1, R_1 and L_1 are resistance and inductance of the lead wire connecting the
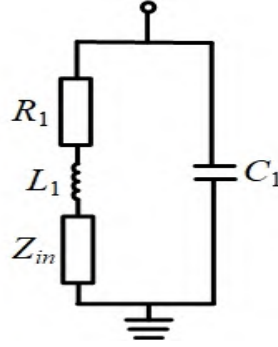
Figure 5.1   The input-port model of the transformer

winding and bushing; Z_{in} represents the input impedance of the winding, and C_1 is the equivalent capacitance to earth of bushing. Generally, the bushing capacitance C_1 is with a value of hundreds of pF, L_1 is several μH and R_1 is between 0.1-5 Ω. Once Z_{in} is determined with specific coil parameters, the circuit model in Figure 5.1 can directly be treated as a terminal load, so that the invading voltage wave flowing from the power system into the winding is obtained.

5.1.2   The MTLs model of the transformer winding
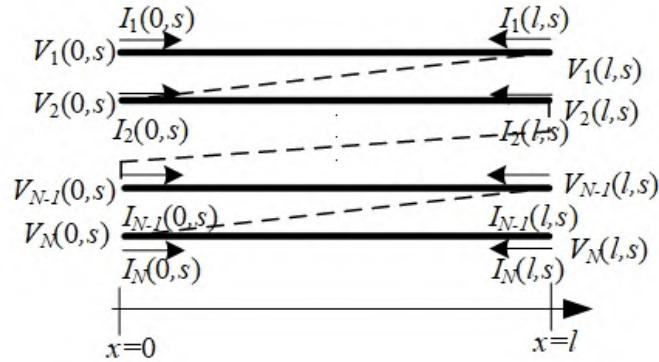
Figure 5.2   Equivalent MTL model of the transformer winding

The winding is split along the plane of the central shaft, and each turn of the coil is expanded into a straight line. We assume that the electrical connections between turns remain fixed, and specify that turns are numbered in the order of electrical connections instead of in the order of position (the total number of turns is N). The equivalent MTLs model of transformer winding is shown in Figure 5.2. In this model, each turn is treated as a TL with the length of l. The $\mathbf{V}(0,s) = [V_1(0,s), \cdots V_N(0,s)]^T$ and $\mathbf{I}(0,s) = [I_1(0,s), \cdots , I_N(0,s)]^T$ represent voltages and currents at head ends, and correspondingly, $\mathbf{V}(l,s) = [V_1(l,s), \cdots V_N(l,s)]^T$ and $\mathbf{I}(l,s) = [I_1(l,s), \cdots I_N(l,s)]^T$ are vectors of voltages and currents at terminal ends. Hence, the Telegrapher's equations of N turns in Laplace domain can be written as

$$-\frac{d}{dx}\left[\begin{array}{c} \mathbf{V}(x,s) \\ \mathbf{I}(x,s) \end{array}\right] = \left[\begin{array}{cc} \mathbf{0} & \mathbf{R}+s\mathbf{L} \\ \mathbf{G}+s\mathbf{C} & \mathbf{0} \end{array}\right]\left[\begin{array}{c} \mathbf{V}(x,s) \\ \mathbf{I}(x,s) \end{array}\right] \tag{5-1}$$

in which $N \times N$ matrices $\mathbf{R}$, $\mathbf{L}$, $\mathbf{G}$ and $\mathbf{C}$ are p.u.l resistance, inductance, conductance and capacitance.

According to the connection order of turns, the boundary condition can be described as: the voltage at the terminal end of the k-th ($k = 1, 2, 3, \cdots, N-1$) TL equals to the voltage at the head end of the $(k+1)$-th TL; the current at the terminal end of the k-th TL has the same value with that at the head end of the $(k+1)$-th TL, but the direction is opposite; the voltage at the head end of the first turn is the input voltage wave, and the end of the last turn in transformer winding is usually directly grounded. There are $2 \times N$ equations in the boundary condition:

$$V_1(0) = V_{in} \tag{5-2a}$$

$$V_k(l) = V_{k+1}(0) \tag{5-2b}$$

$$I_k(l) = -I_{k+1}(0) \tag{5-2c}$$

$$I_N(l) = 0 \tag{5-2d}$$

5.1.3 The formulation of p.u.l parameters in MTL model of transformer winding

1) The p.u.l resistance matrix

Since the skin effect of the conductor becomes obvious in high-frequency range, the influence of frequency should be taken into account when calculating distributed resistance parameters, i.e. the p.u.l resistance is composed by two parts:

$$\mathbf{R} = \mathbf{R}_0 + \mathbf{R}_s \tag{5-3a}$$

$$\mathbf{R}_0 = R_0\mathbf{E} \tag{5-3b}$$

$$\mathbf{R}_s = R_s\mathbf{E} \tag{5-3c}$$

in which $\mathbf{E}$ is the unit matrix, and R_0 and R_s are expressed as

$$R_0 = \frac{1}{d_1 d_2 \sigma} \tag{5-4a}$$

$$R_s = \frac{1}{2(d_1+d_2)}\sqrt{\frac{\pi f \mu}{\sigma}} \tag{5-4b}$$

d_1 and d_2 are the length and width of the cross section of rectangular conductor, respectively. σ refers to the conductor's conductivity, μ is the permeability and f represents the frequency.

2) The p.u.l capacitance matrix
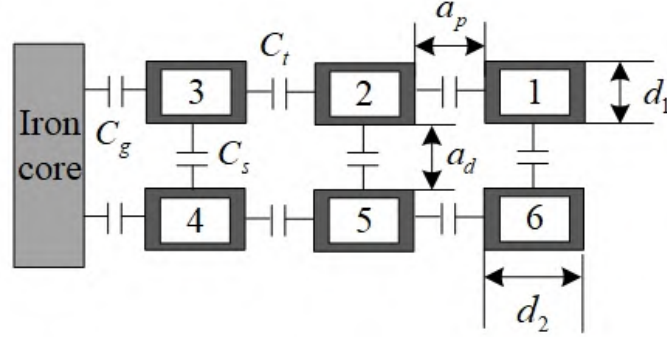
Figure 5.3 The schematic of equivalent capacitances of a transformer winding

In power transformers, the winding is generally composed of dozens or even hundreds of discs, and each disc is composed of dozens of turns. Taking the disc-type continuous winding as an example, Figure 5.3 shows the schematic of equivalent capacitances of a transformer winding. $N_1 = 3$ is the number of turns in each disc, and there are totally $N_2 = 2$ discs in the winding. In Figure 5.3, there are three kinds of capacitances should be considered, including capacitances to earth C_g of the turns near the iron core, the turn-to-turn capacitances C_t and capacitances between discs C_s. These distributed capacitances can be evaluated by modeling in the finite element software, or simply by the formula of parallel-plate capacitance and the coaxial cylinder capacitance formula. Here, we resort to formulae to calculate above capacitances, and according to the formula of parallel-plate capacitance, we have

$$C_t = \frac{\varepsilon_0 \varepsilon_p d_1}{a_p} \quad \text{F/m} \tag{5-5a}$$

$$C_s = \frac{\varepsilon_0 \varepsilon_{de} d_2}{a_d} \quad \text{F/m} \tag{5-5b}$$

in which ε_{de} is the equivalent permittivity of the insulation between discs; ε_p represents the equivalent permittivity of the insulation between turns; a_d is the thickness between discs; a_p is the thickness of the turn-to-turn insulation. Then based on the coaxial cylinder capacitance formula, C_g can be expressed as

$$C_g = \frac{2 d_1 \varepsilon_0 \varepsilon_{we}}{d_a \ln \frac{R_w}{R_i}} \quad \text{F/m} \tag{5-6}$$

d_a is the average diameter of the disc; ε_{we} is the equivalent permittivity of all media between the coil and the iron core; R_w is the inner radius of the coil and R_i is the circumradius of the iron core. A complete p.u.l capacitance matrix is obtained by these three capacitances, and for the winding structure in Figure 5.3, matrix $\mathbf{C}$ can be written as

$$\mathbf{C}=\begin{bmatrix} C_t+C_s & -C_t & 0 & 0 & 0 & -C_s \\ -C_t & 2C_t+C_s & -C_t & 0 & -C_s & 0 \\ 0 & -C_t & C_g+C_t+C_s & -C_s & 0 & 0 \\ 0 & 0 & -C_s & C_g+C_t+C_s & -C_t & 0 \\ 0 & -C_s & 0 & -C_t & 2C_t+C_s & -C_t \\ -C_s & 0 & 0 & 0 & -C_t & C_t+C_s \end{bmatrix} \tag{5-7}$$

Apparently, the diagonal elements in $\mathbf{C}$ are the capacitance to the ground of the corresponding turn plus the mutual capacitances with other turns; the off-diagonal elements are the negative of the mutual capacitance between two corresponding turns.

3) The p.u.l inductance matrix

If no high-frequency component of the electromagnetic wave enters into the core, the winding may be considered as a conductor wrapped by an insulating material in free space, the corresponding inductance is denoted as $\mathbf{L_0}$. At high frequencies, the magnetic flux penetrating the conductor can also generate inductance, so $\mathbf{L_s}$ represents the contribution of skin effect to the inductance. Hence, similar to resistance, the p.u.l inductance matrix includes two parts, i.e. $\mathbf{L} = \mathbf{L_0} + \mathbf{L}_s$. The specific expressions of them are

$$\mathbf{L_0} = \frac{\varepsilon_r}{c^2}\mathbf{C}^{-1} \tag{5-8a}$$

$$\mathbf{L_s} = \frac{\mathbf{R_s}}{2\pi f} \tag{5-8b}$$

in which ε_r is the relative permittivity of insulation; c is the speed that light travels in the vacuum.

4) The p.u.l conductance matrix

The conductance matrix $\mathbf{G}$ can be obtained according to the capacitive loss of insulating material, which is related to the frequency, capacitance and dielectric dissipation factor, i.e.

$$\mathbf{G} = 2\pi f \mathbf{C} \tan\delta \tag{5-9}$$

In general, the dielectric dissipation factor can be expressed as:

$$\tan\delta = 0.07 \times \left(1 - \frac{6}{7}e^{-0.308f\times 10^{-6}}\right) \tag{5-10}$$

5.1.4 The establishment of equivalent circuit model for the transformer winding

Apparently, the Telegrapher's equation in (5-1) can easily be solved in time domain by modeling an equivalent circuit based on ABM and generalized MoC algorithm, as elaborated in chapter 2. Considering the boundary condition mentioned above, the integrated macromodel for a transformer winding can be realized as shown in Figure 5.4, just by connecting the end port of each turn's two-port model to the start port of the next turn's model. V_{in} is the source representing the invading voltage, and the end port of the last turn is generally short-circuited to the ground.
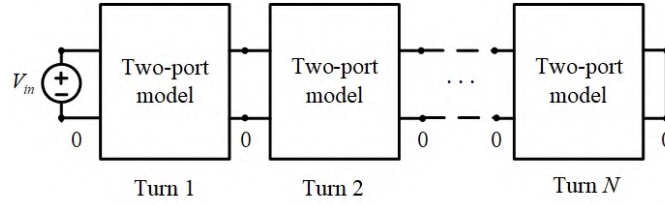
Figure 5.4 The integrated macromodel realization of a transformer winding

Though we just focus on responses on the first a few turns of the entire coil, the voltage and current responses on turns and voltage differences between turns must be obtained by carrying out the simulation in SPICE with the macromodel of the whole winding. However, as we know, with the increase of the number of TLs (turns) in the coil, the macromodel will inevitably become complicated. Consequently, huge demand for computing resources is of necessity, and the simulation efficiency will be impaired. Hence, a simpler or an alternative model is expected to perform more efficient analysis for large windings.

In the following part, we firstly solve equations in (5-1) in frequency domain, then derive the input impedance and voltage transfer functions on account of the boundary condition. The solution to (5-1) can be expressed in the form of Y-parameter matrix, which relates the terminal currents to the terminal voltages as

$$\begin{bmatrix} \mathbf{I}(0,s) \\ \mathbf{I}(l,s) \end{bmatrix} = \begin{bmatrix} \mathbf{Y_C}\coth\mathbf{\Gamma}l & -\mathbf{Y_C}\text{csch}\mathbf{\Gamma}l \\ -\mathbf{Y_C}\text{csch}\mathbf{\Gamma}l & \mathbf{Y_C}\coth\mathbf{\Gamma}l \end{bmatrix} \begin{bmatrix} \mathbf{V}(0,s) \\ \mathbf{V}(l,s) \end{bmatrix} \tag{5-11}$$

where

$$\mathbf{\Gamma}(s) = \sqrt{(\mathbf{R}+s\mathbf{L})(\mathbf{G}+s\mathbf{C})} \tag{5-12a}$$

$$\mathbf{Y_C}(s) = (\mathbf{R}+s\mathbf{L})^{-1}\mathbf{\Gamma}(s) \tag{5-12b}$$

Substituting the boundary condition of (5-2) into (5-11), so (5-11) is simplified by eliminating

$(N-1)$ currents and merging $(N-1)$ voltages as

$$\begin{bmatrix} I_1(0) \\ 0 \\ \vdots \\ 0 \\ I_N(l) \end{bmatrix} = \mathbf{Y}_1 \begin{bmatrix} V_1(0) \\ V_2(0) \\ \vdots \\ V_N(0) \\ V_N(l) \end{bmatrix} \qquad (5\text{-}13)$$

$\mathbf{Y_1}$ is a $(N+1)\times(N+1)$ matrix. Defining $\mathbf{M} = \mathbf{Y}_1^{-1}$, (5-13) can be changed to

$$\begin{bmatrix} V_1(0) \\ V_2(0) \\ \vdots \\ V_N(0) \\ V_N(l) \end{bmatrix} = \mathbf{M} \begin{bmatrix} I_1(0) \\ 0 \\ \vdots \\ 0 \\ I_N(l) \end{bmatrix} \qquad (5\text{-}14)$$

So the voltage at the end of k-th turn and at the head of the $(k+1)$-th turn $(k = 1, 2, 3, \cdots, N-1)$ can easily be obtained by

$$V_k(l) = V_{k+1}(0) = M(k+1,1) I_1(0) + M(k+1,N+1) I_N(l) \qquad (5\text{-}15)$$

And from (5-14), we can also obtain

$$I_1(0) = \frac{M(N+1,N+1) V_1(0) - M(1,N+1) V_N(l)}{M(1,1) M(N+1,N+1) - M(N+1,1) M(1,N+1)} \qquad (5\text{-}16a)$$

$$I_N(l) = \frac{M(1,1) V_N(l) - M(N+1,1) V_1(0)}{M(1,1) M(N+1,N+1) - M(N+1,1) M(1,N+1)} \qquad (5\text{-}16b)$$

We can treat the winding in Figure 5.2 as a single-input multi-output multi-port network, so if $V_1(0) = V_{in}$ and $V_N(l) = 0$, the input impedance Z_{in} in Figure 5.1 is given as

$$Z_{in}(s) = \frac{V_1(0)}{I_1(0)} = \frac{M(1,1) M(N+1,N+1) - M(N+1,1) M(1,N+1)}{M(N+1,N+1)} \qquad (5\text{-}17)$$

and the output voltage at the terminal end of the k-th turn can be related with the input voltage wave by the transfer function $F_k(s)$ as

$$V_k(l) = V_{k+1}(0) = F_k(s) V_{in} \qquad (5\text{-}18a)$$

$$F_k(s) = \frac{M(k+1,1) M(N+1,N+1) - M(k+1,N+1) M(N+1,1)}{M(1,1) M(N+1,N+1) - M(N+1,1) M(1,N+1)} \qquad (5\text{-}18b)$$

In the existing time-domain method for solving MTLs model of the transformer winding, vector fitting is widely utilized to approximate frequency-dependent variables, which may lead to numerical errors and tedious time-domain convolution calculation. Here, for simplifying the calculation and simulation, the input-port model and the circuit model of transfer functions can be realized in SPICE, as shown in Figure 5.5, the frequency-dependent impedance Z_{in} and the transfer function in (5-18b) can be modeled by frequency-domain ABM devices, such as frequency response tables. The load resistance R in the figure is used to avoid the floating node. Then, the invading voltage V_{in} obtained from the input-port model is directly assigned as the input of the controlled voltage source $V_k(l)$, by which the output voltage $V_k(l)$ can easily be calculated in SPICEduring transient analysis.

(a) The input-port model of the transformer winding

(b) The equivalent circuit of the transfer function $F_k(s)$
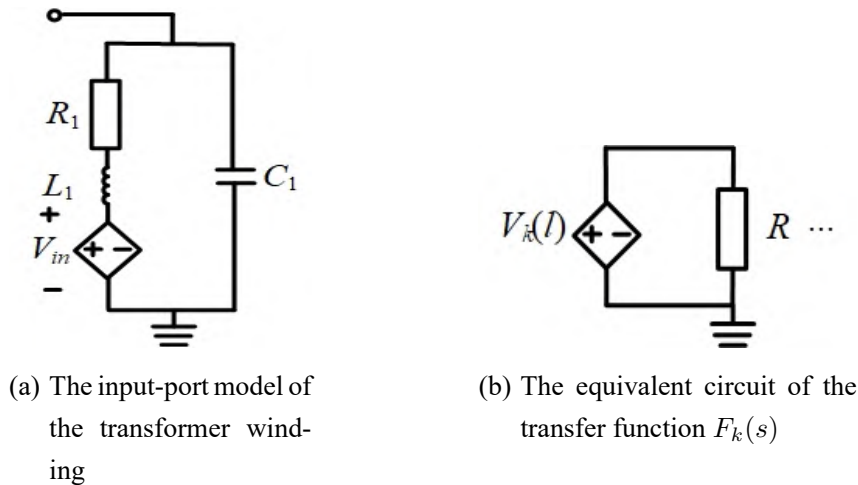
Figure 5.5 The circuit realization of the input-port model of the transformer winding and the transfer function

Compared with the existing time-domain method, the equivalent circuit model is easy to implement, which leaves out of procedures of discretization in finite difference methods and the numerical approximation for transient parameter evaluation. Especially, the circuit model of the transfer function $F_k(s)$ can be solved by SPICE-like solvers with input-port model, which is more convenient to be connected to models of TLs and other elements in the system, and more efficient to simultaneously obtain the invading voltage at the input port and required responses on specified turns in the transformer winding.

5.2 Accuracy and efficiency validation by simulation

The voltage responses of two winding structures will be studied to demonstrate the validity and efficiency of equivalent circuit models. The simulation results are compared with those obtained by other methods. The simulations are carried out using PSpice on a PC equipped with an INTEL i7 3.6-GHz CPU.

5.2.1 Example 1: The voltage pulse invades into a simple continuous winding

In this example, for the sake of analysis convenience, we will firstly focus on a simple continuous winding with total $N_2 = 4$ discs, and there are $N_1 = 4$ turns in each disc. The basic parameters of the winding have been outlined in the Table 5.1. Using the formulations of capacitances in (5-5) and (5-6), we can obtain that $C_t = 121.3$ pF/m, $C_s = 10.5$ pF/m and $C_g = 16.1$ pF/m. The invading voltage pulse is chosen as a double exponential pulse. The integrated macromodel in Figrue 5.4 and the circuit model of transfer functions in Figure 5.5 are utilized to calculate responses of turns, when the wavefront of the input voltage wave is 1.2 μs and 0.25 μs, respectively. Taking the peak value of the input voltage as a reference value, Figure 5.6 shows the per-unit value of voltage responses at the end of 1st, 2ed, 3rd, 4th, 8th (the last turn of the second disc) and 12th (the last turn of the third disc) turn. For comparison, the results obtained by frequency-domain method combined with inverse Fourier transform (IFT) are also depicted in the figure.

Table 5.1 Basic parameters of the winding

Parameter	Average turn length (mm)	Conductor size (mm)	Relative permittivity of insulating paper	Conductor Conductivity (S/m)	Thickness of insulating paper (mm)
Value	1483	11.2×4	3.5	$3e7$	2.95

(a) The wavefront is 1.2 μs   (b) The wavefront is 0.25 μs
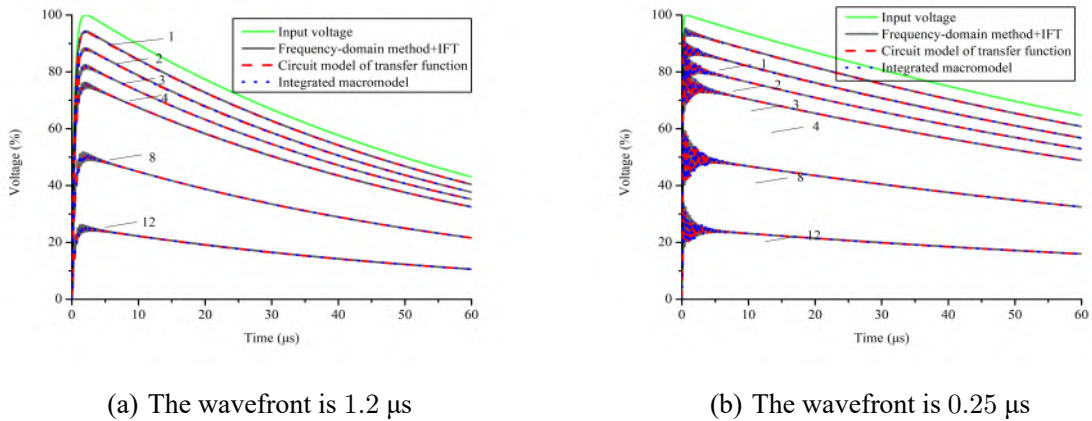
Figure 5.6 The per-unit value of voltage responses at the end of 1st, 2ed, 3rd, 4th, 8th and 12th turn

In Figure 5.6, the results of different methods are consistent with each other, which validates the accuracy of the proposed equivalent circuit model. Table 5.2 compares the simulation times of three methods for different wavefront values. It is clear that the circuit model of the

Table 5.2　The simulation times of three methods

Methods	Wavefront time	
	1.2 μs	0.25 μs
Frequency-domain method+IFT (s)	80.61	92.32
Integrated macromodel (s)	270.65	250.31
Circuit model of transfer function (s)	2.31	2.56

transfer function performs greatly faster than the other two methods. The integrated macro-model is accurate enough, and the efficiency has been proved not to be limited by the length of TLs in the previous chapter. Besides, because only the coupling effect of adjacent TLs is considered in the turns, the macromodel will be simplified when the number of controlled souces representing coupling of other TLs is reduced, the efficiency will be further improved during the process of parallel analysis on the each turn's circuit model. However, the integrated macromodel in this chapter may encounter with problems of exceeding the number of threads allowed by the simulation software and simulation interruption due to the large winding size in practical transformers, in which the turns of each winding can be up to a few hundreds or even thousands. It is also worth noting that, if responses of different input voltage wave are required for one winding, the responses can be obtained just by changing the input of ABM devices in the circuit model. So it is applicable to carry out statistical analysis of input voltage waves.

We can also figure out from Figrue 5.6 that, when a pulse enters the winding, a similar voltage pulse with a steep rise is also generated on each turn in the winding, the voltage decreases slowly after reaching the maximum value, and the peak value decreases with the increase of the turn's number. Besides, the winding can be regarded as a network composed of capacitances and inductances, so voltage pulses can oscillate freely in the network, which results in turn-to-ground voltages with fluctuant waveforms, as shown in Figure 5.6. Meanwhile, we can observe that, the voltage fluctuation becomes more severe with the increase of the turn's number and the shortening of the wavefront time.

Finally, in Table 5.3, we list the maximum voltage differences of the first 4 turns for input voltage waves with different wavefront values. Table 5.3 shows that the maximum voltage difference becomes lower with the increase of turn's number, and it is also obviously influenced by the wavefront of the input voltage wave. Specifically, with the shortening of the wavefront, the maximum voltage difference becomes larger. Hence, the insulation of the first a few turns are more vulnerable to invading waves, especially to steep-front pulses.

Table 5.3 The maximum voltage differences of the former 4 turns

Maximum voltage difference	Wavefront time	
	1.2 μs	0.25 μs
1-to-2 (%)	6.784	11.123
2-to-3 (%)	6.457	9.205
3-to-4 (%)	5.868	9.029

5.2.2 Example 2: The voltage pulse invades into a 180-turn experimental continuous winding

In this part, we take a continuous experimental transformer winding given in [150] as an example. There are $N_2 = 18$ discs in the winding, $N_1 = 10$ turns in each disc, totally $N = 180$ turns in the winding. All other parameters are identical to those of example 1 in Table 5.1. A voltage pulse with 1.2 μs wavefront was applied to the start end of the first turn in the winding. The circuit model of the transfer function are utilized in this example to calculate voltage responses. We also take the peak value of the input voltage as a reference, Figure 5.7 depicts the time-domain induced voltage waveforms at the end of 1st, ..., 5th, 60th, 100th, 160th turn, and Figure 5.8 shows the per-unit voltage peak values at the end of 2ed, 4th, 6th, ..., 18th disc. The results of simulation and measurement obtained in [150] are also shown in the figure.
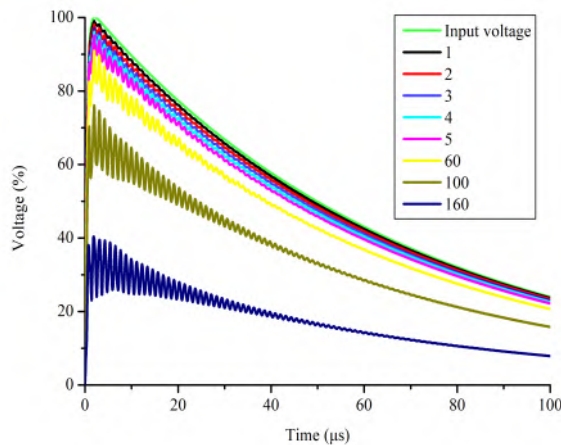
Figure 5.7 The induced voltage at the end of 1st, ..., 5th, 60th, 100th, 160th turn

From Figure 5.7, the response laws are consistent with those obtained in example 1, i.e., the peak values of voltage responses decrease and waveform fluctuation becomes more severe with the increase of the turn's number. From Figure 5.8, we can observe that the simulation
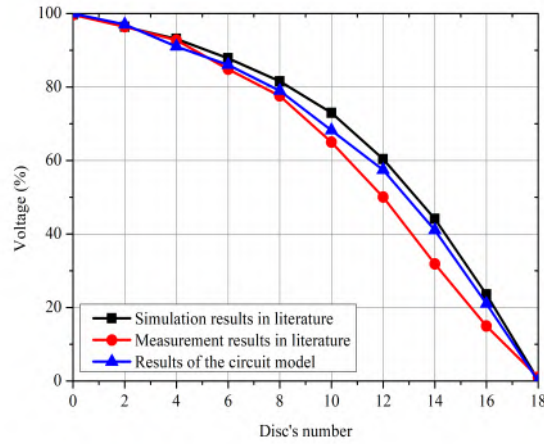
Figure 5.8　The comparison of voltage peak values at the end of 2ed, 4th, 6th, ..., 18th disc

results are roughly identical. The maximum error between simulation results in [150] and those obtained by the circuit model is about 4.74 %, and the maximum error between measurement results and simulation results of the circuit model is about 12.29 %. Furthermore, the voltage peak value of the disc near the incoming wave is the largest, and the peak value of the disc away from the incoming wave decreases successively, then it drops to 0 when it reaches the end of the winding. Specifically, the voltage responses of the 2ed, 4th and 6th are more than 80 % of the voltage at the head end, while the voltage responses of the 16th and 18th discs are lower than 20 %.
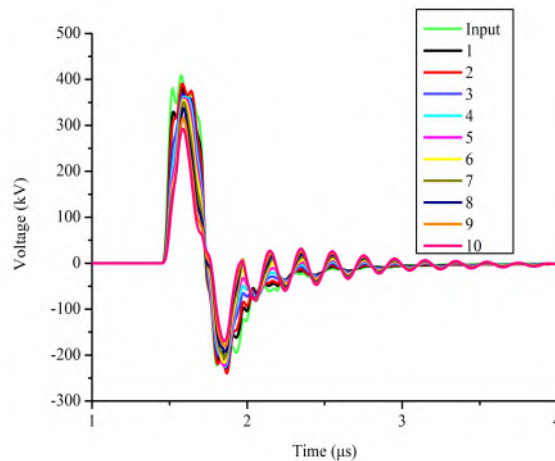
Figure 5.9　The induced voltage responses at the end of input port and of the first 10 turns

Then, as the terminal load, this winding is connected to an overhead TL illuminated by incident field. The length of the TL is 500 m, the height is 10 m and another end of the TL is terminated by its characteristic impedance. All other parameters of the field and ground are same with those in section 3.3.4. The induced voltages at the input port and turns' ends of the

Table 5.4 The maximum voltage differences of the former 10 turns

Turn's number	1-2	2-3	3-4	4-5	5-6	6-7	7-8	8-9	9-10
Voltage difference (kV)	50.9	37.6	30.8	29.1	28.3	27.4	21.7	16.6	28.2

first disc are calculated using the proposed model, and are then shown in Figure 5.9. Table 5.4 lists the maximum turn-to-turn voltage differences. Without loss of generality, for input-port model, it is assumed that R_1 is 2 Ω, L_1 is 2 μH and C_1 is 100 pF. It is shown from Figure 5.9 and Table 5.4 that the energy coupling from the external field can flow along the TL and enter into the transformer winding, which will induce over-voltages in the magnitude of hundreds of kilovolts at the first a few turns. And the maximum turn-to-turn voltage difference and electric field intensity can be up to approximately 50.9 kV and 17.25 kV/m. However, the turn-to-turn voltage difference and the electric field intensity of the transformer winding are related with the parameters of the connected TL and external field, so the possible maximum values of them cannot be evaluated just by simulating one scenario. According to the standard, we have known that the possible maximum peak value of the induced current on the TL exposed to the HEMP can be up to 5 kA, the wave-front is less than 20 ns, and the pulse width is between 500 ns and 550 ns. So in the following part, three typical pulses with different wave-front meeting the standard are adopted to study the maximum voltage difference of the transformer winding.

Table 5.5 The parameters of three waveforms of current pulses

Waveform	Wavefront time (ns)	Parameters		
		k	α	β
1	2.5	1.01	1.17×10^9	1.28×10^6
2	10	1.04	2.81×10^8	1.31×10^6
3	18	1.07	1.52×10^8	1.35×10^6

The double-exponential current pulse can be analytically expressed as

$$I(t) = k \times 5000 \times (1 - e^{(-\alpha t)})^{10} e^{(-\beta t)} \qquad (5-19)$$

The parameters k, α and β corresponding to three waveforms are all listed in Table 5.5. Figure 5.10 shows the maximum voltage differences of the first 10 turns for different input pulses. Obviously, the voltage difference between the first two turns are largest, and the faster the wave-front, the larger the maximum voltage difference. We can also observe from the Figure 5.10 that, the possible maximum voltage difference for the first several turns of the transformer
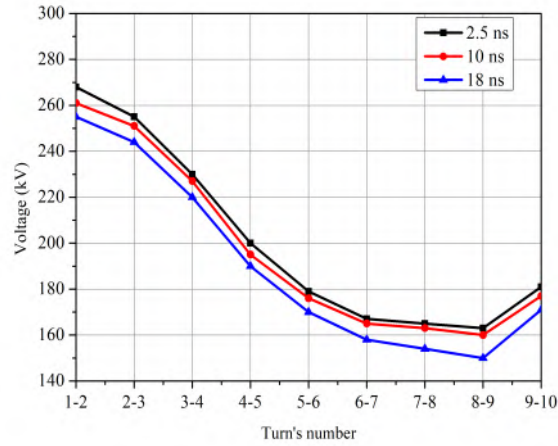
Figure 5.10 The maximum voltage differences of the first 10 turns for different input voltage pulses

winding due to incident field coupling to the TL can be up to hundreds of kilovolts, which means that the electric field intensity in the insulation between turns is around dozens of kilovolts per millimeter. Hence, the inner insulation of the transformer winding may be impaired because of the high turn-to-turn electric field intensity.

5.3 Concluding remarks

A modeling method of the transformer winding is proposed in this chapter to calculate transient responses on turns in the winding when a voltage pulse invades into the transformer. The frequency-dependent variables (input impedance and transfer function) are modeled using frequency-domain devices in ABM library directly, by which the time-domain convolution is calculated directly by the solver. So the input-port model of the transformer winding and transfer function's circuit model can be established, which can be combined with equivalent circuits of MTLs or other elements in the system, and perform the tansient analysis conveniently and efficiently.

Hence, compared with the existing time-domain algorithms, the proposed algorithm avoids the inefficient numerical approximation, order reduction and the corresponding accuracy loss. So it will be more appropriate to carry out transient analysis of transformer windings in SPICE. Besides, the integrated macromodel of the winding can also be modified to be more efficient if accurate and simplified hybrid model are available.

6　Conclusions and perspectives

6.1　Summary

The TEDs may couple to MTLs, and the induced voltages and currents on lines may cause serious effects or even damage to TLs and connected terminal equipment. Hence, the time-domain theoretical modeling of MTLs to field coupling is of great significance for the study of their response laws and protection technologies, when the frequency-dependent variables and nonlinear elements in the system must be considered simultaneously. Hence in this dissertation, a time-domain macromodeling algorithm based on the generalized MoC and ABM is proposed to study transient responses on overhead and buried MTLs, and connected terminal equipment excited by the transient field. Firstly, using the instantaneous and frequency-domain devices in ABM library, a time-domain macromodel for MTLs is established. Especially, several important aspects and parameters which are related to the accuracy and passivity of the model are analyzed. Second, the macromodel of MTLs is extended to model field coupling to MTLs and TL networks above lossy ground. Then, for the problems of field coupling to buried cables, a macromodel that can estimate transient responses of buried coaxial single-core cables is presented. Finally, taking the power transformer, a typical coil-type terminal equipment as the research object, a wide-frequency circuit model for the transformer winding is established, to perform transient analysis with models of other system's components in SPICE conveniently and efficiently. The main research achievement are as follows:

(1) The instantaneous devices and frequency-domain devices of ABM are utilized to model frequency-dependent characteristics and nonlinear components during transient analysis. Some criteria and constraints for accurate transient simulation of frequency-domain parts are also proposed and analyzed. An accurate and efficient time-domain macromodeling algorithm is proposed to calculate transient responses of MTLs, in which the characteristic impedance (or admittance) and propagation operator of TLs are modeled using LAPLACE or FREQ devices directly. There is no need to implement the procedures of rational approximation and delay extraction during the modeling process, nor is partial decoupling used in generalized MoC and DEPACT macromodels necessary. Furthermore, the passivity of the proposed macromodel is intrinsically guaranteed if the p.u.l parameters are physically consistent and positive real. It is verified by an example that, the proposed algorithm can not only yield compact and accurate macromodel, but largely simplifies and speeds up the modeling and simulation processes. Hence, with the knowledge of empirical functions or tabulated data of parameters, the proposed model can be easily formulated and embedded in the SPICE with an accurate and efficient way for the transient analysis of lossy TLs terminated with linear or nonlinear loads.

(2) To model the MTLs and TL networks above lossy ground to field coupling, the proposed macromodel for MTLs is extended to include the field excitation and lossy ground. The expressions of p.u.l parameters, especially for ground impedance and admittance, are elaborated and discussed. The modularity and independence of the macromodel are utilized to model the TL network, by connecting two-port sub-models together. In addition, for certain scenarios, we proposed a simplified model for the network based on the Thevenin transformation, in which the discrete branches is equivalent to a one-port Thevenin circuit. According to the numerical validation, the proposed macromodel is proved to be accurate and efficient enough. The macromodel is utilized to carry out numerical studies about effects of line parameters, lossy ground, and ground wires on induced responses.

(3) A time-domain macromodeling method is proposed to calculate transient responses of buried cables to incident field coupling. Furthermore, approximation expressions for integral formulation of self and mutual ground impedance and admittance are proposed by an analogy with the existing closed-form expressions. It has been proved that the evaluation time is reduced significantly compared to that of the AI formulation on the same computing platform. Hence, compared with the existing time-domain numerical algorithms, the proposed algorithm avoids the time and spatial discretization and inefficient transient parameter evaluation generally used in FDTD method, largely simplifies and speeds up the modeling and simulation processes. Several examples are presented in this chapter. According to the numerical validation, the proposed macromodel is proved to be accurate and efficient enough to carry out transient analysis for field coupling to coaxial single-core buried cables terminated with linear and nonlinear loads. Also, like overhead TL networks, the macromodel for filed coupling to buried wire networks can also be easily realized.

(4) A circuit model of the transformer winding is proposed to calculate transient responses on turns in the winding when a voltage pulse invades into the transformer. The frequency dependent variables (input impedance and transfer function) are derived and modeled using frequency response tables in ABM library of PSpice software directly. So the input-port model of the transformer winding and transfer function's circuit model can be established, which can be connected to the models of MTLs or other elements in the system to perform transient analysis conveniently and efficiently. Compared with the existing time-domain algorithms for voltage distribution calculation of the transformer winding, the TL is not needed to be discretized into cells anymore. It also avoids the inefficient numerical approximation and order reduction.

6.2 Future work

In this dissertation, the research results of the modeling method for transient field coupling to MTLs have been obtained. However, due to the limitation of ability and energy, there are still

some problems to be solved. Further research can be carried out from the following aspects.

(1) The present macromodel is proposed based on the classical TL theory, which is only valid for the uniform TL. However, considering the non-uniform TL, such as twisted-pair lines and lines with vertical risers, the scattering theory becomes necessary. Some numerical full-wave methods including FDTD, finite element and method of moment have been applied to this problem with the requirement of the large computation time and memory sources. In the future work, the macromodeling algorithm may can be studied based on full-wave method to extend its application to the more practical cases.

(2) In this dissertation, we only study a single transformer winding, of which the last turn is short-circuited to the ground and the coupling of other windings in the transformer is not considered. In the future work, the SPICE circuit model should be modified and improved to consider practical multiple and complex operation status of the transformer in the overvoltage analysis of transformer windings.

(3) The present modeling method studied in this dissertation is still a bit theoretical, which is not very applicable to model practical transmission systems. In the future work, the macro-model can be optimized and improved, such as the corona discharge and frequency dependence of the real ground, and so on, are included in the model.

Acknowledgements

It is with immense gratitude that I acknowledge the support of everyone who has shared their knowledge and experience, and given their time to help me to go through all the difficulties and complete the research work of this dissertation.

First of all, I wish to extent my appreciation and gratitude to Professor Yan-zhao Xie and Professor Flavio Canavero for their knowledge, experience and kindness. Their invaluable advice during supervision made the work of this dissertation less difficult and more enjoyable.

Then, I would like to thank Professor Qing Liu from Xi'an University of Science and Technology, Dr. Kejie Li from Hefei University of Technology and Professor Jun Guo, Dr. Shaoyin He, Dr. Shaofei Wang and Dr. Tao Liang from Xi'an Jiaotong University for many useful discussions on my research. Their ideas, comments and suggestions were always appreciated. I wish to thank the following colleagues for making study in HPEMC group an enjoyable experience: Xiaoyu Ge, Yanpeng Ge, Yi Zhou, Qi Li, Yuhao Chen, Hongye Zhang, Ning Dong, Mingxiang Gao, Tongqiang Yi, Ruijiang Sun, Minzhou Liu, Yangxin Qiu, HeNan Liu, Yuchen Lai, Siqi Wang, Zeqi Lv, Mingyue Gou, Daozhong Zhang, Dechang Ren, Yang Ma, Qing Cao, Xin'an Jiang et al. I would like to thank all professors, staff and students in HPEMC group for their supportive and friendly manner.

Next, I wish to thank Professor Shengchang Ji and Professor Hongjie Li, for taking time from their busy jobs to review my dissertation very carefully.

My final thought are with my parents, my grandfather and grandmother, my boyfriend Jingtan Ma, and all my families. Without their encouragement and endless support, I would not persist during my PhD study and have the opportunity to complete this dissertation's research.

Bibliography

[1] Nucci C A, Rachidi F, Ianoz M V, et al. Lightning-induced voltages on overhead lines[J]. IEEE Transactions on Electromagnetic Compatibility. 1993, 35(1):75–86.

[2] Guo J, Xie Y Z, Rachidi F. A semi-analytical method to evaluate lightning-induced overvoltages on overhead lines using the matrix pencil method[J]. IEEE Transactions on Power Delivery. 2018, 33 (6):2837–2848.

[3] Yao-jun X C W. Research on the perniciousness and protection technology of esd[J]. Science & Technology Information. 2010, 31.

[4] Shetye K, Overbye T. Modeling and analysis of gmd effects on power systems: An overview of the impact on large-scale power systems.[J]. IEEE Electrification Magazine. 2015, 3(4):13–21.

[5] Gold S H, Nusinovich G S. Review of high-power microwave source research[J]. Review of Scientific Instruments. 1997, 68(11):3945–3974.

[6] Gu X, Taylor L. Ultra-wideband and its capabilities[J]. Bt Technology Journal. 2003, 21(3):56–66.

[7] Wu H T, Jiao C Q, Cui X, et al. Transient electromagnetic disturbance induced on the ports of intelligent component of electronic instrument transformer due to switching operations in 500 kv gis substations[J]. IEEE Access. 2017, 5:5104–5112.

[8] Radasky W A, Baum C, Wik M. Introduction to the special issue on high-power electromagnetics (hpem) and intentional electromagnetic interference (iemi)[J]. Electromagnetic Compatibility IEEE Transactions on. 2004, 46(3):314–321.

[9] LI B, HE J, ZHOU H, et al. Study about induced current law by emp on transmission line[J]. Information and Electronic Engineering. 2010, 8(1):36–40.

[10] Li B, He J, Zhou H, et al. Electromagnetic interference of transmission line in hemp environment[J]. High Voltage Engineering. 2009, 35(11):2753–2758.

[11] Rachidi F. A review of field-to-transmission line coupling models with special emphasis to lightning-induced voltages on overhead lines[J]. IEEE Transactions on Electromagnetic Compatibility. 2012, 54(4):898–911.

[12] Zhou L, Zhang S, Yin W Y, et al. Investigating a thermal breakdown model and experiments on a silicon-based low-noise amplifier under high-power microwave pulses[J]. IEEE Transactions on Electromagnetic Compatibility. 2015, 58(2):487–493.

[13] Wang H, Li J, Zhou Y, et al. Theoretical and experimental study of complementary metal oxide semiconductor inverters under high-power microwave interferences[J]. Electromagnetics. 2009, 29 (5):393–405.

[14] Fang J, Shen J, Yang Z, et al. Experimental study on microwave vulnerability effect of integrated circuit[J]. High Power Laser and Particle Beams. 2003, 15(6):591–594.

[15] Tianle P, Changjun L, Liping Y. Experimental study on microwave radiation effects on personal computer[J]. High Power Laser and Particle Beams. 2006, 18(9):1549.

[16] Zhai A, Xie Y, Han J, et al. Effect of high altitude nuclear electromagnetic pulse upon phone call[J]. High Power Laser and Particle Beams. 2009, 21(10):1529–1533.

[17] Congmin W, Bo Z. The effect of hpm to electric equipment[J]. Aerospace Electronic Warfare. 2007, 5.

[18] Tesche F M, Barnes P R. The hemp response of an overhead power distribution line[J]. IEEE Power Engineering Review. 1989, 9(7):80–81.

[19] Rachidi F, Tkachenko S. Electromagnetic field interaction with transmission lines: from classical theory to HF radiation effects: volume 5 [M]: WIT press, 2008.

[20] Zhou X, Wang S, Wer G. Study on radiation effects of emp on digital circuits[J]. High Voltage Engineering. 2006, 10.

[21] Yu W, Huang W. The current-mode destroy of semiconductor devices by electromagnetic pulse[J]. High Power Laser and Particle Beams. 1999, 11:358–361.

[22] Qi G, Li K, Li Y, et al. Experimental study on effects of electromagnetic pulse on pipeline supervisory control and data acquisition (scada) system[J]. High Power Laser And Particle Beams. 2015, 27(12): 123202–1.

[23] Kruse V, Nickel D, Taylor E, et al. Impacts of a nominal nuclear electromagnetic pulse on electric power systems: a probabilistic approach[J]. IEEE Transactions on Power Delivery. 1991, 6(3):1251–1263.

[24] Meliopoulos A S, Glytsis E N, Cokkinides G, et al. Comparison of ss-gic and mhd-emp-gic effects on power systems[J]. IEEE transactions on power delivery. 1994, 9(1):194–207.

[25] Yuhao C, Yanzhao X, Minzhou L, et al. Analysis of high-altitude electromagnetic effect models on power system[J]. High Power Laser and Particle Beams. 2019, 31(07):31070007.

[26] Masdi H, Mariun N, Mohamed A, et al. Study of impulse voltage distribution in transformer windings[C]. PECon2010 - 2010 IEEE International Conference on Power and Energy, 2010: 379–383.

[27] Heidarzadeh M, Besmi M. Influence of the parameters of disk winding on the impulse voltage distribution in power transformers[J]. Iranian Journal of Electrical and Electronic Engineering. 2014, 10 (2):143–151.

[28] Miki A, Hosoya T, Okuyama K. A calculation method for impulse voltage distribution and transferred voltage in transformer windings[J]. IEEE Transactions on Power Apparatus and Systems. 1978, PAS-97(3):930–939.

[29] Dian-qian J, Gang H. Discussion about lightning protection for secondary system in 500kv substation[J]. Guangxi Electric Power. 2007, 12(1):5–9.

[30] Chou C J, Liu C W. Assessment of risks from ground fault transfer on closed-loop hv underground distribution systems with cables running in a common route[J]. IEEE Transactions on Power Delivery. 2013, 28(2):1015–1023.

[31] Tuinema B W, Rueda J L, van der Sluis L, et al. Reliability of transmission links consisting of overhead lines and underground cables[J]. IEEE Transactions on Power Delivery. 2015, 31(3):1251–1260.

[32] Bridges G E. Transient plane wave coupling to bare and insulated cables buried in a lossy half-space[J]. IEEE transactions on electromagnetic compatibility. 1995, 37(1):62–70.

[33] Petrache E, Rachidi F, Paolone M, et al. Lightning induced disturbances in buried cables-part i: theory[J]. IEEE Transactions on Electromagnetic Compatibility. 2005, 47(3):498–508.

[34] Xu F, Liu C, Hong W, et al. Fast and accurate transient analysis of buried wires and its applications[J]. IEEE Transactions on Electromagnetic Compatibility. 2013, 56(1):188–199.

[35] Paknahad J, Sheshyekani K, Rachidi F, et al. Lightning electromagnetic fields and their induced currents on buried cables. part ii: The effect of a horizontally stratified ground[J]. IEEE Transactions on Electromagnetic Compatibility. 2014, 56(5):1146–1154.

[36] Paulino J O S, Barbosa C F, do Couto Boaventura W. Lightning-induced current in a cable buried in the first layer of a two-layer ground[J]. IEEE Transactions on Electromagnetic Compatibility. 2013, 56(4):956–963.

[37] Paknahad J, Sheshyekani K, Rachidi F, et al. Evaluation of lightning-induced currents on cables buried in a lossy dispersive ground[J]. IEEE Transactions on Electromagnetic Compatibility. 2014, 56(6): 1522–1529.

[38] Shi L, Qi Z, Zhou Y, et al. Reduced model for disturbance analysis of cable bundles[J]. High Power Laser and Particle Beams. 2013, 25(02):531–536.

[39] Lanoz M, Nucci C, Tesche F. Transmission line theory for field-to-transmission line coupling calculations[J]. Electromagnetics. 1988, 8(2-4):171–211.

[40] Paul C R. Analysis of multiconductor transmission lines [M]: John Wiley and Sons, 2007.

[41] Paul C R. Literal solutions for time-domain crosstalk on lossless transmission lines[J]. IEEE transactions on electromagnetic compatibility. 1992, 34(4):433–444.

[42] Baum C E. Low-and high-frequency solutions of the telegrapher equations for nonuniform multiconductor transmission lines[C]// IEEE. 2007 IEEE International Symposium on Electromagnetic Compatibility: IEEE, 2007: 1–14.

[43] Tesche F M, Ianoz M, Karlsson T. EMC analysis methods and computational models [M]: John Wiley and Sons, 1996.

[44] Haase H, Nitsch J, Steinmetz T. Transmission-line super theory: A new approach to an effective calculation of electromagnetic interactions[J]. Ursi Radio Science Bulletin. 2017, 76(4):33–60.

[45] Haase H, Steinmetz T, Nitsch J. Effects of nonuniform cables on the propagation and coupling processes at high frequencies[C]// Citeseer. Proceedings of the international Conference on Electromagnetics in Advanced Applications: Citeseer, 2001.

[46] Taylor C D, Satterwhite R, Harrison C W. The Response of Terminated Two-wire Transmission Line Excited by Nonuniform Electromagnetic Field [M]: Sandia Corporation, 1965.

[47] Agrawal A K, Price H J, Gurbaxani S H. Transient response of multiconductor transmission lines excited by a nonuniform electromagnetic field[J]. IEEE Transactions on electromagnetic compatibility. 1980, 18(2):119–129.

[48] Rachidi F. Formulation of the field-to-transmission line coupling equations in terms of magnetic excitation field[J]. IEEE Transactions on Electromagnetic Compatibility. 1993, 35(3):404–407.

[49] Pillage L T, Rohrer R A. Asymptotic waveform evaluation for timing analysis[J]. IEEE Transactions on Computer-Aided Design of Integrated Circuits and Systems. 1990, 9(4):352–366.

[50] Celik M, Cangellaris A C. Efficient transient simulation of lossy packaging interconnects using moment-matching techniques[J]. IEEE Transactions on Components, Packaging, and Manufacturing Technology: Part B. 1996, 19(1):64–73.

[51] Chiprout E, Nakhla M S. Analysis of interconnect networks using complex frequency hopping (cfh)[J]. IEEE Transactions on Computer-Aided Design of Integrated Circuits and Systems. 1995, 14(2):186–200.

[52] Feldmann P, Freund R W. Efficient linear circuit analysis by padé approximation via the lanczos process[J]. IEEE Transactions on Computer-Aided Design of Integrated Circuits and Systems. 1995, 14(5):639–649.

[53] Yee K. Numerical solution of initial boundary value problems involving maxwell's equations in isotropic media[J]. IEEE Transactions on antennas and propagation. 1966, 14(3):302–307.

[54] Theethayi N, Baba Y, Rachidi F, et al. On the choice between transmission line equations and full-wave maxwell's equations for transient analysis of buried wires[J]. IEEE Transactions on Electromagnetic Compatibility. 2008, 50(2):347–357.

[55] Theethayi N, Thottappillil R, Paolone M, et al. External impedance and admittance of buried horizontal wires for transient studies using transmission line analysis[J]. IEEE Transactions on Dielectrics and Electrical Insulation. 2007, 14(3):751–761.

[56] Zhang B, Zou J, Du X, et al. Ground admittance of an underground insulated conductor and its characteristic in lightning induced disturbance problems[J]. IEEE Transactions on Electromagnetic Compatibility. 2016, 59(3):894–901.

[57] Yinghui Z, Lihua S, Cheng G. A time-domain method to calculate emp coupling of buried cables based on transmission line model[J]. High Power Laser and Particle Beams. 2006, 18(7):1166.

[58] Hamm J, Renn F, Hess O. Dispersive media subcell averaging in the fdtd method using corrective surface currents[J]. IEEE Transactions on Antennas and Propagation. 2013, 62(2):832–838.

[59] Baum C E. Extension of the blt equation into time domain[J]. Interaction Note. 1999, 553:211–216.

[60] Tesche F M. Development and use of the blt equation in the time domain as applied to a coaxial cable[J]. IEEE transactions on electromagnetic compatibility. 2007, 49(1):3–11.

[61] Tesche F M. On the analysis of a transmission line with nonlinear terminations using the time-dependent blt equation[J]. IEEE Transactions on Electromagnetic Compatibility. 2007, 49(2):427–433.

[62] Antonini G, De Camillis L. Time-domain green's function-based sensitivity analysis of multiconductor transmission lines with nonlinear terminations[J]. IEEE Microwave and Wireless Components Letters. 2009, 19(7):428–430.

[63] Grivet-Talocia S, Huang H M, Ruehli A E, et al. Transient analysis of lossy transmission lines: An efficient approach based on the method of characteristics[J]. IEEE Transactions on Advanced Packaging. 2004, 27(1):45–56.

[64] Elfadel I M, Huang H M, Ruehli A E, et al. A comparative study of two transient analysis algorithms for lossy transmission lines with frequency-dependent data[J]. IEEE transactions on advanced packaging. 2002, 25(2):143–153.

[65] Kuznetsov D B, Schutt-Ainé J E. Optimal transient simulation of transmission lines[J]. IEEE Transactions on Circuits and Systems I: Fundamental Theory and Applications. 1996, 43(2):110–121.

[66] Erdin I, Dounavis A, Achar R, et al. A spice model for incident field coupling to lossy multiconductor transmission lines[J]. IEEE Transactions on Electromagnetic Compatibility. 2001, 43(4):485–494.

[67] Dounavis A, Achar R, Nakhla M S. Efficient passive circuit models for distributed networks with frequency-dependent parameters[J]. IEEE Transactions on Advanced Packaging. 2000, 23(3):382–392.

[68] Nakhla N M, Dounavis A, Achar R, et al. Depact: Delay extraction-based passive compact transmission-line macromodeling algorithm[J]. IEEE Transactions on Advanced Packaging. 2005, 28(1):13–23.

[69] Liu X, Cui X, Qi L. Calculation of lightning-induced overvoltages on overhead lines based on depact macromodel using circuit simulation software[J]. IEEE Transactions on Electromagnetic Compatibility. 2011, 54(4):837–849.

[70] Paul C R. A spice model for multiconductor transmission lines excited by an incident electromagnetic field[J]. IEEE Transactions on Electromagnetic Compatibility. 1994, 36(4):342–354.

[71] Maio I, Canavero F G, Dilecce B. Analysis of crosstalk and field coupling to lossy mtls in a spice environment[J]. IEEE Transactions on Electromagnetic Compatibility. 1996, 38(3):221–229.

[72] Paul C R. Solution of the transmission-line equations under the weak-coupling assumption[J]. IEEE Transactions on Electromagnetic compatibility. 2002, 44(3):413–423.

[73] Roy S, Beygi A, Dounavis A. Electromagnetic interference analysis of multiconductor transmission line networks using longitudinal partitioning-based waveform relaxation algorithm[J]. IEEE transactions on electromagnetic compatibility. 2012, 55(2):395–406.

[74] Achar R, Nakhla M S, Dhindsa H S, et al. Parallel and scalable transient simulator for power grids via waveform relaxation (pts-pwr)[J]. IEEE Transactions on Very Large Scale Integration (VLSI) Systems. 2009, 19(2):319–332.

[75] Nakhla N M, Ruehli A E, Nakhla M S, et al. Simulation of coupled interconnects using waveform relaxation and transverse partitioning[J]. IEEE Transactions on Advanced Packaging. 2006, 29(1): 78–87.

[76] Nakhla N, Ruehli A E, Nakhla M S, et al. Waveform relaxation techniques for simulation of coupled interconnects with frequency-dependent parameters[J]. IEEE Transactions on Advanced Packaging. 2007, 30(2):257–269.

[77] Xie Y Z, Canavero F, Maestri T, et al. Crosstalk analysis of multiconductor transmission lines based on distributed analytical representation and iterative technique[J]. IEEE Transactions on Electromagnetic Compatibility. 2010, 52(3):712–727.

[78] Xie Y z, Guo J, Canavero F G. Analytic iterative solution of electromagnetic pulse coupling to multiconductor transmission lines[J]. IEEE transactions on electromagnetic compatibility. 2013, 55 (3):451–466.

[79] Guo J, Xie Y z, Canavero F G. Gauss–seidel iterative solution of electromagnetic pulse coupling to three-conductor transmission lines[J]. IEEE Transactions on Electromagnetic Compatibility. 2014, 57(2):292–298.

[80] Guo J, Xie Y z, Qiu A c. Jor iterative method for the modeling of mtls excited by emp[J]. IEEE Antennas and Wireless Propagation Letters. 2015, 15:536–539.

[81] Guo J, Xie Y z. An efficient model of transient electromagnetic field coupling to multiconductor transmission lines based on analytical iterative technique in time domain[J]. IEEE Transactions on Microwave Theory and Techniques. 2018, 66(6):2663–2673.

[82] Chang F Y. The generalized method of characteristics for waveform relaxation analysis of lossy coupled transmission lines[J]. IEEE Transactions on Microwave Theory and Techniques. 1989, 37 (12):2028–2038.

[83] Grivet-Talocia S, Canavero F G. Topline: a delay-pole-residue method for the simulation of lossy and dispersive interconnects[C]. 2002 IEEE 11th Topical Meeting on Electrical Performance of Electronic Packaging, 2002: 359-362.

[84] Charest A, Achar R, Nakhla M, et al. Delay extraction-based passive macromodeling techniques for transmission line type interconnects characterized by tabulated multiport data[J]. Analog Integrated Circuits and Signal Processing. 2009, 60(1-2):13–25.

[85] Dounavis A, Pothiwala V A. Passive closed-form transmission line macromodel using method of characteristics[J]. IEEE Transactions on Advanced Packaging. 2008, 31(1):190–202.

[86] Celik M, Cangellaris A C, Yaghnour A. An all-purpose transmission-line model for interconnect simulation in spice[J]. IEEE transactions on microwave theory and techniques. 1997, 45(10):1857–1867.

[87] Cangellaris A C, Pasha S, Prince J L, et al. A new discrete transmission line model for passive model order reduction and macromodeling of high-speed interconnections[J]. IEEE Transactions on Advanced Packaging. 1999, 22(3):356–364.

[88] Gustavsen B, Semlyen A. Rational approximation of frequency domain responses by vector fitting[J]. IEEE Transactions on power delivery. 1999, 14(3):1052–1061.

[89] Triverio P, Grivet-Talocia S, Nakhla M S, et al. Stability, causality, and passivity in electrical interconnect models[J]. IEEE Transactions on Advanced Packaging. 2007, 30(4):795–808.

[90] Yu Q, Wang J M L, Kuh E S. Passive multipoint moment matching model order reduction algorithm on multiport distributed interconnect networks[J]. IEEE Transactions on Circuits and Systems I: Fundamental Theory and Applications. 1999, 46(1):140–160.

[91] Erdin I, Dounavis A, Achar R, et al. Circuit simulation of incident field coupling to multiconductor transmission lines with frequency-dependent losses[C]// IEEE. 2001 IEEE EMC International Symposium. Symposium Record. International Symposium on Electromagnetic Compatibility (Cat. No. 01CH37161): volume 2: IEEE, 2001: 1084–1087.

[92] Gao Y H, Lai Z F, Liu X M, et al. Research on very fast transient over-voltages distribution in large power transformer windings[J]. Advanced Materials Research. 2012, 433-440:7287–7292.

[93] Wang Z J, Yang Y. Calculation of very fast transient overvoltage distributions in large power transformer windings[J]. High Voltage Engineering. 2010, 04:104–111.

[94] Gupta S C, Singh B. Determination of the impulse voltage distribution in windings of large power transformers[J]. Electric Power Systems Research. 1992, 25(3):183–189.

[95] Wang Y, Chen W, Wang C, et al. A hybrid model of transformer windings for very fast transient analysis based on quasi-stationary electromagnetic fields[J]. Electric Power Components and Systems. 2008, 36(5):540–554.

[96] Gutierrez M, Degeneff R, McKenny P, et al. Linear, lumped parameter transformer model reduction technique[J]. IEEE transactions on power delivery. 1995, 10(2):853–861.

[97] Wang Z. A model for transient analysis in large transformer windings[J]. Journal of Tsinghua University. 1993, 33(1):25–32.

[98] Shibuya Y, Fujita S, Tamaki E. Analysis of very fast transients in transformers[J]. IEE Proceedings-Generation, Transmission and Distribution. 2001, 148(5):377–383.

[99] Ying P, Jiangjun R. Investigation of very fast transient overvoltage distribution in taper winding of tesla transformer[J]. IEEE Transactions on Magnetics. 2006, 42(3):434–441.

[100] Roden J A, Paul C R, Smith W T, et al. Finite-difference, time-domain analysis of lossy transmission lines[J]. IEEE transactions on electromagnetic compatibility. 1996, 38(1):15–24.

[101] Dou L, Wang Z q. Application of lax-wendroff difference method to the analysis of high-speed interconnect transmission lines[J]. Information and Control. 2005, 34(6):724.

[102] Zanji W. Modeling for simulating very fast transient in transformer windings[J]. Chinese Society for Electrical Engineering. 1996, 5.

[103] Liang G, Sun H, Zhang X, et al. Modeling of transformer windings under very fast transient over-voltages[J]. IEEE Transactions on electromagnetic compatibility. 2006, 48(4):621–627.

[104] Liang G, Zhang X, Wang X, et al. Research on high-frequency circuit model of transformer windings in vfto[C]. Zhongguo Dianji Gongcheng Xuebao(Proceedings of the Chinese Society of Electrical Engineering): volume 26, 2006: 144–148.

[105] Pothiwala V, Dounavis A. An efficient closed form macromodeling algorithm using method of characteristics for lossy multiconductor transmission lines[C]// IEEE. 2006 IEEE Electrical Performane of Electronic Packaging: IEEE, 2006: 203–206.

[106] Lin S, Kuh E S. Transient simulation of lossy interconnects based on the recursive convolution formulation[J]. IEEE Transactions on Circuits and Systems I: Fundamental Theory and Applications. 1992, 39(11):879–892.

[107] Semlyen A, Dabuleanu A. Fast and accurate switching transient calculations on transmission lines with ground return using recursive convolutions[J]. IEEE Transactions on Power Apparatus and Systems. 1975, 94(2):561–571.

[108] Grivet-Talocia S, Maio I, Canavero F. Recent advances in reduced-order modeling of complex interconnects[C]// IEEE. IEEE 10th Topical Meeting on Electrical Performance of Electronic Packaging (Cat. No. 01TH8565): IEEE, 2001: 243–246.

[109] M.Rabaey J. The Spice Page[M/OL]. 2010. `http://bwrcs.eecs.berkeley.edu/Classes/IcBook/SPICE/`.

[110] PSpice Reference Guide, 2nd ed. [M]: Cadence Design Systems, Inc., 2000: 191–236.

[111] Bayadi A, Harid N, Zehar K, et al. Simulation of metal oxide surge arrester dynamic behavior under fast transients[C]. International conference on power systems transients, IPST, 2003.

[112] Chen H, Du Y p. A comprehensive study on the nonlinear behavior of metal oxide varistors[C]// IEEE. 2016 33rd International Conference on Lightning Protection (ICLP): IEEE, 2016: 1–5.

[113] Zola J G. Simple model of metal oxide varistor for pspice simulation[J]. IEEE Transactions on computer-aided design of integrated circuits and Systems. 2004, 23(10):1491–1494.

[114] Chen C T. Linear system theory and design [M]: Oxford University Press, Inc., 1998.

[115] Hohn F E. Elementary matrix algebra [M]: Courier Corporation, 2013.

[116] Ralston A, Rabinowitz P. A first course in numerical analysis [M]: Courier Corporation, 2001.

[117] Nakhla N, Nakhla M, Achar R. Simplified delay extraction-based passive transmission line macromodeling algorithm[J]. IEEE Transactions on Advanced Packaging. 2010, 33(2):0–509.

[118] Weinberg L. Network analysis and synthesis: volume 17 [M]: McGraw-Hill New York, 1962.

[119] Dweck E E. Theory of linear active networks[J]. Electronics and power. 1968, 14(7):298.

[120] Dounavis A, Li X. Passive closed-form transmission-line model for general-purpose circuit simulators[J]. IEEE Transactions on Microwave Theory and Techniques. 1999, 47(12):2450–2459.

[121] Du Z, Xie Y z, Canavero F G. A spice-compatible macromodel for field coupling to multiconductor transmission lines based on the analog behavioral modeling[J]. IEEE Transactions on Electromagnetic Compatibility. 2019, 61(6):1884–1890.

[122] Du Z, Xie Y z. A spice model for incident field coupling to lossy overhead transmission line[C]. 2017 7th IEEE International Symposium on Microwave, Antenna, Propagation, and EMC Technologies (MAPE), 2017: 187-190.

[123] Fontaine J, Umbert A, Djebari B, et al. Ground effects in the response of a single-wire transmission line illuminated by an emp[J]. Electromagnetics. 1982, 2(1):43–54.

[124] D'Amore M, Sarto M S. Simulation models of a dissipative transmission line above a lossy ground for a wide-frequency range. i. single conductor configuration[J]. IEEE Transactions on Electromagnetic Compatibility. 1996, 38(2):127–138.

[125] Xie Y, Wang Z, Sun B, et al. High-altitude electromagnetic pulse environment over the lossy ground[J]. High Power Laser and Particle Beams. 2003, 15(7):680–684.

[126] Carson J R. Wave propagation in overhead wires with ground return[J]. Bell Labs Technical Journal. 1926, 5(4):539–554.

[127] Vance E F. Coupling to shielded cables [M]: Wiley New York, 1978.

[128] Sunde E D. Earth conduction effects in transmission systems for sunde erling d[J]. Students Quarterly Journal. 1949, 20(78):92.

[129] Wait J R. Theory of wave propagation along a thin wire parallel to an interface[J]. Radio Science. 2016, 7(6):675–679.

[130] Semlyen A. Ground return parameters of transmission lines an asymptotic analysis for very high frequencies[J]. IEEE Transactions on Power Apparatus and Systems. 1981, PAS-100(3):1031–1038.

[131] Chen K. Time harmonic solutions for a long horizontal wire over the ground with grazing incidence[J]. IEEE transactions on antennas and propagation. 1985, 33(3):233–243.

[132] D'Amore M, Sarto M. A new formulation of lossy ground return parameters for transient analysis of multiconductor dissipative lines[J]. IEEE Transactions on Power Delivery. 1997, 12(1):303–314.

[133] Rachidi F, Nucci C, Ianoz M, et al. Influence of a lossy ground on lightning-induced voltages on overhead lines[J]. IEEE Transactions on Electromagnetic Compatibility. 1996, 38(3):250–264.

[134] Rachidi F, Nucci C A, Ianoz M. Transient analysis of multiconductor lines above a lossy ground[J]. IEEE Transactions on Power Delivery. 1999, 14(1):294–302.

[135] Huo Y, Zhao Y, Li Z. A fast equivalent method for modeling electromagnetic pulse response of cable bundle terminated in arbitrary loads[J]. Progress In Electromagnetics Research. 2017, 53:177–190.

[136] Baum C E, Liu T K, Tesche F M. On the analysis of general multiconductor transmission-line networks[J]. Interaction Note. 1978, 350(6):467–547.

[137] Xie H, Du T, Zhang M, et al. Theoretical and experimental study of effective coupling length for transmission lines illuminated by hemp[J]. IEEE transactions on electromagnetic compatibility. 2015, 57(6):1529–1538.

[138] Papadopoulos T A, Tsiamitros D A, Papagiannis G K. Impedances and admittances of underground cables for the homogeneous earth case[J]. IEEE transactions on power delivery. 2010, 25(2):961–969.

[139] Papadopoulos T, Chrysochos A, Papagiannis G. Comparison of earth return approaches on modeling of underground cables[C]// IEEE. 45th International Universities Power Engineering Conference UPEC2010: IEEE, 2010: 1–5.

[140] Du Z, Xie Y z, Ning D, et al. A spice-compatible macromodel for field coupling to underground transmission lines based on the analog behavioral modeling[J]. IEEE Transactions on Electromagnetic Compatibility. 2019, 1-10.

[141] Du Z, Xie Y z. Transient response of overhead and buried multiconductor lines to hemp[J]. High Power Laser and Particle Beams. 2019, 31(07):31070003.

[142] Schelkunoff S A. The electromagnetic theory of coaxial transmission lines and cylindrical shields[J]. Bell system technical journal. 1934, 13(4):532–579.

[143] Wedepohl L, Wilcox D. Transient analysis of underground power-transmission systems. system-model and wave-propagation characteristics[C]// IET. Proceedings of the institution of electrical engineers: volume 120: IET, 1973: 253–260.

[144] Wait J R. Electromagnetic wave propagation along a buried insulated wire[J]. Canadian journal of physics. 1972, 50(20):2402–2409.

[145] Papagiannis G, Tsiamitros D, Labridis D, et al. Direct numerical evaluation of earth return path impedances of underground cables[J]. IEE Proceedings-Generation, Transmission and Distribution. 2005, 152(3):321–327.

[146] Theethayi N. Electromagnetic interference in distributed outdoor electrical systems, with an emphasis on lightning interaction with electrified railway network [D]: Institutionen för teknikvetenskaper, 2005.

[147] Du Z, Xie Y z, Canavero F G. A spice-compatible macromodel for field coupling to multiconductor transmission lines based on the analog behavioral modeling[J]. IEEE Transactions on Electromagnetic Compatibility. 2018.

[148] Xie H, Wang J, Fan R, et al. Spice models to analyze radiated and conducted susceptibilities of shielded coaxial cables[J]. IEEE Transactions on electromagnetic compatibility. 2010, 52(1):215–222.

[149] Yu Y, Zanji W, Chong S. A circuit model in a wide frequency range for power transformer and analysis of its characteristics[C]// IEEE. 2009 Asia-Pacific Power and Energy Engineering Conference: IEEE, 2009: 1–5.

[150] Zhang X. Time Domain Simulation Calculatin and Experimental Research on the Effect of VFTO on Power Transformers [D]: North China Electric Power University, 2008.

[151] Newcomb R W. Linear multiport synthesis [M]: McGraw-Hill, 1966.

[152] Harville D A. Matrix algebra from a statistician's perspective [M]: Taylor and Francis Group, 1998.

Appendix A   Proof of Theorem

Converting (2-1)-(2-5) to the expression of Y-parameters, the congruent transform matrices are expressed as

$$\begin{bmatrix} \mathbf{I}(0) \\ \mathbf{I}(l) \end{bmatrix} = \begin{bmatrix} \mathbf{Y}_{11} & \mathbf{Y}_{12} \\ \mathbf{Y}_{21} & \mathbf{Y}_{22} \end{bmatrix} \begin{bmatrix} \mathbf{V}(0) \\ \mathbf{V}(l) \end{bmatrix}; \quad \begin{bmatrix} \mathbf{Y}_{11} & \mathbf{Y}_{12} \\ \mathbf{Y}_{21} & \mathbf{Y}_{22} \end{bmatrix} = \psi_1 + \psi_2 \tag{A-1}$$

$$\psi_1(s) = \frac{1}{2}\mathbf{W}_1^T \begin{bmatrix} \mathbf{H}_1(s) & \mathbf{0} \\ \mathbf{0} & \mathbf{0} \end{bmatrix} \mathbf{W}_1; \quad \psi_2(s) = \frac{1}{2}\mathbf{W}_2^T \begin{bmatrix} \mathbf{H}_2(s)^{-1} & \mathbf{0} \\ \mathbf{0} & \mathbf{0} \end{bmatrix} \mathbf{W}_2 \tag{A-2}$$

where

$$\mathbf{W}_1 = \begin{bmatrix} \mathbf{E}_n & -\mathbf{E}_n \\ \mathbf{0} & \mathbf{E}_n \end{bmatrix}; \quad \mathbf{W}_2 = \begin{bmatrix} \mathbf{E}_n & \mathbf{E}_n \\ \mathbf{0} & \mathbf{E}_n \end{bmatrix} \tag{A-3}$$

$$\mathbf{H}_1(s) = \mathbf{Z}_\mathbf{C}^{-1}(s)(\mathbf{E}_n - \mathbf{H}(s))^{-1}(\mathbf{E}_n + \mathbf{H}(s)) \tag{A-4a}$$

$$\mathbf{H}_2(s) = (\mathbf{E}_n - \mathbf{H}(s))^{-1}(\mathbf{E}_n + \mathbf{H}(s))\mathbf{Z}_\mathbf{C}(s) \tag{A-4b}$$

Since $\mathbf{H}(s)$ and $\mathbf{Z}_\mathbf{C}(s)$ are acquired from equations (2-3)-(2-5), then the macromodel will always satisfy the first condition of $\mathbf{Y}(s^*) = \mathbf{Y}^*(s)$. To prove $\mathbf{Y}(s)$ is positive real and analytic (condition 2 and 3 of passivity definition), the $\mathbf{Y}^T(s^*) + \mathbf{Y}(s)$ is expressed as

$$\mathbf{Y}^T(s^*) + \mathbf{Y}(s) = (\psi_1^T(s^*) + \psi_1(s)) + (\psi_2^T(s^*) + \psi_2(s)) \tag{A-5}$$

where

$$\psi_1^T(s^*) + \psi_1(s) = \frac{1}{2}\mathbf{W}_1^T \begin{bmatrix} \mathbf{H}_1(s^*) + \mathbf{H}_1(s) & \mathbf{0} \\ \mathbf{0} & \mathbf{0} \end{bmatrix} \mathbf{W}_1 \tag{A-6a}$$

$$\psi_2^T(s^*) + \psi_2(s) = \frac{1}{2}\mathbf{W}_2^T \begin{bmatrix} \mathbf{H}_2(s^*)^{-1} + \mathbf{H}_2(s)^{-1} & \mathbf{0} \\ \mathbf{0} & \mathbf{0} \end{bmatrix} \mathbf{W}_2 \tag{A-6b}$$

It is obvious that if $\mathbf{H}_1(s)$ and $\mathbf{H}_2(s)$ are positive real then the matrices $\psi_1(s)$ and $\psi_2(s)$ are also positive real, since they are expressed in terms of congruence transformations of positive real functions[151, 152]. Thus, it requires to show that $\mathbf{H}_1(s)$ and $\mathbf{H}_2(s)$ are positive real functions to prove the passivity of the proposed macromodel. Hence, the condition of theorem above is utilized. Let $\mathbf{\Gamma}(s)l$ be expressed in terms of values and eigenvectors as

$$\mathbf{\Gamma}(s)l = \mathbf{V}_P(s)\mathbf{\Lambda}_P(s)\mathbf{V}_P^{-1}(s) \tag{A-7}$$

where $\mathbf{V}_P(s)$ and $\mathbf{\Lambda}_P(s)$ are the eigenvectors and eigenvalues of $\mathbf{\Gamma}(s)l$, respectively. Let the diagonal matrix $\mathbf{\Lambda}_P(s)$ be expressed as

$$\mathbf{\Lambda}_P(s) = \mathbf{A}_P + j\mathbf{B}_P \tag{A-8}$$

where $\mathbf{A}_P = diag(a_{p1}, ..., a_{pn})$ and $\mathbf{B}_P = diag(b_{p1}, ..., b_{pn})$ are the real and imaginary parts of $\mathbf{\Lambda}_P(s)$, respectively. Since the parameters $\mathbf{R}(s) + s\mathbf{L}(s)$ and $\mathbf{G}(s) + s\mathbf{C}(s)$ satisfy the condition of theorem, the propagation function $\mathbf{\Gamma}(s)$ and the characteristic impedance matrix $\mathbf{Z_C}(s)$ expressed in (2-4)-(2-5) must also be positive real function. Then $\mathbf{A}_P$ is a positive real for any complex value of $s = \sigma + j\omega$ satisfying $\sigma > 0$. Next, transform the $l\mathbf{\Gamma}(s)\mathbf{Z_C^{-1}}(s)$ and $(l\mathbf{\Gamma}(s))^{-1}\mathbf{Z_C^{-1}}(s)$ as

$$\mathbf{V}_P^{-1}(s)(l\mathbf{\Gamma}(s)\mathbf{Z_C^{-1}}(s))(\mathbf{V}_P^{-1}(s))^{*T} \tag{A-9}$$

$$\mathbf{V}_P^{-1}(s)((l\mathbf{\Gamma}(s))^{-1}\mathbf{Z_C^{-1}}(s))(\mathbf{V}_P^{-1}(s))^{*T} \tag{A-10}$$

Since $\mathbf{\Gamma}(s)\mathbf{Z_C^{-1}}(s) = \mathbf{G}(s) + s\mathbf{C}(s)$ and $\mathbf{Z_C}(s)\mathbf{\Gamma}(s) = \mathbf{R}(s) + s\mathbf{L}(s)$ are positive real (condition in theorem), then (A-9) and (A-10) are also positive real since the inverse of a positive real function is positive real and both (A-9) and (A-10) are expressed in terms of a congruent transformation of a positive real functions[151, 152]. Substituting (A-7) into (A-9) yields

$$\mathbf{V}_P^{-1}(s)(\mathbf{V}_P(s)\mathbf{\Lambda}_P(s)\mathbf{V}_P^{-1}(s)\mathbf{Z_C^{-1}}(s))(\mathbf{V}_P^{-1}(s))^{*T} = \mathbf{\Lambda}_P(s)\widetilde{\mathbf{Z}}_\mathbf{C}(s) \tag{A-11}$$

Similarly, substituting (A-7) to (A-10) yields

$$\mathbf{V}_P^{-1}(s)((\mathbf{V}_P(s)\mathbf{\Lambda}_P(s)\mathbf{V}_P^{-1}(s))^{-1}\mathbf{Z_C^{-1}}(s))(\mathbf{V}_P^{-1}(s))^{*T} = \mathbf{\Lambda}_p^{-1}(s)\widetilde{\mathbf{Z}}_\mathbf{C}(s) \tag{A-12}$$

where $\widetilde{\mathbf{Z}}_\mathbf{C}(s)$ is defined in terms of a congruent transformation of a positive real function $\mathbf{Z_C}(s)$ as

$$\widetilde{\mathbf{Z}}_\mathbf{C}(s) = \mathbf{V}_P^{-1}(s)\mathbf{Z_C^{-1}}(s)(\mathbf{V}_P^{-1}(s))^{*T} = \mathbf{A}_Z + j\mathbf{B}_Z \tag{A-13}$$

in which $\mathbf{A}_Z$ and $\mathbf{B}_Z$ are the real and imaginary parts of $\widetilde{\mathbf{Z}}_\mathbf{C}(s)$, respectively. Using (A-13) and the fact that (A-8) is a diagonal matrix, (A-11) and (A-12) can also be expressed in terms of real and imaginary parts as

$$\boldsymbol{\Lambda}_P(s)\widetilde{\mathbf{Z}}_{\mathbf{C}}(s) = (\mathbf{A}_P\mathbf{A}_Z - \mathbf{B}_P\mathbf{B}_Z) + j(\mathbf{B}_P\mathbf{A}_Z + \mathbf{A}_P\mathbf{B}_Z) \tag{A-14}$$

$$\boldsymbol{\Lambda}_p^{-1}(s)\widetilde{\mathbf{Z}}_{\mathbf{C}}(s) = (\mathbf{A}_P^2 + \mathbf{B}_P^2)^{-1}((\mathbf{A}_P\mathbf{A}_Z + \mathbf{B}_P\mathbf{B}_Z) + j(-\mathbf{B}_P\mathbf{A}_Z + \mathbf{A}_P\mathbf{B}_Z)) \tag{A-15}$$

Since (A-14) and (A-15) are positive real functions and $\mathbf{A}_P$ is a positive real and diagonal matrix, then the following inequalities hold:

$$z^{*T}(\mathbf{A}_P\mathbf{A}_Z - \mathbf{B}_P\mathbf{B}_Z)z \geq 0 \tag{A-16a}$$

$$z^{*T}(\mathbf{A}_P\mathbf{A}_Z + \mathbf{B}_P\mathbf{B}_Z)z \geq 0 \tag{A-16b}$$

$$z^{*T}(\mathbf{A}_Z \pm \left|\mathbf{A}_P^{-1}\mathbf{B}_P\right|\mathbf{B}_Z)z \geq 0 \tag{A-16c}$$

where z is any arbitrary complex vector. Since $\mathbf{H}(s) = e^{-\boldsymbol{\Gamma}(s)l}$ is a function of $l\boldsymbol{\Gamma}(s)$, the eigen-decomposition in (A-7) can also be used to diagonalize $\mathbf{H}(s)$ as

$$\mathbf{H}(s) = \mathbf{V}_P(s)\boldsymbol{\Lambda}_H(s)\mathbf{V}_P^{-1}(s) \tag{A-17}$$

where $\mathbf{V}_P(s)$ is the same eigenvectors in (A-7) and $\boldsymbol{\Lambda}_H(s)$ is the eigenvalues of $\mathbf{H}(s)$. And the relationship of the eigenvalues between $\boldsymbol{\Lambda}_P(s)$ and $\boldsymbol{\Lambda}_H(s)$ are

$$\boldsymbol{\Lambda}_P(s) = diag(\lambda_1, \lambda_2, ..., \lambda_n) \tag{A-18a}$$

$$\boldsymbol{\Lambda}_H(s) = diag(e^{\lambda_1}, e^{\lambda_2}, ..., e^{\lambda_n}) \tag{A-18b}$$

Let $\boldsymbol{\Lambda}_H(s)$ be

$$\boldsymbol{\Lambda}_H(s) = \mathbf{A}_H + j\mathbf{B}_H \tag{A-19}$$

Where $\mathbf{A}_H = diag(a_{H1}, a_{H2}, ..., a_{Hn})$ and $\mathbf{B}_H = diag(b_{H1}, b_{H2}, ..., b_{Hn})$ are the real and imaginary parts of $\boldsymbol{\Lambda}_H(s)$. It can be proved that the exponential function $e^{-s} = e^{-\sigma}(\cos\omega - j\sin\omega)$ satisfies the following inequalities as follows for all $\sigma > 0$

$$\left|\frac{2e^{-\sigma}\cos\omega}{1 - e^{-2\sigma}}\right| = \left|\frac{\cos\omega}{(e^\sigma - e^{-\sigma})/2}\right| \leq \left|\frac{1}{(e^\sigma - e^{-\sigma})/2}\right| \leq \left|\frac{1}{\sigma}\right| \tag{A-20a}$$

$$\left|\frac{2e^{-\sigma}\sin\omega}{1 - e^{-2\sigma}}\right| = \left|\frac{\sin\omega}{(e^\sigma - e^{-\sigma})/2}\right| \leq \left|\frac{\omega}{\sigma}\right| \tag{A-20b}$$

$$(e^{-\sigma}\cos\omega)^2 + (e^{-\sigma}\sin\omega)^2 = e^{-2\sigma} \leq 1 \tag{A-20c}$$

Hence, each diagonal element of $\boldsymbol{\Lambda}_H(s)$ will also satisfy conditions similar to (A-20):

$$\left| \frac{2a_{Hi}}{1 - a_{Hi}^2 - b_{Hi}^2} \right| \leq \left| \frac{1}{a_{pi}} \right| \tag{A-21a}$$

$$\left| \frac{2b_{Hi}}{1 - a_{Hi}^2 - b_{Hi}^2} \right| \leq \left| \frac{b_{pi}}{a_{pi}} \right| \tag{A-21b}$$

$$a_{Hi}^2 + b_{Hi}^2 \leq 1 \tag{A-21c}$$

where the index i ranges from 1 to n corresponding to the number of lines. In order to prove $\mathbf{H}_1(s)$ is a positive real function, making the same transformation of (A-11) and (A-12) on $\mathbf{H}_1(s)$ as

$$\mathbf{V}_P^{-1}(s)\mathbf{H}_1(s)(\mathbf{V}_P^{-1}(s))^{*T} = \mathbf{V}_P^{-1}(s)\mathbf{Z}_{\mathbf{C}}^{-1}(s)(\mathbf{E}_n - \mathbf{H}(s))^{-1}(\mathbf{E}_n + \mathbf{H}(s))(\mathbf{V}_P^{-1}(s))^{*T}$$
$$= (\mathbf{E}_n - \mathbf{\Lambda}_H(s))^{-1}(\mathbf{E}_n + \mathbf{\Lambda}_H(s))\mathbf{Z}_{\mathbf{C}}^{-1}(s) \tag{A-22}$$

Let $(\mathbf{E}_n - \mathbf{\Lambda}_H(s))^{-1}(\mathbf{E}_n + \mathbf{\Lambda}_H(s))$ be

$$(\mathbf{E}_n - \mathbf{\Lambda}_H(s))^{-1}(\mathbf{E}_n + \mathbf{\Lambda}_H(s)) = \mathbf{A}_{H1} + j\mathbf{B}_{H1} \tag{A-23}$$

Substituting (A-13) and (A-23) into (A-22) yields

$$(\mathbf{E}_n - \mathbf{\Lambda}_H(s))^{-1}(\mathbf{E}_n + \mathbf{\Lambda}_H(s))\mathbf{Z}_{\mathbf{C}}^{-1}(s) = (\mathbf{A}_{H1}\mathbf{A}_Z - \mathbf{B}_{H1}\mathbf{B}_Z) + j(\mathbf{B}_{H1}\mathbf{A}_Z - \mathbf{A}_{H1}\mathbf{B}_Z) \tag{A-24}$$

It is obvious that $\mathbf{A}_{H1}$ is a diagonal positive real function. To prove $\mathbf{H}_1(s)$ is positive real requires that (A-24) is positive real. Therefore, (A-24) must satisfy

$$z^{*T}(\mathbf{A}_{H1}\mathbf{A}_Z - \mathbf{B}_{H1}\mathbf{B}_Z)z \geq 0 \tag{A-25a}$$

$$z^{*T}(\mathbf{A}_Z - \mathbf{A}_{H1}^{-1}\mathbf{B}_{H1}\mathbf{B}_Z)z \geq 0 \tag{A-25b}$$

Comparing (A-16) and (A-25) reveals that $\mathbf{H}_1(s)$ is positive real if

$$\left| \mathbf{A}_P^{-1}\mathbf{B}_P \right| \geq \left| \mathbf{A}_{H1}^{-1}\mathbf{B}_{H1} \right| \tag{A-26}$$

Using (A-8) and (A-19), $\left| \mathbf{A}_P^{-1}\mathbf{B}_P \right|$ is defined as

$$\left| \mathbf{A}_P^{-1}\mathbf{B}_P \right| = diag(k_{p1}, k_{p2}, ..., k_{pn}) \tag{A-27}$$

in which $k_{pi} = \left| \frac{b_{pi}}{a_{pi}} \right|$. Similarly, $\left| \mathbf{A}_{H1}^{-1}\mathbf{B}_{H1} \right|$ can also be defined as

$$\left| \mathbf{A}_{H1}^{-1}\mathbf{B}_{H1} \right| = diag(k_{H1}, k_{H2}, ..., k_{Hn}) \tag{A-28}$$

in which

$$k_{Hi} = \left| \frac{2b_{Hi}}{1 - a_{Hi}^2 - b_{Hi}^2} \right| \quad \text{(A-29)}$$

Since inequality condition of (A-21b) has been proved, the inequality (A-26) is true. Hence, the condition of theorem can ensure $\mathbf{H}_1(s)$ is positive real.

Then, to prove that $\mathbf{H}_2(s)^{-1}$ is positive real, a similar strategy is followed. The function $\mathbf{H}_2(s)^{-1}$ goes through the similar transformation and mathematical simplification yields

$$\mathbf{V}_P^{-1}(s)\mathbf{H}_2(s)^{-1}(\mathbf{V}_P^{-1}(s))^{*T} = (\mathbf{E}_n + \mathbf{\Lambda}_H(s))^{-1}(\mathbf{E}_n - \mathbf{\Lambda}_H(s))\mathbf{Z}_{\mathbf{C}}^{-1}(s) \quad \text{(A-30)}$$

Let $(\mathbf{E}_n + \mathbf{\Lambda}_H(s))^{-1}(\mathbf{E}_n - \mathbf{\Lambda}_H(s))$ be

$$(\mathbf{E}_n + \mathbf{\Lambda}_H(s))^{-1}(\mathbf{E}_n - \mathbf{\Lambda}_H(s)) = \mathbf{A}_{H2} + j\mathbf{B}_{H2} \quad \text{(A-31)}$$

Substituting (A-13) and (A-31) into (A-30) yields

$$(\mathbf{E}_n + \mathbf{\Lambda}_H(s))^{-1}(\mathbf{E}_n - \mathbf{\Lambda}_H(s))\mathbf{Z}_{\mathbf{C}}^{-1}(s) = (\mathbf{A}_{H2}\mathbf{A}_Z - \mathbf{B}_{H2}\mathbf{B}_Z) + j(\mathbf{B}_{H2}\mathbf{A}_Z + \mathbf{A}_{H2}\mathbf{B}_Z) \quad \text{(A-32)}$$

It is obvious that $\mathbf{A}_{H2}$ is a diagonal positive real function. To prove $\mathbf{H}_2(s)^{-1}$ is positive real requires that (A-32) is positive real. Therefore, (A-32) must satisfy

$$z^{*T}(\mathbf{A}_{H2}\mathbf{A}_Z - \mathbf{B}_{H2}\mathbf{B}_Z)z \geq 0 \quad \text{(A-33a)}$$

$$z^{*T}(\mathbf{A}_Z - \mathbf{A}_{H2}^{-1}\mathbf{B}_{H2}\mathbf{B}_Z)z \geq 0 \quad \text{(A-33b)}$$

Comparing (A-16) with (A-33) reveals that $\mathbf{H}_2(s)^{-1}$ is positive real if

$$\left| \mathbf{A}_P^{-1}\mathbf{B}_P \right| \geq \left| \mathbf{A}_{H2}^{-1}\mathbf{B}_{H2} \right| \quad \text{(A-34)}$$

$\left| \mathbf{A}_{H2}^{-1}\mathbf{B}_{H2} \right|$ can be defined as $\left| \mathbf{A}_{H2}^{-1}\mathbf{B}_{H2} \right| = diag(g_{H1}, g_{H2}, ..., g_{Hn})$, in which

$$g_{Hi} = \left| \frac{2b_{Hi}}{1 - a_{Hi}^2 - b_{Hi}^2} \right| \quad \text{(A-35)}$$

Since inequality condition of (A-21b) has been proved, the inequality (A-35) is true. Hence, the condition of theorem can ensure $\mathbf{H}_2(s)^{-1}$ is positive real. Then, the proof of theorem is completed ∎.